CONCOMITANT GRADIENTS IN LOW-FIELD NMR STUDIES OF RESTRICTED DIFFUSION

by

Jason Louis Hobson

Bachelor of Science (Honours), University of Victoria

THESIS SUBMITTED IN PARTIAL FULFILLMENT

OF THE REQUIREMENTS FOR THE DEGREE OF

MASTER OF SCIENCE

IN THE DEPARTMENT

OF

PHYSICS

APPROVAL

Name: Jason Louis Hobson

Degree: Master of Science

Title of Thesis: Concomitant Gradients in Low-Field NMR Studies of Restricted Diffusion

Examining Committee: Dr. E. Emberly, Assistant Professor (Chair)

Dr. M.E. Hayden, Associate Professor
Senior Supervisor

Dr. B.J. Frisken, Professor
Supervisor

Dr. H.D. Trottier, Professor
Supervisor

Dr. J.M. McGuirk, Assistant Professor
Internal Examiner

Date Approved: July 7, 2006

ii

Abstract

Linear magnetic field gradients are used in conventional magnetic resonance (MR) imaging in order to spatially encode and/or resolve nuclear spin distributions. These gradients are normally thought of as being unidirectional, but are always accompanied by orthogonal field components and gradients. These concomitant gradients can largely be ignored as long as the curvature they induce in magnetic field lines is small compared to inverse dimensions of the field of view. Recent attempts to acquire MR images in milliTesla magnetic fields have sparked interest in trying to understand the potential influence of concomitant field gradients. In this thesis a series of NMR experiments intended to probe diffusion of 3He gas within a restricted geometry and in very-low magnetic fields are described. Data from these experiments show clear evidence for the perturbing influence of concomitant gradients, and can be qualitatively understood in terms of a simple model that ignores diffusion.

Keywords: low-field nuclear magnetic resonance (NMR); concomitant gradients; restricted diffusion; polarized noble gas.

To my family and friends.
For even though I may crumble,
I know my foundation never will.

Acknowledgments

Completing this thesis was truly my most challenging project. I can say, with no sense of being overdramatic, that I would not have finished this project without the help of a network of very important people.

I have been blessed with a large family that has provided encouragement, support, and love in many forms throughout my graduate studies.

I was fortunate to work in a lab filled with intelligent and charismatic individuals who managed to fill each day with laughter and learning. Chris, with his quick mind and bottomless well of knowledge, proved to be the best companion an experimentalist could hope for. Josie, with her contagious laugh and undying motivation, was a brilliant example of the type of scientist I strive to be. Erin, with her sharp wit and useful advice, was my sounding board who kept me sane during insane times. And Geoff, with his amazing ability to master anything he bends his will towards, listened and answered every one of my questions no matter how basic or unintelligible.

Without my supervisor, Dr. Mike Hayden, this document would not be as polished as it is. His guidance and patience have been invaluable and his boundless enthusiasm for science has been a source of motivation. I hope that, thanks to him, I have now learned not to pepper my written word with "Jason" sentences.

Finally, I find it difficult to express in words what the commitment, dedication, and love of my wife, Kamini, have meant to me during this time. I have been constantly reminded that marrying her was the best decision I have ever made.

Contents

List of Tables

List of Figures

Chapter 1

Introduction

Magnetic field gradients are normally used in Magnetic Resonance Imaging (MRI) for phase encoding and/or spatial resolution of nuclei [1, 2]. An ideal encoding gradient should generate a linear relationship between position and magnetic field strength. This in turn would produce planes of constant Larmor precession frequency. Unfortunately, Maxwell's equations impose constraints that render this idealization impossible: a gradient applied in any one direction must be accompanied by orthogonal field components and gradients. These concomitant gradients reflect the curvature that is introduced when the field map is distorted. Yablonskiy et al. [3] recently predicted that concomitant gradients can cause idealized planes of constant precession frequency to warp into cylindrical surfaces with radius of curvature $R_c = B_0/G$, where B_0 is the magnitude of the static magnetic field and G is the strength of the applied gradient. In conventional high field MRI, where $B_0 \sim 1$ T and $G \sim 0.01$ T/m, the value of R_c that one obtains is of order 100 m. This is large compared to the imager itself (or, more importantly, the field of view) and so it is not surprising that concomitant gradients can be safely neglected for many applications. In this thesis, a different regime is explored. Several experiments are performed in which $B_0 \sim 600$ μT and G ranges from 0 to 0.005 T/m. This results in values of R_c as small as 10 cm, which is not much larger than the dimensions of the sample. With even lower values of B_0, the value of R_c has the potential to be even more extreme.

Ultimately, this work is motivated by the fact that in recent years there have been several attempts to perform MRI using very low ($B_0 \sim 1$ mT - 100 mT) [4–8] and ultra low ($B_0 \sim 1$ μT - 1 mT) [9, 10] static magnetic fields. More generally, there are scientific

and technological demands for being able to perform Nuclear Magnetic Resonance (NMR) experiments in the Earth's magnetic field [11–13]. Various advantages and disadvantages to working in these regimes have been discussed in the literature. Some of the advantages include the facts that low field magnets are not nearly as bulky as high field magnets and the amount of radio frequency power absorbed by the subject is significantly decreased [14]. Two disadvantages of working in low fields are that the Signal-to-Noise Ratio (SNR) from thermally polarized samples decreases and the potential introduction of image artifacts (like distortion or blurring) by concomitant gradients [3, 15–18]. The experiments reported in this thesis are specifically designed to probe the influence of concomitant gradients on the response of a nuclear spin system to a pulse sequence that is an important component of many conventional MRI sequences.

One method of counteracting the inherent decrease in SNR that occurs in low magnetic fields is to use hyperpolarized noble gases as contrast agents. The nuclei of ^{3}He and ^{129}Xe atoms can be polarized using a laser [19, 20] such that the magnetization density of the gas at pressures of order 40 Torr is similar to that of thermally polarized ^{1}H atoms in water at 1 T. The SNR one obtains using these hyperpolarized noble gases is thus only weakly dependent on magnetic field strength [21]. Over the last decade, hyperpolarized ^{3}He gas has become a useful tool for the study of lung structure and function in both high [22, 23] and low [4, 6, 7, 24] static magnetic fields. More generally, using the technique of spin echoes [25], hyperpolarized noble gases can be used to probe diffusion within restricted geometries. This method has been applied to the study of diffusion in porous media including the lungs [26–29], hydro-carbon bearing rocks [30] and other related porous systems [31], and have been used to acquire Apparent Diffusion Coefficient (ADC) images of the lungs [32, 33].

In general, the extraction of quantitative information from NMR experiments involving diffusion in restricted geometries is a complex problem [34–37]. Over time, invaluable experimental data have been obtained from studies performed on microscopic model pores including closely spaced parallel plates [38–41], small rectangular channels [42], long narrow cylindrical tubes [43] and bead-pack arrays. It was recently demonstrated that a much higher degree of control over geometry was possible in these experiments using macroscopic model pores filled with hyperpolarized gases. The work described in this thesis builds on that of Hayden et al. with gas diffusion in macroscopic cylindrical model

pores [5]. In particular, the conditions under which the attenuation of Free Induction Decays (FIDs) are influenced by concomitant gradients are studied.

Three different experimental parameters are varied: the magnetic field gradient strength, the position of the model pore with respect to the pivot point of the gradient field, and the ^{3}He gas density. The first two parameters directly influence the strength of the concomitant gradients to which the sample is exposed. The last parameter determines the distance that atoms can move during the period of time that the gradient is applied.

These experiments require an accurate measurement of the attenuation of a FID that is induced by the application of a field gradient. That is, an accurate measurement of the amplitude of the FID immediately before and after the gradient pulse must be made. As the gradient strength increases, the amplitude of the FID after the gradient pulse decreases and eventually becomes comparable to (or smaller than) the baseline noise level. In an effort to extend the dynamic range of the experiment as well as to evaluate possible systematic effects in the low SNR regime, an additional study was performed. Five different analytic models for FIDs were fit to simulated noisy data using a least squares minimization routine, and the accuracy and precision of the extracted fit parameters were compared.

The structure of the remainder of this thesis is as follows. The basic physics that is needed to understand the work presented in later chapters is outlined in Chapter 2. The experimental apparatus is described in Chapter 3. The various procedures that were used to probe the influence of concomitant gradients are summarized in Chapter 4. The study of the influence of noise on the extraction of the amplitude and decay time of a FID is presented in Chapter 5. The experimental results and the interpretation of these results are contained in Chapter 6. Finally, concluding remarks and suggestions for possible future work are given in Chapter 7.

Chapter 2

Theory

This chapter summarizes the theoretical basis for the experiments described in this thesis. The first section reviews the atomic energy level structure of the ^{3}He atom. The next section describes how nuclear polarization of ^{3}He is achieved by Metastability-Exchange Optical Pumping (MEOP). This is followed by a discussion of the physics of Nuclear Magnetic Resonance (NMR) and, more specifically, issues that arise when very low magnetic fields are employed. In addition, a description of the role of diffusion and the influence of geometry on the outcome of a few basic NMR experiments is included. The final section of this chapter discusses the influence of noise on the extraction of parameters, such as the transverse nuclear magnetization and apparent relaxation time, from low-field NMR Free Induction Decay (FID) data.

2.1 Energy Levels of the ^{3}He Atom

The following four subsections summarize the atomic energy level structure of the ^{3}He atom, with an emphasis on the states employed for optical pumping experiments. Three phenomena play role in defining this structure: spin-orbit coupling, the hyperfine interaction, and the Zeeman effect. Each of these contributes to the overall Hamiltonian for the ^{3}He atom; these contributions are discussed separately. Note that the discussion given below has been adapted from the treatments given by S. Gasiorowicz [44] and E. Courtade et al. [45].

2.1.1 The Basic Hamiltonian

To understand the basic form of the Hamiltonian for the ^{3}He atom, it is easiest to first consider the Hamiltonian for the Hydrogen atom and then introduce additional terms that account for the extra electron. Hydrogen consists of one proton and one electron. If we consider the nucleus (i.e. the proton) to be at rest, the Hamiltonian for hydrogen contains two terms: the kinetic energy of the electron and the Coulombic potential energy the electron experiences due to its interaction with the proton. In spherical coordinates, the Hydrogen Hamiltonian has the form

$$\mathcal{H} = -\frac{\hbar^2}{2m_e r^2}\nabla^2 - \frac{e^2}{4\pi\varepsilon_0}\frac{1}{r} \, , \tag{2.1}$$

where $\hbar$ is the reduced Planck constant, m_e is the mass of the electron, r is the distance between the nucleus and the electron, ∇^2 is the Laplacian in spherical coordinates, e is the charge of the electron, and ε_0 is the permittivity of free space.

The ^{3}He atom consists of two protons, one neutron and two electrons. The Hamiltonian for ^{3}He includes kinetic energy and Coulombic potential energy terms for both electrons analagous to those for the hydrogen atom as well as an additional potential energy term that describes the Coulombic repulsion between the two electrons. The ^{3}He Hamiltonian thus has the form

$$\mathcal{H} = \sum_{j=1}^{2}\left\{ -\frac{\hbar^2}{2m_e r_j^2}\nabla_j^2 - \frac{e^2}{4\pi\varepsilon_0}\frac{2}{r_j} + \frac{1}{2}\sum_{k\neq j}^{2}\frac{e^2}{4\pi\varepsilon_0}\frac{1}{|r_j - r_k|} \right\} . \tag{2.2}$$

The following three subsections describe modifications to this Hamiltonian that characterize additional interactions between the electrons and the nucleus as well as interactions between the atom and an external magnetic field.

2.1.2 Spin-Orbit Coupling

Coupling of electron spin angular momentum S and orbital angular momentum L results in the splitting of many of the electronic energy levels of ^{3}He. Spin-orbit coupling creates the fine structure of the ^{3}He atom and is caused by electron movement. In the rest frame of the electron, the electron experiences a magnetic field that is created by the relative motion of

the nucleus. To better understand the origin of the splitting we examine the correction that must be added to the basic Hamiltonian described above. The additional term has the form

$$\mathscr{H}_{so} = -\boldsymbol{\mu}_s \cdot \boldsymbol{B}_L \, , \tag{2.3}$$

where $\boldsymbol{\mu}_s$ is the magnetic moment of the electron and $\boldsymbol{B}_L$ is the magnetic field it experiences due to the "motion" of the nucleus. The magnetic moment is given by

$$\boldsymbol{\mu}_s = -\gamma_e \frac{e\hbar}{2m_e} \boldsymbol{S} \, . \tag{2.4}$$

where γ_e is the gyromagnetic ratio of the electron. The effective field is

$$\boldsymbol{B}_L = -\frac{1}{c^2} \boldsymbol{v} \times \boldsymbol{E} \, , \tag{2.5}$$

where c is the speed of light, $\boldsymbol{v}$ is the velocity of the electron and $\boldsymbol{E}$ is the electric field produced by the nucleus. A direct relationship between $\boldsymbol{B}_L$ and $\boldsymbol{L}$ is revealed through a series of substitutions. These include expressions for the momentum of the electron, $\boldsymbol{p} = m_e \boldsymbol{v}$ and the electric field

$$\boldsymbol{E} = \frac{E}{r} \boldsymbol{r} \, , \tag{2.6}$$

where E is the magnitude of the electric field, $\boldsymbol{r}$ is a vector that describes the position of the electron with respect to the nucleus and r is the magnitude of $\boldsymbol{r}$. Substituting these two expressions into Eq. 2.5 and rearranging the cross product yields

$$\boldsymbol{B}_L = \frac{\boldsymbol{r} \times \boldsymbol{p}}{m_e c^2} \frac{E}{r} \, . \tag{2.7}$$

Since $\boldsymbol{L} = \boldsymbol{r} \times \boldsymbol{p}$, Eq. 2.7 can be rewritten as

$$\boldsymbol{B}_L = \frac{\boldsymbol{L}}{m_e c^2} \frac{E}{r} \, . \tag{2.8}$$

The additional term to the Hamiltonian now has the form

$$\mathscr{H}_{so} = -\boldsymbol{\mu}_s \cdot \boldsymbol{B}_L = -\gamma_e \frac{e\hbar}{2m_e^2 c^2} \frac{E}{r} \boldsymbol{S} \cdot \boldsymbol{L} \tag{2.9}$$

or

$$\mathcal{H}_{so} \propto \boldsymbol{S} \cdot \boldsymbol{L} \, . \tag{2.10}$$

The magnitude of the spin angular momentum $\boldsymbol{S}$ can have $2S+1$ possible values. The ^{3}He atom has two electrons, each with spin $s = 1/2$. Therefore, because of the Pauli exclusion principle, the total S of these electrons must be 0 in the ground state but can be 0 or 1 for excited states. The magnitude of the orbital angular momentum $\boldsymbol{L}$ can have $2\ell+1$ different values but ℓ is limited to the range

$$\ell = 0, 1, \ldots n - 1 \, , \tag{2.11}$$

where n is the principal quantum number. At this point it is useful to introduce the total angular momentum

$$\boldsymbol{J} = \boldsymbol{S} + \boldsymbol{L} \, . \tag{2.12}$$

The eigenvalues of $\boldsymbol{J}$ are

$$J = S + \ell, S + \ell - 1, \ldots, |S - \ell| \, . \tag{2.13}$$

This presents an easy method for determining which orbitals are split by the spin-orbit coupling.

As an aside, in the following examples, and throughout this thesis, individual orbitals will be referred to using the following notation

$$n^{2S+1}\ell_J \, . \tag{2.14}$$

However, ℓ will be denoted with the conventional method of replacing its numerical value with letters (S for $\ell=0$ and P for $\ell=1$).

Consider the ^{3}He ground state, denoted 1^1S_0. In this state, S and ℓ are both equal to 0 and, therefore, there is no orbital splitting due to spin-orbit coupling. The same is true of the first excited state where $S = 1$ and $\ell = 0$, denoted 2^3S_1. The first case of orbital splitting from spin-orbit coupling occurs in the 2^3P states in which $S = 1$ and $\ell = 1$. Since J can equal 0, 1, or 2 the excited state is split into three separate sublevels, denoted 2^3P_0, 2^3P_1, and 2^3P_2.

2.1.3 Hyperfine Structure

Hyperfine structure of atomic energy levels is a result of the interaction between the nuclear magnetic moment and the magnetic field generated by orbiting electrons. This phenomenon can be understood using an approach similar to that used in the previous subsection. The additional term that needs to be added to the Hamiltonian to account for the hyperfine interaction has the form

$$\mathcal{H}_{hf} = -\boldsymbol{\mu}_N \cdot \boldsymbol{B}_J \, , \tag{2.15}$$

where $\boldsymbol{\mu}_N$ is the magnetic moment of the nucleus and $\boldsymbol{B}_J$ is the magnetic field the nucleus experiences due to the presence of the electrons. The magnetic moment of the nucleus is given by

$$\boldsymbol{\mu}_N = -\gamma_N \frac{e\hbar}{2m_N} \boldsymbol{I} \, , \tag{2.16}$$

where γ_N is the gyromagnetic ratio of the nucleus, m_N is the mass of the nucleus and $\boldsymbol{I}$ is the nuclear angular momentum which takes on $2I+1$ different values. In the case of ^{3}He, I is equal to $1/2$. Using methods of substitution similar to those outlined in Subsection 2.1.2, a relationship can be found between $\boldsymbol{B}_J$ and $\boldsymbol{J}$, the total electronic angular momentum. The ensuing Hamiltonian is

$$\mathcal{H}_{hf} \propto \boldsymbol{I} \cdot \boldsymbol{J} \, . \tag{2.17}$$

We can introduce the vector

$$\boldsymbol{F} = \boldsymbol{J} + \boldsymbol{I} \, , \tag{2.18}$$

which represents the sum of the electronic and nuclear angular momenta. The eigenvalues of $\boldsymbol{F}$ are given by

$$F = J+I \, , J+I-1 , \ldots , |J-I| \, . \tag{2.19}$$

Again, we can see that the ^{3}He $1\,^1S_0$ ground state, which has $J=0$ and $I=1/2$, has no hyperfine structure. The $2\,^3S_1$ excited state, which has $J=1$ and $I=1/2$, is split into two sublevels defined by $F=1/2$ and $F=3/2$. Also, the $2\,^3P$ states, which were split into three sublevels by

spin-orbit coupling, are further split into five separate sublevels by the hyperfine interaction. Figure 2.1 summarizes the spin-orbit and hyperfine contributions to the first two excited states of the ^{3}He atom.

2.1.4 The Zeeman Effect

When an atom is placed in a magnetic field, the electronic states split into even more sublevels. There are two effects which split the ground state and the excited states. If we consider the ground state of ^{3}He, we have to examine the interaction between the external magnetic field and the nuclear magnetic moment. The correction to the Hamiltonian has the form

$$\mathcal{H}_z = -\boldsymbol{\mu}_N \cdot \boldsymbol{B}_0 \ , \tag{2.20}$$

where $\boldsymbol{B}_0$ is the external magnetic field. If $\boldsymbol{B}_0$ defines the z-direction, then only the z-component of $\boldsymbol{I}$

$$I_z = m_I \hbar \tag{2.21}$$

interacts with $\boldsymbol{B}_0$. Here m_I is the nuclear magnetic quantum number which takes on values

$$m_I = I, I-1, \ldots -I \ . \tag{2.22}$$

Since I is 1/2 for ^{3}He, the 1^1S_0 ground state will split into two sublevels corresponding to m_I equal to +1/2 and -1/2.

The magnetic field also has an effect on the excited states, but instead of $\boldsymbol{\mu}_N$, the total magnetic moment $\boldsymbol{\mu}_F$ must be considered. The correction to the Hamiltonian has the form

$$\mathcal{H}_z = -\boldsymbol{\mu}_F \cdot \boldsymbol{B}_0 \ , \tag{2.23}$$

where

$$\boldsymbol{\mu}_F \propto \boldsymbol{F} \ . \tag{2.24}$$

Again, if $\boldsymbol{B}_0$ defines the z-direction, then only the z-component of $\boldsymbol{F}$
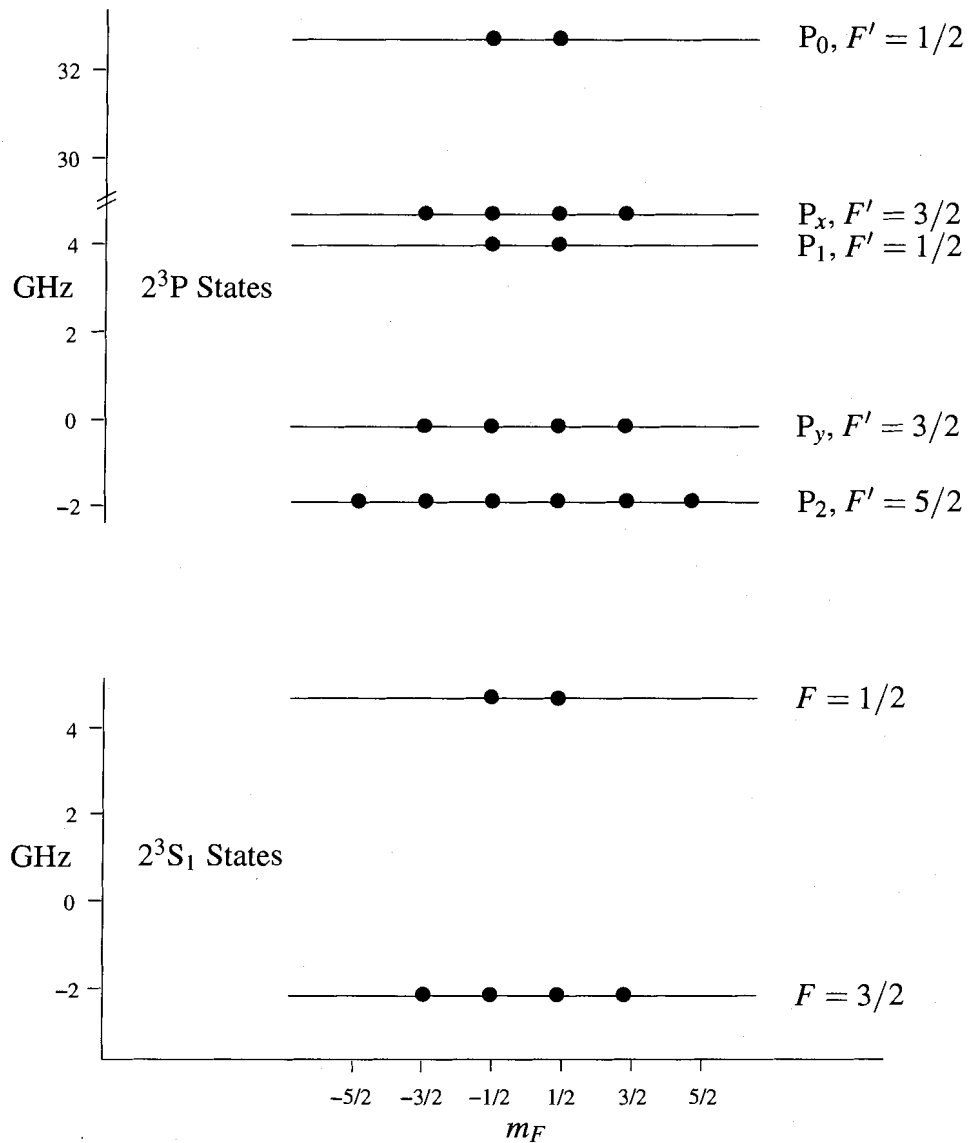
Figure 2.1: The various energy levels arising from spin-orbit coupling, the hyperfine interaction, and the hyperfine Zeeman effect on the 2^3S_1 and 2^3P excited states. Altogether the 2^3S_1 and 2^3P excited states are split into a total of 7 sublevels by spin-orbit coupling and the hyperfine interaction and a total of 24 sublevels when the Zeeman effect is included. The sublevels of the 2^3P excited state that correspond to $F' = 3/2$ are denoted by P_x and P_y for clarity. This figure has been adapted from the work of E. Courtade et al. [45].

$$F_z = m_F \hbar \qquad (2.25)$$

interacts with the field. As usual, m_F takes on the values

$$m_F = F, F - 1, \ldots, -F . \qquad (2.26)$$

The 2^3S_1 excited state is split into six Zeeman sublevels by this effect. There are four Zeeman sublevels for the state corresponding to the $F=3/2$ hyperfine state and two Zeeman sublevels for the $F=1/2$ hyperfine state. The 2^3P excited state is split into 18 Zeeman sublevels. These levels are summarized in Fig. 2.1.

2.2   Metastability-Exchange Optical Pumping

In thermal equilibrium, and in the presence of a static magnetic field, a gas of ^{3}He atoms will consist of two populations: those with nuclei that are parallel to and those with nuclei that are antiparallel to the magnetic field. The ratio of the difference between these populations to the total number of atoms is referred to as the polarization of the sample (see subsection 2.3.1). The term "hyperpolarized" will be used here in reference to a situation where the gas has been driven to a state of nuclear polarization that is larger - often by many orders of magnitude - than that achieved in thermal equilibrium. Hyperpolarized ^{3}He can be produced in several different ways, including two optical techniques: Metastability-Exchange Optical Pumping (MEOP) [19] and Spin Exchange Optical Pumping (SEOP) [20]. MEOP has been used to produce nuclear polarization as high as 90% at ^{3}He pressures of 0.7 mbar [46]. All of the experiments discussed in this thesis were performed using MEOP.

In MEOP, polarized light at 1083 nm is used to induce transitions from the 2^3S_1 metastable state to the 2^3P excited state. In the experiments presented in this thesis, circularly polarized light was used to induce the transition ultimately resulting in a large electronic polarization of 2^3S_1 atoms. Electronic spin polarization is then transferred to the nucleus by the hyperfine interaction. Finally, nuclear polarization is transferred to ground-state atoms through metastability-exchange collisions. The following subsections describe this sequence of events in further detail.

2.2.1 Optical Pumping of ^{3}He

Optical pumping is a technique for manipulating electron state populations. It often requires ensuring that appropriate excited electronic states of the atom are populated. For ^{3}He, which is a gas, a radio-frequency discharge is typically used to excite the atoms. The atoms of interest are those that are trapped in the long-lived 2^3S_1 metastable state. The term metastable here refers to an excited state that has a longer lifetime than ordinary excited states. The longer lifetime comes about because transitions from metastable states are "forbidden" by selection rules and are much less probable than "allowed" transitions from excited states. The natural lifetime of the 2^3S_1 excited state is 8×10^3 s, but in practice atoms in this state relax during wall collisions. For example, in a 5 cm diameter by 5 cm long cylindrical cell filled with 1 Torr of ^{3}He the diffusion time to the walls and hence the metastable lifetime is of order 1.5 ms [47].

It is possible to optically pump electrons from the 2^3S_1 states to the 2^3P states. The different transitions that are allowed between the 2^3S_1 and 2^3P sublevels are displayed in Fig. 2.2. If circularly polarised light is used to selectively pump the electrons into the 2^3P sublevels the selection rule $\Delta m_f = \pm 1$ for total angular momentum must be taken into account. That is, incident light with right- or left-handed polarization will excite transitions between the 2^3S_1 and 2^3P sublevels such that $\Delta m_F = +1$ or $\Delta m_F = -1$, respectively. Once excited, the electrons have an equal probability of radiative decay to either of the 2^3S_1 sublevels. The result of constant pumping will be an accumulation of electrons in the 2^3S_1 sublevels either with high m_F values, if right-handed polarized light is used, or low m_F values, if left-handed polarized light is used.

Consider the C_8 transition between the 2^3S_1, $F=1/2$ and the 2^3P_0, $F'=1/2$ sublevels (see Fig. 2.2). Incident light with right-handed polarization will only excite electrons from the 2^3S_1, $m_F=-1/2$ sublevel to the 2^3P_0, $m_F=1/2$ sublevel (see Fig. 2.1). The atom then has an equal probability of decaying into the 2^3S_1, $m_F=-1/2$ or 2^3S_1, $m_F=+1/2$ sublevels. The net result will be an accumulation of electrons in the 2^3S_1, $m_F=+1/2$ sublevel. For the experimental work presented in this thesis, the C_9 transition was used.
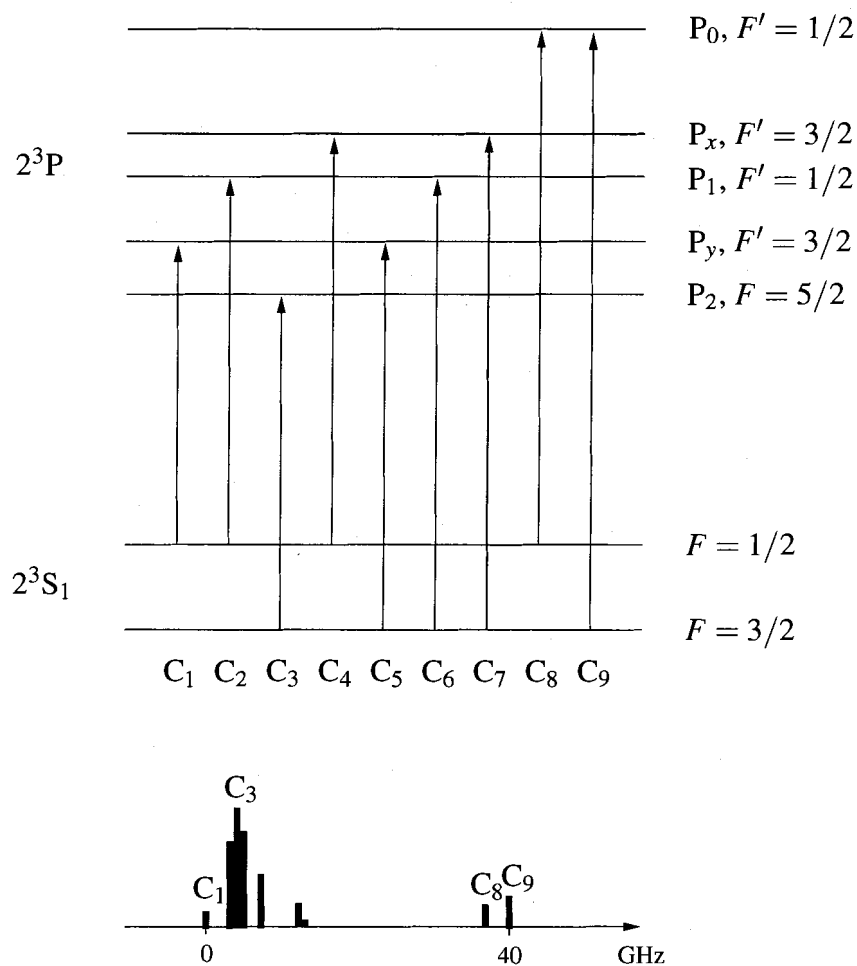
Figure 2.2: The nine possible transitions (labeled C_1-C_9) between the 2^3S_1 and 2^3P states of the ^{3}He atom. The C_9 transition was used for all MEOP experiments described in this thesis. The C_9 transition corresponds to a zero-field wavelength of 1083.031 nm [45]. The sublevels of the 2^3P excited state that correspond to $F' = 3/2$ are denoted by P_x and P_y for clarity.

2.2.2 Metastability-Exchange Collisions

Once metastable ^{3}He atoms are polarized, the resultant electronic polarization is transferred to the nucleus by the hyperfine interaction. Metastable atoms undergo two types of collisions: direct collisions with no metastability-exchange and metastability-exchange collisions. Direct collisions have little effect on the values of I and S of atoms. In metastability-exchange collisions, nuclear polarization is transferred to ground state atoms [48]. A metastability-exchange collision involves the transfer of electrons between excited and ground state atoms. In effect, this results in nuclear polarization of the ground state atom but leaves the electronic orientation S of the metastable atom unchanged. This reaction can be described by

$$^3\text{He}\left(\downarrow\right) + {}^3\text{He}^*\left(\uparrow\right) \rightarrow {}^3\text{He}^*\left(\downarrow\right) + {}^3\text{He}\left(\uparrow\right) ,$$
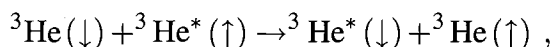
where ^{3}He represents an atom in the ground state, ^{3}He* represents an atom in the 2^3S$_1$ metastable state and the arrow next to each term represents nuclear spin.

2.3 Nuclear Magnetic Resonance

Nuclear Magnetic Resonance (NMR) refers to a broad class of phenomena that involve manipulating nuclear spin state populations of spin-bearing atoms or molecules immersed in a static magnetic field. The manipulation is accomplished by applying an additional, oscillating magnetic field that induces transitions between nuclear spin states. In a classical sense, the oscillating magnetic field drives the nuclear magnetic moment away from thermal equilibrium and causes it to precess about the static magnetic field. This precession can be detected by various means and recorded as an electronic signal. NMR is used in Magnetic Resonance Imaging (MRI) and to perform NMR spectroscopy. In this thesis, NMR is used to probe the influence of concomitant gradients on the coherent rephasing of nuclear precession signals during a bipolar gradient pulse.

The first subsection below introduces the notion of thermal equilibrium and nuclear polarization. The following two subsections summarize a few aspects of the classical model for pulsed NMR. Following that a description of two pulse sequences used to manipulate nuclei is presented. Finally, in the last two subsections, there is a discussion of the manner

in which NMR is used to probe diffusion. This discussion follows the treatment outlined by Abragam [49].

2.3.1 Population Distributions

NMR experiments probe the net magnetic moment of a collection of nuclei. To determine the net magnetic moment, it is necessary to consider the influence of a static magnetic field on individual nuclei. As mentioned in subsection 2.1.4, there are two ways for the magnetic moment of a ^{3}He nucleus to align with an external magnetic field B_0, depending on the value of m_I. When m_I is +1/2, the nucleus is considered to be aligned parallel with B_0 and when m_I is -1/2, the nucleus is considered to be aligned anitparallel with B_0. The energy of these states is given by

$$E = -\gamma \hbar B_0 m_I \ , \tag{2.27}$$

where γ is the gyromagnetic ratio of the ^{3}He nucleus and B_0 is the magnitude of the external magnetic field. For ^{3}He gas in thermal equilibrium, there will be two populations denoted, N_+ and N_-, that represent the total number of nuclei that have aligned parallel and antiparallel to B_0, respectively. The relative thermal equilibrium population of an ensemble of spins is given by

$$\frac{N_+}{N_-} = e^{-\Delta E / k_B T} \ , \tag{2.28}$$

where ΔE is the difference in energy between the two populations

$$\Delta E = E_+ - E_- = -\frac{1}{2}\gamma \hbar B_0 - \left(+\frac{1}{2}\gamma \hbar B_0 \right) = -\gamma \hbar B_0 \ . \tag{2.29}$$

The polarization of an ensemble of spins is defined as

$$P = \frac{N_+ - N_-}{N_+ + N_-} = \tanh\left(\frac{\gamma \hbar B_0}{2 k_B T} \right) \ . \tag{2.30}$$

The value of γ for a ^{3}He atom is $2\pi \times 3.243 \times 10^7$ rad/sT [50]. For a magnetic field strength of 6 Gauss (the approximate field used for the experiments presented in this thesis) and 293 K the thermal equilibrium polarization of ^{3}He gas is 1.6 parts per billion. The magnetization, or the net magnetic moment per unit volume, is
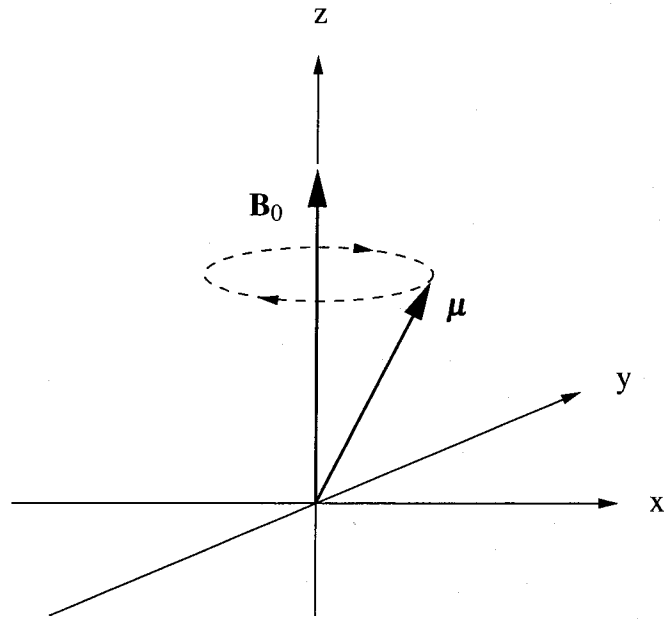
Figure 2.3: The motion of a magnetic moment $\boldsymbol{\mu}$ about a magnetic field $\boldsymbol{B_0}$.

$$M_0 = N_V \mu \tanh\left(\frac{\gamma \hbar B_0}{2k_B T}\right) ,\tag{2.31}$$

where N_V is the total number of particles per unit volume and μ is the magnetic moment of a single atom. The magnetization density of ^{3}He gas at room temperature and a pressure of 1 Torr is $M_0 \approx 5.5 \times 10^{-13}$ A/m in a 6 Gauss field. This can be raised to $M_0 \approx 9.0 \times 10^{-7}$ A/m using MEOP. For the sake of comparison, $M_0 \approx 3.5 \times 10^{-5}$ A/m for protons in room temperature water at 1 T.

2.3.2 Free Precession

A magnetic moment $\boldsymbol{\mu}$ in a magnetic field $\boldsymbol{B_0}$ experiences a torque (see Fig. 2.3). The equation of motion for $\boldsymbol{\mu}$ is

$$\frac{d\boldsymbol{\mu}}{dt} = \gamma\boldsymbol{\mu} \times \boldsymbol{B_0} .\tag{2.32}$$

In a classical context this leads to free precession of $\boldsymbol{\mu}$ around $\boldsymbol{B_0}$ at a frequency

$$\omega_0 = \gamma B_0 \, , \tag{2.33}$$

known as the Larmor frequency.

In practice, NMR usually involves the manipulation of a very large number of nuclear spins, and so a classical treatment of nuclear spin precession is often adequate. Instead of considering individual magnetic moments, one introduces the net nuclear magnetization

$$M = \frac{1}{V} \sum_{j=1}^{N} \mu_j, \tag{2.34}$$

where the sum is over the N particles in the system. The equation of motion for M is thus

$$\frac{dM}{dt} = \gamma M \times B_0 \, . \tag{2.35}$$

The motion of M can be modified by changing the magnetic field. Consider the effect of applying a magnetic field $2B_1$ that is orthogonal to B_0 and oscillating at a frequency ω that is approximately equal to ω_0. This linearly polarized field can be decomposed into two counter rotating components, each with magnitude B_1. In the reference frame rotating at frequency ω (in the same sense as the nuclear spin precession) the equation of motion for M is

$$\frac{dM}{dt} = \gamma M \times B_{eff} \, , \tag{2.36}$$

where

$$B_{eff} = \left(B_0 - \frac{\omega}{\gamma} \right) k + B_1 i \, , \tag{2.37}$$

where i and k are unit vectors in the rotating reference frame. The influence of the counter-rotating component of B_1 can be neglected for many situations and does not play a role in the work described in this thesis. In the rotating reference frame, M precesses about B_{eff}. In the laboratory reference frame this corresponds to a spiral motion about B_0. If B_1 is applied at ω_0 (i.e. at resonance) then B_{eff} is simply

$$B_{eff} = B_1 i \tag{2.38}$$

and thus M precesses about i at frequency γB_1. The angle through which M rotates is given by

$$\theta = \gamma B_1 t , \tag{2.39}$$

where t is the length of time for which B_1 is applied. Two common angles that are used in NMR are 90 and 180 degrees. The application of B_1 "tipping pulses" that give rise to these rotations are known as $\pi/2$-pulses and π-pulses, respectively. A $\pi/2$ pulse is commonly used to rotate M from its equilibrium orientation along k into the transverse plane.

2.3.3 Relaxation Processes

After the application of a tipping pulse, B_0 becomes the effective field again. The manner in which M returns to thermal equilibrium can often be described by the Bloch model [51]. The Bloch model contains two phenomenological parameters that characterize the rate at which M returns to equilibrium: the longitudinal relaxation time T_1 and the transverse relaxation time T_2. The evolution of M caused by relaxation processes can be superimposed on the free evolution of the spins to give

$$\frac{dM}{dt} = \gamma M \times B_0 - \frac{M_x i + M_y j}{T_2} - \frac{M_z - M_0}{T_1} k . \tag{2.40}$$

T_1 is a measure of the characteristic time it takes the longitudinal component of the magnetization M_z to align with B_0 following any perturbation from thermal equilibrium. This form of relaxation is typically induced by magnetic field fluctuations resulting from atomic or molecular motion. The Bloch equation that describes the relaxation of M_z is thus

$$\frac{dM_z}{dt} = \frac{M_0 - M_z}{T_1} , \tag{2.41}$$

where M_0 is the magnitude of M_z at equilibrium. This can be solved to find

$$M_z = M_0 + [M_z(0) - M_0] e^{-t/T_1} , \tag{2.42}$$

where $M_z(0)$ is the value of M_z at $t = 0$, or immediately after B_1 is turned off.

T_2 is a measure of the timescale for transverse magnetization to persist in a perfectly uniform external magnetic field. Interactions between nuclei eventually destroy any such

coherence in the transverse magnetization. In the rotating reference frame, the Bloch equations that describe the decay of transverse magnetization are

$$\frac{dM_x}{dt} = -\frac{M_x}{T_2} \tag{2.43}$$

$$\frac{dM_y}{dt} = -\frac{M_y}{T_2}, \tag{2.44}$$

where M_x and M_y are the components of the magnetization along the x and y axis in the rotating reference frame, respectively. These equations can also be solved to show

$$M_x(t) = M_x(0)e^{-t/T_2} \tag{2.45}$$

$$M_y(t) = M_y(0)e^{-t/T_2}, \tag{2.46}$$

where $M_x(0)$ and $M_y(0)$ are the values of M_x and M_y at $t = 0$, or immediately after B_1 is turned off. If there are inhomogeneities in the external magnetic field then the apparent decay rate for the transverse magnetization is faster. In this case the apparant decay time is denoted T_2^*.

2.3.4 NMR Detection

In a typical inductively-detected NMR experiment, receive coils are used to monitor the precession of the transverse magnetization. These coils are tuned with a capacitor such that the electronic (RLC) resonance matches the Larmor frequency. The coils used for the work described in this thesis are discussed in subsection 3.2.2. The precession of the transverse magnetization is detected as an induced EMF ε across the coils as described by Faraday's Law

$$\varepsilon = -N\frac{d\Phi}{dt}, \tag{2.47}$$

where N is the number of turns in the coil and Φ is the magnetic flux through the coil. The induced EMF following a tipping pulse is known as a free induction decay (FID) and is proportional to

$$M(t) = M_\perp e^{-t/T_2} e^{i(\omega_0 t + \phi)} \, ,   \tag{2.48}$$

where

$$M_\perp = \sqrt{(M_x(0))^2 + (M_y(0))^2} \, ,   \tag{2.49}$$

and

$$\phi = \tan^{-1}\left(\frac{M_y(0)}{M_x(0)}\right) \, .   \tag{2.50}$$

Equation 2.48 is the solution to the Bloch equations in the laboratory frame. Typically, the next stage in the detection process is to amplify the induced EMF. After amplification, the voltage signal is fed to two phase-sensitive detectors (PSD). These detectors separate the orthogonal M_x and M_y components of the induced EMF. One PSD multiplies the induced EMF by a reference voltage signal

$$\varepsilon_{ref} = \varepsilon_L \cos(\omega_L t) = \frac{1}{2}\varepsilon_L \left[e^{i\omega_L t} + e^{-i\omega_L t} \right] \, ,   \tag{2.51}$$

derived from the local oscillator used to generate tipping pulses, where ε_L is the amplitude and ω_L is the frequency of the reference voltage signal. The output of the PSD is

$$\begin{aligned}
\varepsilon_{psd} &= \frac{1}{2} M(t) \varepsilon_L \left[e^{i\omega_L t} + e^{-i\omega_L t} \right] \\
&= \frac{1}{2} M_\perp \varepsilon_L e^{-t/T_2} e^{i(\omega_0 t + \phi)} \left[e^{i\omega_L t} + e^{-i\omega_L t} \right] \\
&= \frac{1}{2} M_\perp \varepsilon_L e^{-t/T_2} \left[e^{i((\omega_0 + \omega_L)t + \phi)} + e^{i((\omega_0 - \omega_L)t + \phi)} \right] \, .
\end{aligned}$$

The PSD output is passed through a low pass filter. The resultant voltage signal from the filter if $\omega_0 \approx \omega_L$ is

$$\varepsilon_{psd} = \frac{1}{2} M_\perp \varepsilon_L e^{-t/T_2} e^{i((\omega_0 - \omega_L)t + \phi)} \, .   \tag{2.52}$$

If ϕ is chosen such that $\phi = 0$ then the resultant signal is a measure of M_x. The second PSD is 90° out of phase with the first PSD. Therefore, $\phi = \pi/2$ and the resultant signal is a measure of M_y. These voltage signals can then be recorded using an analog to digital converter and stored in a digital format for subsequent processing.
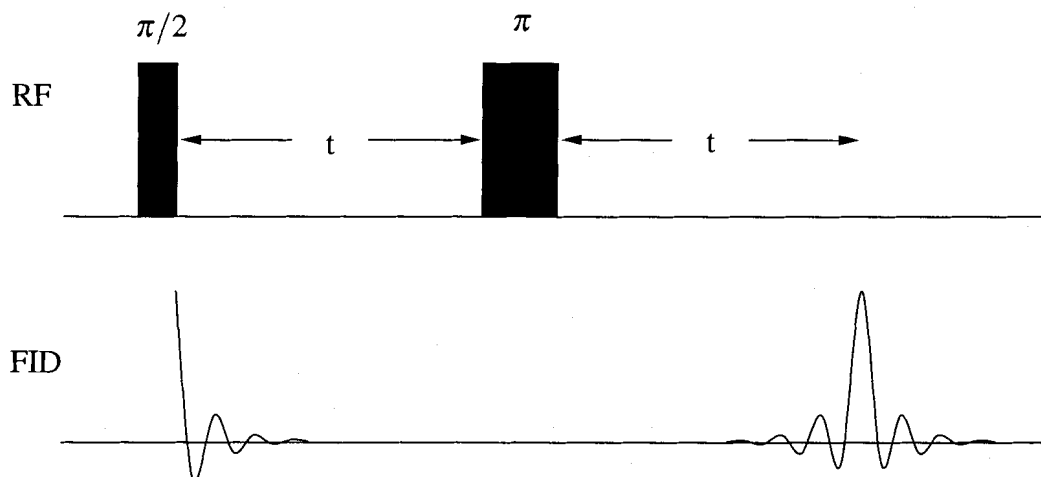
Figure 2.4: A Carr-Purcell spin echo experiment. The upper half of the figure shows the timing of the two tipping pulses. The lower half shows an example of the FID that might be recorded during the experiment. The duration of the tipping pulses is typically much shorter than t.

2.3.5 Spin Echoes

The phenomenon of spin echoes was first described in 1950 by E. L. Hahn [25]. Fig. 2.4 shows an elementary sequence of B_1 pulses that can be used to generate what is commonly referred to as a Hahn spin echo. This particular sequence is known as a Carr-Purcell sequence [52]. First, a $\pi/2$-pulse is applied, causing M to rotate from its equilibrium orientation along z into the transverse plane. Once the tipping pulse is turned off, M will begin to precess about the static magnetic field. Immediately, the transverse components of M begin to decay with the characteristic time T_2^* due to field inhomogeneities. These inhomogeneities cause individual nuclei to have slightly different Larmor frequencies. Therefore, the decay in M is caused by a "fanning out" of the individual magnetic moments (see Fig. 2.5) in the rotating reference frame as some nuclei get ahead of the average phase and others fall behind. To remove the effect of field inhomogeneities a π-pulse is applied at a time t after the initial pulse. The π-pulse rotates the magnetic moments by $180°$. After the π-pulse, the individual magnetic moments that were rotating slower than the average rate and had fallen behind now find themselves with more than the average acquired phase. Those moments that were precessing faster than the average rate are now behind the aver-
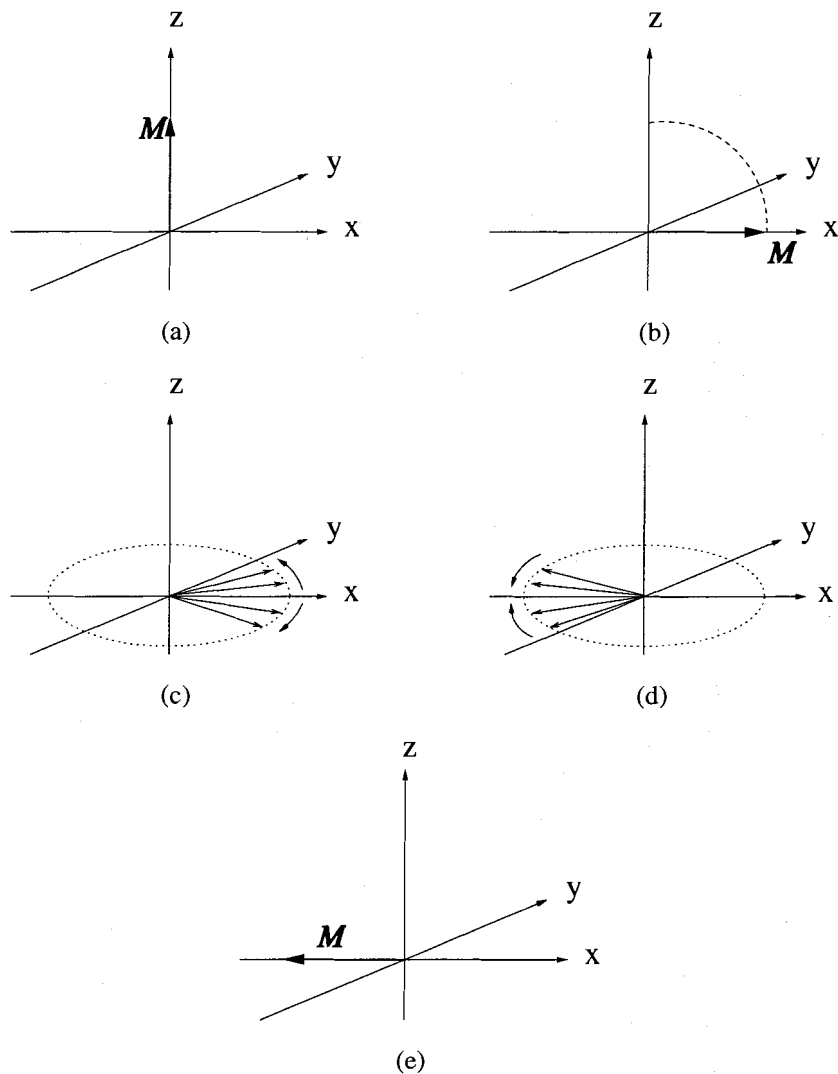
Figure 2.5: The evolution of the transverse magnetization M during a spin echo experiment. In this series of figures, the static magnetic field B_0 defines the z-axis. Figure 2.5(a) shows the magnetization vector in its initial state before the spin-echo experiment begins. The application of the $\pi/2$-pulse rotates M into the transverse plane (Fig. 2.5(b)). Immediately after the $\pi/2$-pulse, field inhomogeneities cause the individual magnetic moments to "fan out" or deviate in phase from nuclei precessing at the average Larmor frequency (Fig. 2.5(c)). The π-pulse rotates the magnetic moments by 180° so that they begin to rephase (Fig. 2.5(d)). Finally, a time $2t$ after the application of the $\pi/2$-pulse, the magnetic moments rephase to form a large transverse magnetization (Fig. 2.5(e)).

age. Therefore, after the π-pulse, the individual moments begin to rephase, increasing the coherence and the net transverse magnetization. This refocusing is known as a spin echo. The Hahn spin echo occurs at a time $2t$ after the $\pi/2$-pulse. The net magnetization will disappear again but can be refocused with further applications of properly timed π-pulses, in which case the sequence is known as a Carr-Purcell-Meiboom-Gill sequence [53]. The spin echo experiment removes the effect of field inhomogeneities and provides access to the intrinsic transverse relaxation time T_2.

2.3.6 Free Diffusion

Up to this point, it has been implicitly assumed that nuclei are static (i.e. they can precess but have no translational motion). In terms of the spin echo sequence described above, this assumption means that the Larmor frequency of each spin remains the same throughout the sequence. If B_0 is not homogeneous, random translational motion will cause the phase accumulated by each nucleus to be different. As a result, perfect refocusing of the transverse magnetization is not possible, and the amplitude of the spin echo will be attenuated. These effects can be evaluated by adding a diffusion term to the Bloch equation. The resulting equation was first written down by H. C. Torrey and is known as the Bloch-Torrey equation [54]

$$\frac{d\boldsymbol{M}}{dt} = \gamma \boldsymbol{M} \times \boldsymbol{B}_0 - \frac{M_x \boldsymbol{i} + M_y \boldsymbol{j}}{T_2} - \frac{M_z - M_0}{T_1}\boldsymbol{k} + D_0 \nabla^2 \boldsymbol{M} , \qquad (2.53)$$

where D_0 is the free diffusion coefficient for the spin-bearing atoms or molecules.

One method of measuring D_0 is to use the pulsed gradient spin echo sequence (PGSE) [38] shown in Fig. 2.6. A PGSE is similar to a Carr-Purcell spin echo pulse sequence except that a constant and uniform magnetic field gradient G is intentionally applied for a time τ before and after the π-pulse. During the application of this idealized gradient field, the effective magnetic field at a spatial location r is

$$\boldsymbol{B}_{eff} = B_0 \boldsymbol{k} + \boldsymbol{G} \cdot \boldsymbol{r} . \qquad (2.54)$$

Torrey's analysis of Eq. 2.53 showed that diffusion in the presence of this gradient leads to an attenuation of the transverse magnetization. This decay is described by
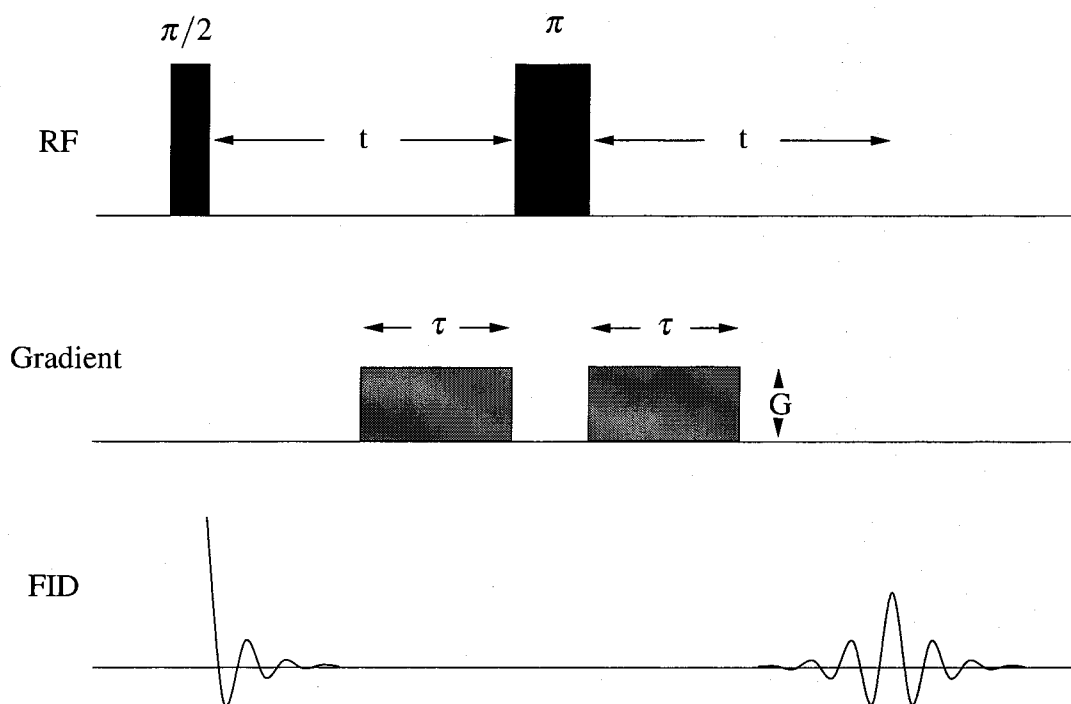
Figure 2.6: A pulsed-gradient spin echo sequence. The upper section of the figure shows the timing of the two tipping pulses. The middle section shows the timing of the pulsed gradient fields. The lower section shows an example of the FID that might be recorded during the experiment.
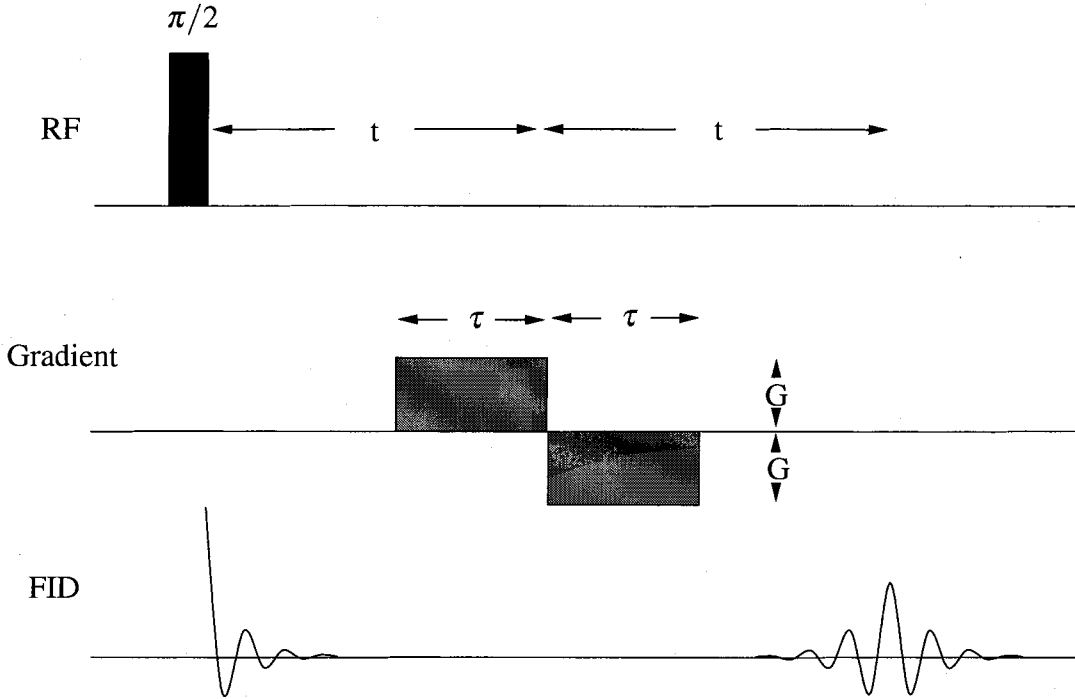
Figure 2.7: A gradient-recalled spin echo sequence. The upper section of the figure shows the timing of the tipping pulse. The middle section shows the timing of the gradient pulse field. The lower half shows an example of the FID that would be recorded during the experiment.

$$M = M_0 \exp\left[-\frac{2}{3} D_0 \gamma^2 G^2 \tau^3 \right] , \qquad (2.55)$$

where G is the amplitude of the gradient and τ is the length of time for which the gradient is applied. This experiment is only sensitive to random atomic displacements along the direction of the gradient G.

In this thesis, a gradient-recalled spin echo (GRSE) sequence is used to probe atomic diffusion (shown in Fig. 2.7). A GRSE is similar to the PGSE but employs a bipolar gradient pulse instead of the combination of two identical gradient pulses and a π-pulse. GRSE sequences are widely used in MRI [55]. A distinct advantage of GRSE sequences is that an image can be acquired with significantly fewer RF pulses, which decreases both the RF power delivered to the subject and the imaging time. The PGSE sequence changes

the phase of the precessing magnetization with the π-pulse. The GRSE sequence changes the direction of the gradient which changes the sign of the Hamiltonian. If the gradient is ideal (i.e. the gradient generates a linear relationship between position and magnetic field strength) these two operations are mathematically equivalent. However, if the full expression for a field gradient is considered (i.e. to take into account the existence of concomitant gradients) the mathematical equivalence of the two sequences no longer exists (see subsection 2.4.1). This difference is increasingly important as B_0 is lowered.

2.3.7 Restricted Diffusion

The discussion of the previous section assumes that the random motions of atoms are not impeded. That is, the sample is infinite in extent. However, in experiments where D_0 is large and/or the sample size is small this assumption breaks down. Under these conditions the translational motion of atoms is "restricted". Nevertheless, the attenuation of a FID or spin echo can be formally represented by

$$M = M_0 \exp\left[-\frac{2}{3} D_{eff} \gamma^2 G^2 \tau^3 \right] , \tag{2.56}$$

where D_{eff} is an effective diffusion coefficient that is both time- and geometry-dependent. This type of situation was first studied by Wayne and Cotts [39, 40]. One expects that $D_{eff} < D_0$ simply because motions are restricted. A full analysis of the restricted diffusion problem requires that three different length scales be considered: the characteristic length scale for diffusion ℓ_D, the structural length scale ℓ_s and the dephasing length ℓ_G. The diffusion length scale, ℓ_D, is a measure of the characteristic distance an atom will diffuse along the direction of the applied gradient during a time τ and is given by

$$\ell_D = \sqrt{D_0 \tau} . \tag{2.57}$$

The structural length scale ℓ_s is a measure of the characteristic distance an atom must travel before colliding with a physical barrier. The dephasing length scale is a measure of the characteristic distance that an atom must diffuse to accumulate a 2π phase shift with respect to its original position [56], and is given by

$$\ell_G = \left(\frac{D_0}{\gamma G}\right)^{\frac{1}{3}}.$$ (2.58)

One can identify three different regimes in which the attenuation of FID or spin-echo amplitudes differ: free diffusion, motional averaging, and localization. To determine the relevant regime, it is necessary to consider the relative size of the three length scales (see Fig. 2.8). The free diffusion regime occurs when $\ell_D \ll \ell_s$ and ℓ_G (i.e. the majority of atoms do not come into contact with physical boundaries during the experiment) and, therefore, Eq. 2.55 remains valid. The motionally averaged regime occurs when ℓ_s is the smallest length scale. In this regime, the time scale of the experiment is long enough that the distance atoms diffuse is large compared to ℓ_s. Finally, the localization regime occurs when ℓ_G is the shortest length scale. In this regime, atoms within the container a distance ℓ_G apart become indistinguishable. The form of FID and spin echo attenuation envelopes in this latter regime are modified significantly from the form given by Eqs. 2.55 and 2.56.

The relationship between D_{eff} and D_0 can be calculated analytically for three prototypical geometries: slab, cylindrical, and spherical [57]. The relationship for a cylindrical geometry is of particular interest as all experiments described in this thesis made use of ^{3}He gas confined to cylindrical optical pumping cells (described in Chapter 3). For this geometry and for the particular case where G is perpendicular to the cylinder axis, the relationship between D_{eff} and D_0 is

$$D_{eff} = \frac{3}{D_0 \tau^3} \sum_{n=1}^{\infty} \frac{\alpha_n^{-4}}{\alpha_n^2 R^2 - 1} \left(2\tau - \frac{3 - 4\exp\left(-\alpha_n^2 D_0 \tau\right) + \exp\left(-\alpha_n^2 D_0 2\tau\right)}{\alpha_n^2 D_0}\right),$$ (2.59)

where α_n is the nth root of $J_1'(\alpha_n R)$ and J_1 is a Bessel function and R is the radius of the cylinder [56].

If T_1 and T_2^* are long compared to the gradient application time it is possible to use a GRSE to measure D_{eff}. This can be done by measuring the amplitude of the FID immediately before and after the bipolar gradient pulse [5]. These amplitudes represent M_0 and M, respectively. Using this information and Eq. 2.56 it is possible to determine D_{eff}, and hence, D_0.
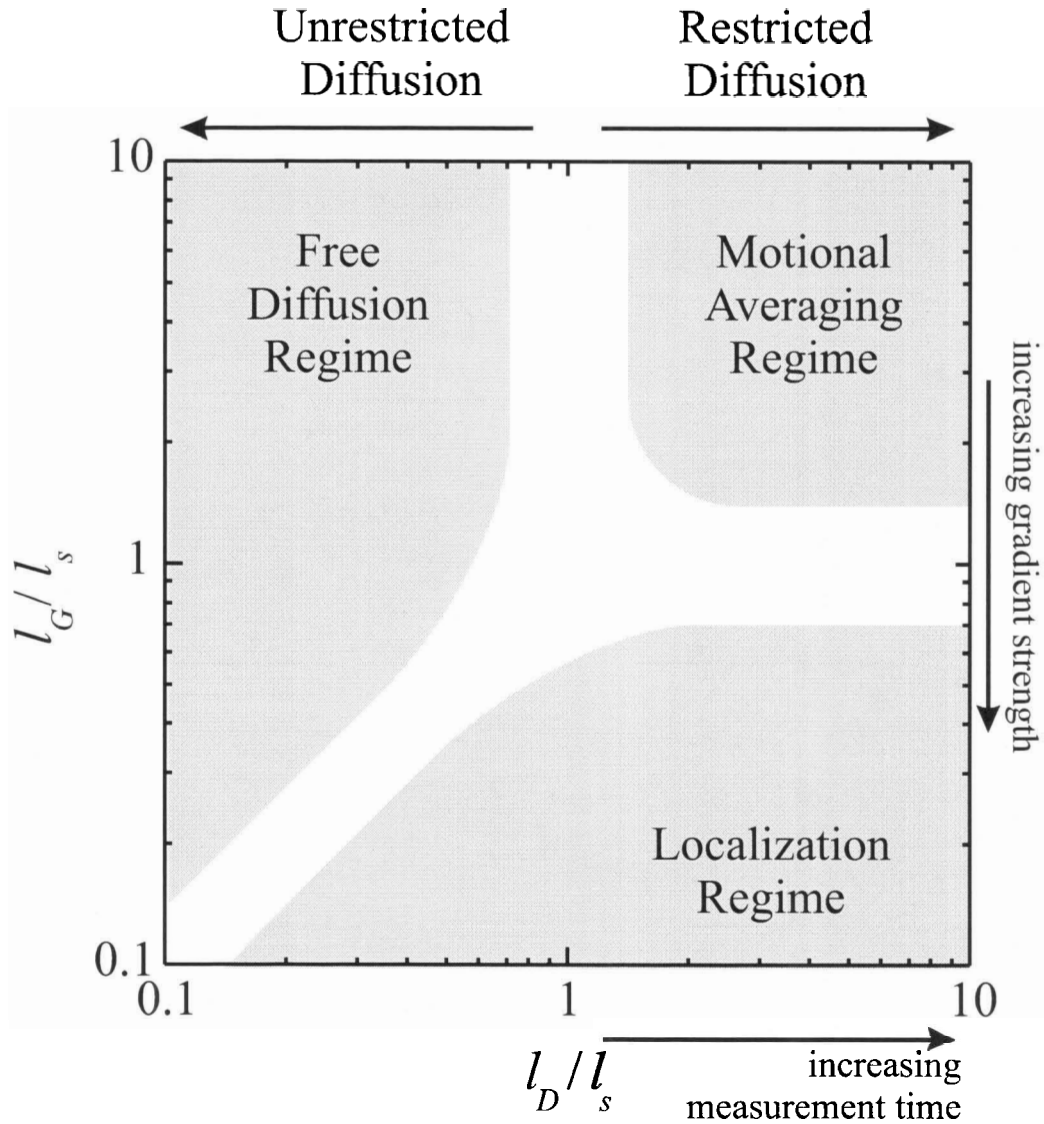
Figure 2.8: The attenuation of the transverse magnetization caused by diffusion in the presence of a gradient exhibits three types of behavior depending on the relative sizes of ℓ_D, ℓ_s, and ℓ_G. This figure has been reproduced with the permission of Dr. Mike Hayden and has been adapted from Fig. 1 of reference [5].

2.4   Very Low-Field NMR

In recent years, the feasibility of performing NMR and MRI in very low magnetic fields has been examined [4–10]. In this thesis, measurements corresponding to the GRSE experiment described above are reported for ^{3}He gas in a homogeneous magnetic field of approximately 6 Gauss. At this field strength, additional considerations must be taken into account. In particular, it becomes relatively straight forward to make the characteristic radius of curvature $R_c = B_0/G$ (introduced in Chapter 1) comparable to sample dimensions. That is, whenever a gradient field is applied, perpendicular gradients are also created as demanded by Maxwell's equations. These concomitant gradients distort what would otherwise be planes of constant precession frequency and complicate the evolution of spin coherences. The first subsection below explains the origin of concomitant gradients and describes the form they take when a Golay coil arrangement is used to generate a gradient directed perpendicular to B_0. The second subsection describes a method for evaluating the influence of concomitant gradients on a FID during the application of a field gradient.

2.4.1   Concomitant Gradients

In general, the gradient G of a magnetic field B is a tensor quantity with the following form:

$$G \equiv \begin{bmatrix} \frac{\partial B_x}{\partial x} & \frac{\partial B_x}{\partial y} & \frac{\partial B_x}{\partial z} \\ \frac{\partial B_y}{\partial x} & \frac{\partial B_y}{\partial y} & \frac{\partial B_y}{\partial z} \\ \frac{\partial B_z}{\partial x} & \frac{\partial B_z}{\partial y} & \frac{\partial B_z}{\partial z} \end{bmatrix} . \tag{2.60}$$

Maxwell's equations require that

$$\nabla \cdot \mathbf{B} = \frac{\partial B_x}{\partial x} + \frac{\partial B_y}{\partial y} + \frac{\partial B_z}{\partial z} = 0 , \tag{2.61}$$

and

$$\nabla \times \mathbf{B} = \left(\frac{\partial B_z}{\partial y} - \frac{\partial B_y}{\partial z} \right) \hat{\imath} + \left(\frac{\partial B_x}{\partial z} - \frac{\partial B_z}{\partial x} \right) \hat{\jmath} + \left(\frac{\partial B_y}{\partial x} - \frac{\partial B_x}{\partial y} \right) \hat{k} = 0 \tag{2.62}$$

for a static magnetic field in free space. These four relationships imply that only five of the nine components of the gradient are independent. Identity 2.60 can be written

$$G \equiv \begin{bmatrix} \frac{\partial B_x}{\partial x} = -\frac{\partial B_y}{\partial y} - \frac{\partial B_z}{\partial z} & \frac{\partial B_x}{\partial y} = \frac{\partial B_y}{\partial x} & \frac{\partial B_x}{\partial z} = \frac{\partial B_z}{\partial x} \\ \frac{\partial B_y}{\partial x} & \frac{\partial B_y}{\partial y} & \frac{\partial B_y}{\partial z} = \frac{\partial B_z}{\partial y} \\ \frac{\partial B_z}{\partial x} & \frac{\partial B_z}{\partial y} & \frac{\partial B_z}{\partial z} \end{bmatrix} , \tag{2.63}$$

which indicates that only two of the diagonal terms are independent and the off diagonal terms must be symmetric. This implies that the application of a gradient in any direction must produce gradients in other, orthogonal directions.

For the experimental work described in this thesis, gradients are produced using Golay coils (a quadrupolar arrangement of saddle coils). One Golay coil generates a nominally linear gradient $\frac{\partial B_z}{\partial y}$ along the y-axis while another generates a nominally linear gradient $\frac{\partial B_z}{\partial x}$ along the x-axis. If the static magnetic field defines the z-axis, the magnetic field during application of a gradient pulse is

$$B = B_0 k + G \cdot r . \tag{2.64}$$

However, referring to Identity 2.63, when $\frac{\partial B_z}{\partial y}$ is nonzero, $\frac{\partial B_y}{\partial z}$ must also be nonzero and of equal magnitude. Close to the centre (isocentre) of the Golay coils this leads to a magnetic field

$$B = Gz j + (B_0 + Gy) k . \tag{2.65}$$

The gradient of the magnitude of this magnetic field is

$$\nabla |B| = \frac{G}{|B|} [(B_0 + Gy) j + Gz k] . \tag{2.66}$$

An important feature of this geometry is the fact that $|\nabla |B||^2 = G^2$, which is independent of position.

Magnetic field lines provide a useful construct for visualizing the influence of concomitant gradients during the application of a gradient. Magnetic field lines represent the local direction and strength of the field. The direction of the field line indicates the direction of the field, while the density of field lines indicates the magnitude of the field. If B_0 is large and a Golay coil is employed, magnetic field lines will tend to be straight and vary in density along the transverse direction. However, if Gz and Gy are comparable to B_0, then the

field lines will curve (see Fig. 2.9). Particular care must be taken when performing NMR experiments in regions where this curvature is large, as discussed in the next subsection.

2.4.2 Attenuation Caused by Concomitant Gradients

Thus far, the attenuation of FID amplitudes that results from the irreversible loss of magnetization associated with diffusion in the presence of a field gradient has been discussed. The presence of concomitant gradients also contributes to the attenuation of FIDs during a GRSE because of inexact rephasing [3]. During the application of a gradient, the plane of precession of M will not be perpendicular to B_0. Instead, continuing to use the example of a Golay coil intended to produce a $\frac{\partial B_z}{\partial y}$ gradient, M will rotate about B with Larmor frequency

$$\omega = \gamma |B| = \gamma \sqrt{(B_0 + Gy)^2 + (Gz)^2} \ . \qquad (2.67)$$

If static spins are considered, this leads to a position dependent phase accumulation ϕ, over the gradient application time τ, that is equal to

$$\phi(y,z) = \int_0^\tau dt\, \gamma |B| \ . \qquad (2.68)$$

The phase accumulated over both lobes of a bipolar gradient is

$$\begin{aligned}
\phi(y,z) &= \int_0^\tau dt\, \gamma \sqrt{(B_0 + G(t)y)^2 + G(t)^2 z^2} \\
&\quad + \int_\tau^{2\tau} dt\, \gamma \sqrt{(B_0 - G(t)y)^2 + G(t)^2 z^2} \ . \qquad (2.69)
\end{aligned}$$

If $B_0 \gg Gy$ and Gz, the accumulated phase is position independent. However, if B_0 is comparable to changes in the field associated with the gradient, the accumulated phase depends on Gz, Gy and B_0. This in turn implies that for a sample of finite extent (eg. volume V), the amplitude of the detected signal

$$M \propto \int_V e^{-i\phi(y,z)} dV \ , \qquad (2.70)$$

will in general be attenuated.

It is instructive to illustrate the influence of concomitant gradients using a one-dimensional model of a cell of length $2L$ placed along the z-axis of the magnet, but displaced a distance d

(a) Positive Gradient

(b) Negative Gradient
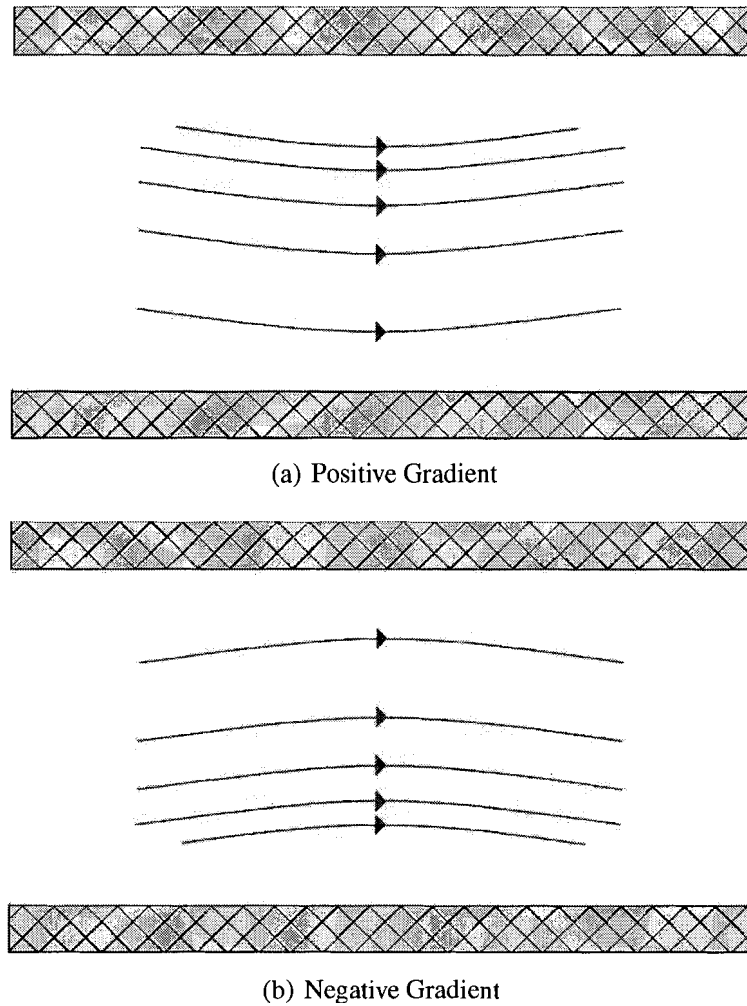
Figure 2.9: The influence of concomitant gradients on magnetic field lines. This figure shows the magnetic field lines inside a solenoid during the application of a transverse gradient (the sides of which are represented by the rectangle). Figure 2.9(a) displays the shape of the field lines when a positive gradient is applied. Figure 2.9(b) displays the shape of the field lines when a negative gradient is applied.

from the isocentre. If a transverse gradient $\frac{\partial B_z}{\partial y}$ is applied, the z-component of the magnetic field is

$$B_z(z) \approx B_0 \left(1 - \frac{G^2 z^2}{B_0^2} \right) . \tag{2.71}$$

Ignoring spin dephasing in y-z plane, the leading order contribution to the magnetization of the spins after a symmetric bipolar pulse is

$$M(z) \propto \exp(2i\gamma B(z)\tau) . \tag{2.72}$$

Integrating over the length of the cell to obtain the average complex magnetization viewed by pickup coils oriented in the y-z plane leads to

$$M \propto \frac{\sqrt{\pi}}{4LG} \sqrt{\frac{2B}{i\gamma\tau}} \exp(2\gamma B\tau) \left[\mathrm{erf}\left(\sqrt{\frac{2i\gamma\tau}{B}} G(d+L) \right) + \mathrm{erf}\left(\sqrt{\frac{2i\gamma\tau}{B}} G(d-L) \right) \right] . \tag{2.73}$$

where erf denotes the error function. Figure 2.10 shows M calculated for a 10 cm cell displaced 5 cm from the isocentre over a range of gradient strengths. An interesting feature is the appearance of a node. This is discussed further in subsection 6.3.2. The periodicity of these nodes is caused by the error functions (which have complex arguments). The frequency of oscillation of the error functions is determined by L and G.

It is important to note that concomitant gradients do not have an effect on the results of a PGSE sequence (see Fig. 2.6) if diffusion can be ignored. In this pulse sequence the phase accumulated over both lobes of gradient field will be

$$\phi(y,z) = \int_0^\tau dt \, \gamma \sqrt{(B_0 + G(t)y)^2 + G(t)^2 z^2}$$
$$- \int_\tau^{2\tau} dt \, \gamma \sqrt{(B_0 + G(t)y)^2 + G(t)^2 z^2} = 0 . \tag{2.74}$$

Therefore, concomitant gradients will not have an influence on the amplitude of the FID from a PGSE sequence as long as the gradient pulses are applied for the same duration and the spins remain immobile.
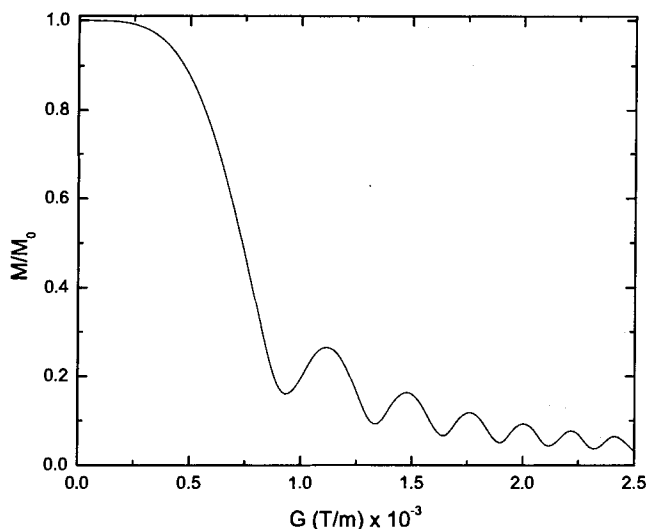
Figure 2.10: The calculated net transverse magnetization of a 10 cm one-dimensional cell displaced 5 cm from the isocentre after a bipolar gradient pulse.

2.5 NMR Signal Analysis

To characterize the attenuation of a FID during a GRSE sequence it is necessary to determine the amplitude of the FID immediately before and after the bipolar gradient pulse. It is thus necessary to analyze the recorded signal (discussed in subsection 2.3.4) and determine the amplitude of the transverse magnetization M as well as the decay time of the transverse magnetization T_2^*. There are several methods for analyzing the signal to extract these parameters. However, both the accuracy and the precision of the extracted parameters are dependant on the Signal-to-Noise Ratio (SNR) of the signal. There are two categories of noise present in the recorded signals: amplitude noise and frequency noise. In this thesis, data nominally conforming to the complex sinusoid represented by Eq. 2.48 is analyzed in the time domain using a least squares minimization routine. An alternate and computationally simpler method is to fit the magnitude of the detected signal to an exponential decay. The latter approach is not influenced by frequency noise but is susceptible to a systematic bias (known as Rician noise) in low SNR regimes [58, 59]. Rician noise is a direct result of

processing data containing Gaussian noise.

The first subsection below describes characteristics of the noise present in the recorded signal. The subsequent subsection discusses the origin and consequence of Rician noise on analysis methods that rely on fits to the magnitude of the detected signal. It follows the treatment of A. Papoulis [60].

2.5.1 Noise Characteristics

Amplitude noise is caused by three different sources (in order of decreasing importance): noise added when amplifying the weak signal, background magnetic noise, and Johnson noise originating from the NMR coils. Additive noise results from the amplification of the voltage induced across the receiver coils. The front end of the amplifier is not perfect and contributes noise that is added to the resultant output. Background noise results from inductive and capacitive coupling of the coils to sources other than the precessing nuclei. An efficient method for shielding against low-frequency background magnetic noise is used for the work described in this thesis and is discussed in Chapter 3. Finally, Johnson noise is caused by random thermal motion electric charges inside a conductor. The experimentally determined amplitude noise has Gaussian characteristics (see Fig. 3.13).

Frequency noise is caused by fluctuations in the effective magnetic field. Fluctuations in the magnetic field cause the Larmor frequency of the nuclei and hence the frequency of the detected signal to fluctuate. The spectral density of frequency fluctuations for almost all real frequency sources can be fit by a model that involves a sum over terms of the form $S(f) \sim f^{\alpha}$ for $-2 \leq \alpha \leq 2$ [61]. In this thesis, two types of frequency noise were present in the measured signals: random-walk (corresponding to $\alpha = 0$) and drift frequency noise (corresponding to $\alpha = -2$). Random walk frequency noise originates from random fluctuations in the magnetic field. These are caused by background noise and by random fluctuations in the current driving the solenoid. Drift frequency noise is caused when the Larmor frequency of nuclei drifts in a systematic way. In the experiments in this thesis, drift frequency noise is correlated with two sources: the motion of a nearby elevator and the stability of the current source that drives the solenoid. Characteristics of the noise associated with the apparatus used in this thesis are contained in the Chapter 3.

2.5.2   Rician Bias

NMR data correspond to two sinusoids that are in quadrature with each other. One method of extracting the amplitude and characteristic decay time from this data is to fit an exponential curve to the magnitude of the FID (i.e. the square root of the sum of the squares of the two sinusoids). This method removes any consideration of the frequency or phase of the two sinusoids. In regimes of high SNR, it can be used to obtain accurate determinations of the amplitude and decay time. However, in regimes of low SNR (SNR < 5), a non-negligible, systematic bias is incurred.

In order to understand the origin of this bias, consider two gaussian distributed random variables, x and y. In terms of the experiments performed in this thesis, these two random variables represent the two recorded voltage signals from the receiver coils. For this argument, the standard deviation σ of the two noise sources will be considered to be the same. The probability distribution functions (PDF) for x and y are

$$f(x) = \frac{1}{\sigma\sqrt{2\pi}} e^{\frac{-(x-\eta_R)^2}{2\sigma^2}} \tag{2.75}$$

$$f(y) = \frac{1}{\sigma\sqrt{2\pi}} e^{\frac{-(y-\eta_I)^2}{2\sigma^2}} , \tag{2.76}$$

where η_R and η_I are the mean values of the variables x and y, respectively. The PDF of the magnitude of the two signals, $z = \sqrt{x^2 + y^2}$, is given by

$$f_z(z)dz = \int\int_{\Delta D_z} f(x,y)dxdy , \tag{2.77}$$

where ΔD_z is the region of the xy plane such that $z < \sqrt{x^2 + y^2} < z + dz$. If the random variables are independent, then

$$f(x,y) = f_x(x)f_y(y) ;$$

or

$$f(x,y) = \frac{1}{2\pi\sigma^2} e^{\frac{-[(x-\eta)^2+y^2]}{2\sigma^2}} , \tag{2.78}$$

where $\eta = \sqrt{\eta_R^2 + \eta_I^2}$. Using the substitutions

$$x = z\cos\theta \qquad y = z\sin\theta \qquad dxdy = zdzd\theta ,$$

it follows that

$$f_z(z)dz = \frac{1}{2\pi\sigma^2} \int_0^{2\pi} e^{\frac{-[(z\cos\theta-\eta)^2+(z\sin\theta)^2]}{2\sigma^2}} zdzd\theta \qquad (2.79)$$

or

$$f_z(z)dz = \frac{z}{2\pi\sigma^2} e^{\frac{-(z^2+\eta^2)}{2\sigma^2}} \int_0^{2\pi} e^{\frac{z\eta\cos\theta}{\sigma^2}} d\theta . \qquad (2.80)$$

This reduces to

$$f_z(z) = \frac{z}{\sigma^2} I_0\left(\frac{z\eta}{\sigma^2}\right) e^{\frac{-(z^2+\eta^2)}{2\sigma^2}} , \qquad (2.81)$$

where I_0 is a modified Bessel function of the first kind. This is the expression for a Rician noise distribution [58, 59]. Fig. 2.11 displays the shape of this distribution for different levels of the ratio z/σ^2 (i.e. SNR). At large values of SNR, the Rician distribution has the same properties as the Gaussian distribution. At low values of SNR (SNR < 5) the Rician distribution is different. Consider, for example, two Gaussian distributed variables with a mean value of 0. The magnitude of these two variables will have a nonzero mean value because of the systematic error introduced by the Rician distribution. In terms of the experiments in this thesis, when SNR is low (i.e. FID amplitude is low compared to the accompanying amplitude noise) models that fit to the magnitude of a FID will incur a systematic bias. In other words, the accuracy of parameters extracted from fits to the magnitude of the data is degraded, even if the precision of these determinations remain good.
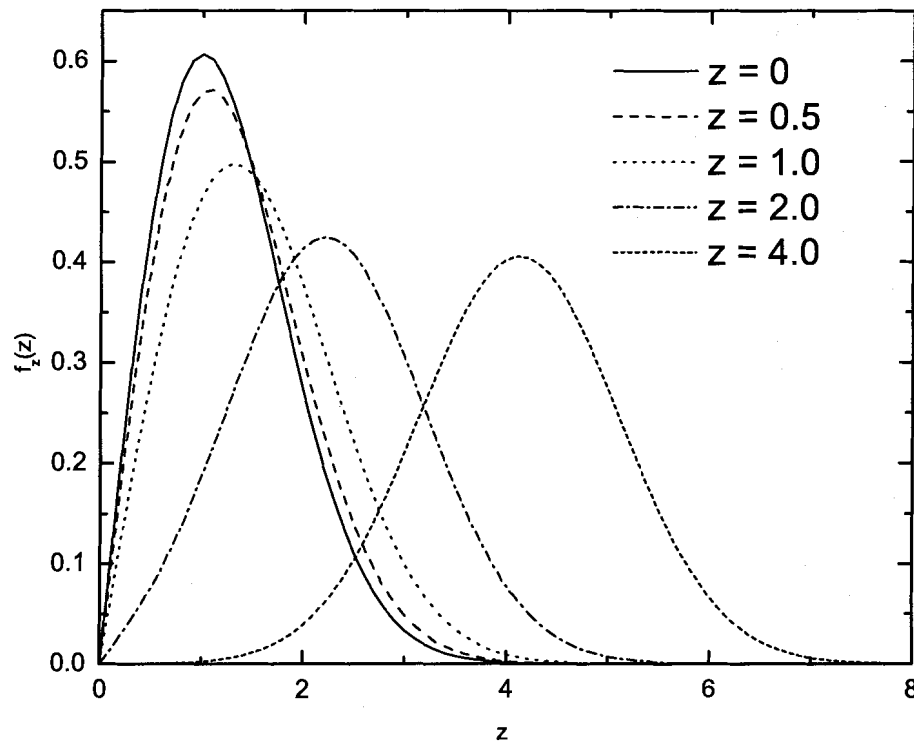
Figure 2.11: The shape of a Rician distribution for various values of the ratio z/σ^2. The standard deviation σ is held constant at a value of 1 as z is varied. As the ratio decreases, the peak of the Rician distribution and the value of z differ.

Chapter 3

Apparatus

The central investigation described in this thesis involves a study of the influence of concomitant gradients on the outcome of experiments that probe the diffusion of hyperpolarized ^{3}He in a restricted geometry. This chapter contains descriptions of the apparatus used to polarize the helium, the storage cells that serve to confine the gas, and the equipment used to perform NMR experiments.

3.1 Optical Pumping Apparatus

Metastability Exchange Optical Pumping (MEOP) was used to polarize ^{3}He gas confined to cylindrical glass cells with optical flats on either end. A 10 MHz radio frequency discharge was used to populate the 2^3S_1 metastable state. A circularly polarized beam of coherent 1083 nm light was then used to induce large nuclear polarizations. The following subsections outline the optical pumping (OP) cells, discharge source and optics associated with the polarization apparatus.

3.1.1 Optical Pumping Cells

The ^{3}He used in this work was confined to sealed cylindrical OP cells. These cells were fabricated, cleaned, sealed and characterized previously at Simon Fraser University and at the Ecole Normale Supérieure [62, 63]. They were constructed from borosilicate glass tubes with an approximate outer diameter of 5 cm, and a wall thickness of 0.15 cm. Optical
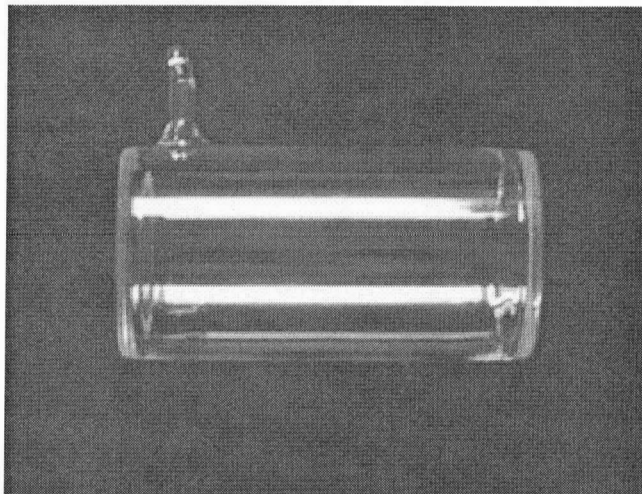
Figure 3.1: An optical pumping cell.

flats with an approximate diameter of 5.0 cm and an approximate thickness of 0.3 cm were attached to the ends of the cylinders in order to provide undistorted optical access to the gas confined in the cells. Cells with two different internal lengths were used for the experiments in this thesis: 8.7 cm and 3.4 cm. In addition to the cylindrical tube and the optical flats, a fill tube was attached to the walls of the OP cell. A photograph of an OP cell is shown in Fig. 3.1. The cells were cleaned using an intense microwave discharge in order to remove as many contaminants as possible. Once clean, ^{3}He was metered into the cell to a final pressure of either 1 Torr or 6 Torr at 293 K. At room temperature the ^{3}He diffusion coefficients at these pressures are 0.140 m^2/s and 0.023 m^2/s [5]. The fill tube was then flame-sealed using a torch. With this production method, OP cells consistently yielded intrinsic longitudinal nuclear relaxation times T_1 longer than 140 minutes at 293 K [62]. This decay is associated with diffusion of ^{3}He into the glass matrix of the OP cell [64]. Table 3.1.1 lists the inner dimensions, gas pressure and role of the three cells used in this thesis.

The OP cell with an inner length of 3.4 cm was only used for shimming the low field magnet (see subsection 3.2.1) while the two OP cells with an inner length of 8.7 cm were used for the experiments outlined in Chapter 4. The T_2^* decay time of a FID is inversely proportional to the square of the gradient. In a gradient, the shorter OP cell will produce a FID with a larger T_2^* decay time than the longer OP cells. However, a smaller cell contains fewer nuclei and thus produces a smaller FID than a larger cell would. Typically, T_2^* decay times of order 10 s were obtained in the OP cell B once the magnet was shimmed.

Cell	Identification Number	Diameter	Length	^{3}He Pressure	Function
A	JB18397	4.7 cm	3.4 cm	0.993 Torr	Shimming
B	CL20010525	4.5 cm	8.8 cm	1.004 Torr	Attenuation
C	CB20040325	4.9 cm	8.7 cm	6.002 Torr	Attenuation

Table 3.1: The inner dimensions, ^{3}He pressure at 293 K, and role played by the three OP cells used in this thesis.
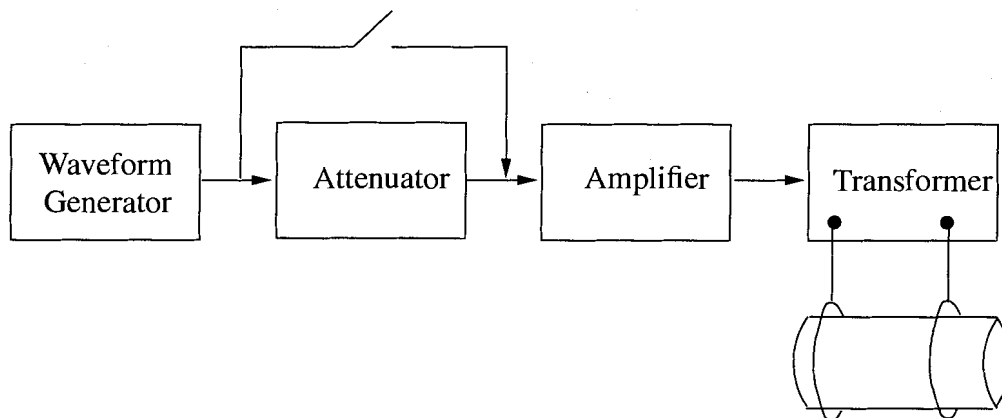
Figure 3.2: A block diagram illustrating the apparatus used to create the 10 MHz radio-frequency discharge within the optical pumping cell.

3.1.2 10 MHz Radio Frequency Discharge Source

Metastable exchange optical pumping of ^{3}He requires that the metastable 2^3S_1 electronic state be populated. By imposing a strong oscillating electric field within the OP cell, a (radio-frequency) discharge is ignited that populates the metastable state through radiative cascade processes. A block diagram of the apparatus used to create the discharge is shown in Fig. 3.2.

A low-level radio frequency sine wave produced using an Agilent 33120A waveform generator. The sine wave was subsequently fed into a Nicolet Magnetics Corporation, Model 881-0041000, 150 W amplifier that provided a gain of approximately 45 dB. The output from the amplifier was then passed through a balanced, step-up transformer. The transformer was coupled to an OP cell with a pair of leads that were wrapped around either
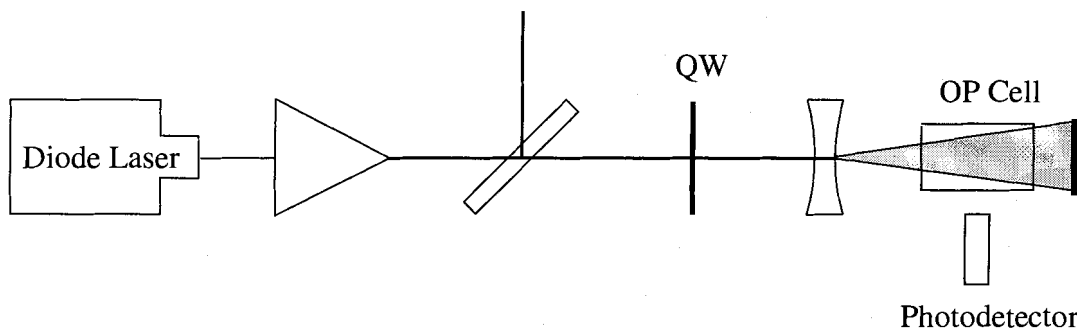
Figure 3.3: A block diagram detailing the beam source and optics.

end of the cell (see Fig. 3.2). Typically, the potential difference used to drive the discharge was in the range of 225-675 V and oscillated at a frequency of 8-11 MHz.

Typically a weak discharge, close to extinction, is desired for low-field ^{3}He MEOP applications [65]. A strong electric field is necessary to ignite the discharge but it can be maintained at much lower levels. To facilitate ignition of the discharge a switch was inserted to momentarily bypass the 10x attenuator shown in Fig. 3.2. When depressed, a large oscillating electric field (sufficient to ignite the discharge) is applied across the cell. After the discharge is created, the attenuator can be activated and the discharge is maintained, only at a much lower level.

3.1.3 Optics

Once a discharge has been ignited, the 2^3S_1 metastable state is rapidly populated and the optical pumping process commences. Fig. 3.3 summarizes the optical components used to generate and collimate the beam of circularly polarized light resonant with the C_9 transition at 1083 nm that is passed through the OP cell.

The beam source was a Spectra Diode Laboratories SDL-6702-H1 GaAlAs 50 mW diode laser mounted on a SDL-800-H heat sink and controlled by a SDL-803 driver. The diode incorporates a distributed Bragg reflector that enables tuning of the laser wavelength with changes in the operating temperature of the device. The temperature was finely adjusted with an external dc voltage derived from a 1.5V battery. The output power of the laser diode was approximately 15 mW. The spectral linewidth of the diode is approximately 10 MHz. This is much narrower than the 2 GHz Doppler width of the 2^3S_1-2^3P transition at

295 K which limits the fraction of atoms that are optically pumped with this diode. The output of the diode has a divergence of 30° along the x-axis and 10° along the y-axis. A converging lens was used to focus the SDL output onto the end of an optical fibre that fed a IPG Photonics Corporation YAD-1-1083 Ytterbium Fiber Amplifier. The output power from the amplifier was approximately 250 mW.

The optical components through which the laser beam passes produces a circularly polarized and roughly collimated beam that is directed through the OP cell. The beam first passes through a polarizing beamsplitter cube that splits the laser beam into two orthogonal, linearly, polarized components. The reflected beam is discarded into a light-absorbing shield. The transmitted beam passes through a quarter-wave plate aligned at 45° to the polarization axis of the beam splitting cube, and is thus transformed into circularly polarized light. Finally, the circularly polarized light passes through a lens that provides a gently diverging beam comparable in diameter to the OP cell. A mirror placed at the far end of the OP cell retroreflects the transmitted light, doubling the rate at which photons are absorbed by the gas.

The laser was tuned to 1083.031 nm to pump the C_9 transition (Fig. 2.2) between the 2^3S_1 metastable state and the 2^3P state. This transition was specifically chosen because experimental evidence shows that at low field it yields a higher maximum polarization than other transitions [65]. The laser was tuned by monitoring the intensity of the 1083 nm light emitted from the discharge while adjusting the operating temperature of the diode laser. The light intensity was monitored with a Thorlab DET-110 Si photodetector placed at a right-angles to the laser beam to only detect emitted light from the discharge. The photodetector was shielded with a 10 nm bandpass filter with a centre wavelength of 1080 nm. The intensity of the 1083 nm light emitted by the discharge is directly proportional to the rate of transitions from the 2^3P state to the 2^3S_1 state. Figure 3.4 displays the relationship between the photodetector output and the wavelength of the laser. Based on previous experiments performed with a similar apparatus, the polarization of the gas is expected to be of order 20% [62].
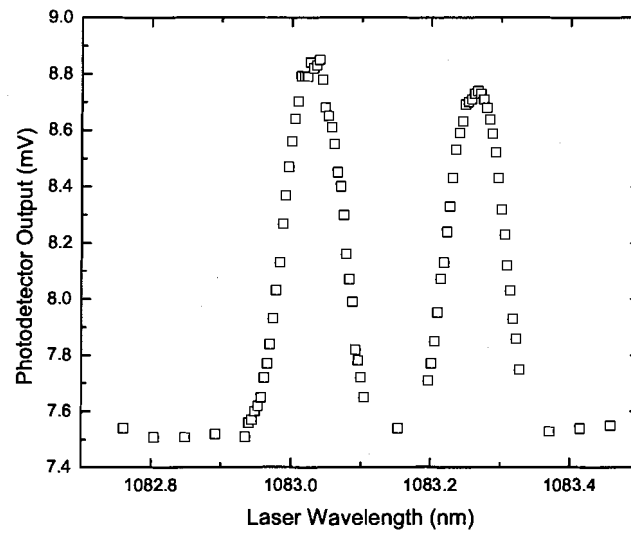
Figure 3.4: The output from the photodetector as the wavelength of the laser was varied. The left peak corresponds to the C_9 transition while the right peak corresponds to the C_8 transition.

3.2 Low-Field Nuclear Magnetic Resonance Apparatus

The nuclear magnetic resonance apparatus used for this experiment consists of several different components: a solenoid to provide a homogeneous static magnetic field, transmit coils that provide oscillating magnetic fields perpendicular to the homogeneous magnetic field, receiver coils that detect the precession of nuclear spins and a system of electronics used to amplify, demodulate and record the electronic signal. This apparatus is discussed in the following subsections.

3.2.1 Low-Field Magnet

A Magnex Scientific whole body resistive MRI magnet and gradient set was used to provide a static magnetic field B_0, to provide linear magnetic field gradients, and to provide shim fields in order to optimize the homogeneity of B_0. A photograph of the MRI magnet is shown in Fig. 3.5. All the above components are housed in a cylinder with an outer diameter of 71.1 cm, inner diameter of 55.0 cm and a length of 122 cm. For the purposes of this thesis positions and directions within the cylinder will be discussed in Cartesian coordinates. The z axis of this reference system is aligned with the axis of the magnet and the x and y axes are aligned with the horizontal and vertical directions, respectively. The origin of this coordinate system is at the isocentre and corresponds to the point in space about which the x, y, and z gradients pivot. The isocentre is displaced by 6 mm along the positive z axis from the geometric centre of the cylinder.

The static field is produced by a solenoid and is thus directed along the z-axis. This magnet has a maximum field strength of 0.01T. A static field of 630 μT was used for the work described here corresponding to a ^{3}He Larmor frequency of 20.4 kHz. The intrinsic homogeneity of this magnet is < 100 ppm over a 25 cm diameter spherical volume (DSV). The current to drive the solenoid was provided by a Hewlett-Packard 6002A DC Power Supply and was typically 1.8 A. The power supply is rated for a current drift of 0.05% + 5 mA/8 hours. Figure 3.6 displays an example of the measured magnetic field drift that is attributed to systematic changes in current. Typically, the current was seen to drift by 0.1 mA over an 8 s FID acquisition period. This corresponds to a systematic drift in the static magnetic field of 10 nT. In addition, random fluctuations were also present in the static magnetic field. The random fluctuations could be characterized by a guassian distribution
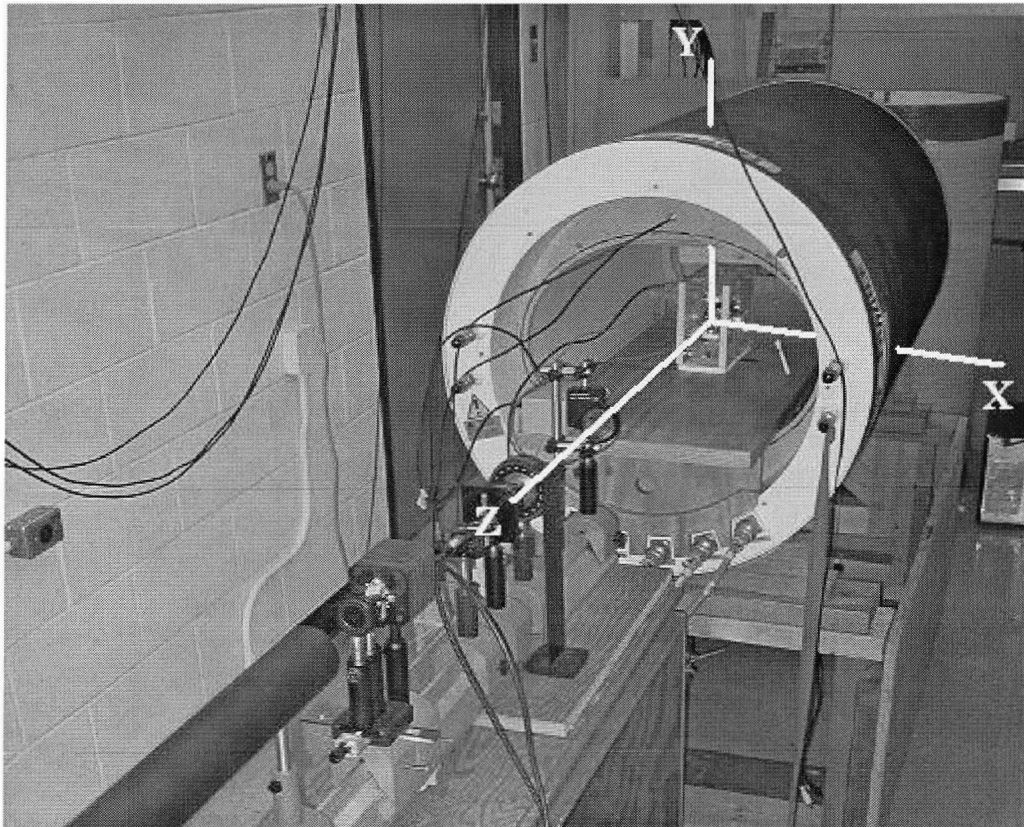
Figure 3.5: The Magnex Scientific resistive magnet and gradient set. The magnet is the large cylinder in the background of the figure. The alignment of the coordinate system with respect to the magnet is also specified.
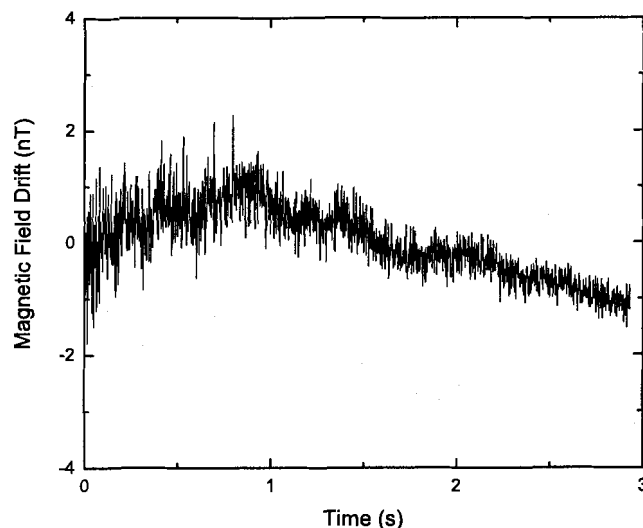
Figure 3.6: An example of the drift in the magnetic field during the acquisition of a FID. This drift is caused by systematic variations in the current used to drive the solenoid. This plot was generated by extracting the frequency of a FID using a sliding window. The frequency variation is directly proportional to the magnetic field variation (see Eq. 2.33).

with a standard devation of 1 nT.

As well as the primary solenoid, this MRI magnet has 16 additional sets of coils: three gradient coils and 13 shim coils. The gradient coils are used to produce linear magnetic field gradients along the x, y, and z directions. The z gradient is produced by a pair of Maxwell coils wound from copper strip and was driven by a Hewlett-Packard 6002A DC Power Supply. The z gradient has a linearity of < 1.5% over a 25 cm DSV. The x and y gradients were produced using Golay coils made from sheet copper and were driven by two Techron 8607 Gradient Amplifiers. The x and y gradients have a linearity of <2% over a 25 cm DSV. The characteristics of the Gradient Amplifiers are discussed further in subsection 3.2.3.

The shim coils produce higher order magnetic field gradients with various symmetries and are primarily used to suppress inhomogeneities arising from the background field. The shim coils were driven with a Compushim power supply. Only those coils providing z^2, z^3,
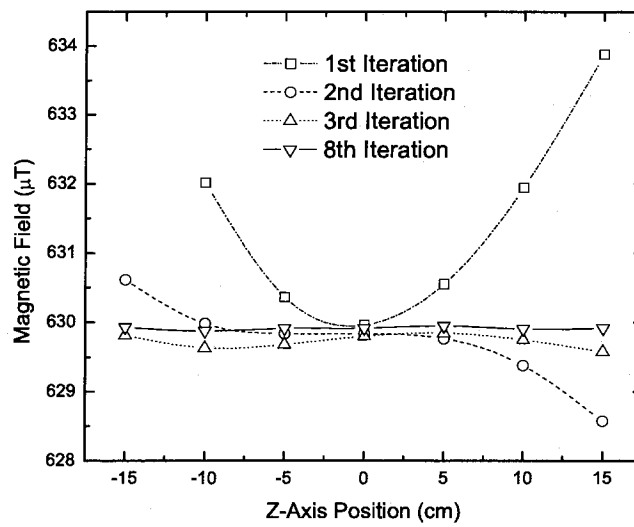
Figure 3.7: The magnetic field strength during the shimming process. After the 1st iteration, the z shim coil was turned on. After the 2nd iteration, the z^2 shim coil was turned on. After the 3rd iteration, the z^3 shim coil was turned on. Iterations after that involved modifying each of the shim field strengths until, by the 8th iteration, the field profile varied by approximately 30 nT over a 30 cm range centred at the gradient isocentre. The spatial resolution of each point is of order 3 cm.
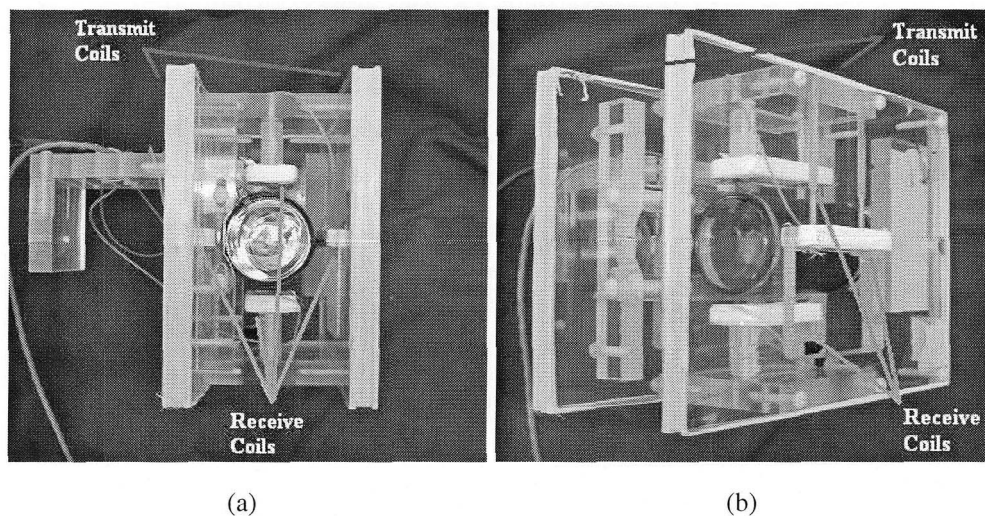
Figure 3.8: Two photographs showing the placement of the transmit and receive coils with respect to the OP cell.

z^4 and x^2-y^2 symmetries were used for the experiments described in this thesis. The magnetic field was shimmed using an iterative technique. By measuring the Larmor frequency of the FID from OP cell A (and hence the magnetic field strength) at various positions within the magnet it was possible to generate a field map. After this map was determined, one of the shim coils would be adjusted in an effort to produce a flatter profile. The magnetic field measurements would then be repeated to determine the field map. This procedure was repeated for each shim coil until the magnetic field was as homogeneous as possible. Figure 3.7 shows the results of a series of measurements along the z-axis of the magnet after 1, 2, 3, and 8 iterations of shim coil settings. This procedure was repeated along the x- and y-axes as well. After shimming was finished, the magnetic field variations inside a 10 cm by 10 cm by 12 cm volume were of order 30 nT. The FID from the OP cell B placed in this volume had a characteristic T_2^* time on the order of 10 seconds.

3.2.2 Transmit and Receive Coils

Separate from the magnet and gradient coils are two additional systems of coils: the transmit coils used to create a uniform, oscillating $\mathbf{B}_1$ field, and receive coils across which a voltage signal was induced by the precession of nuclei. Figure 3.8 shows the relative orien-

tation of the transmit and receive coils as well as the placement of an OP cell between the coils. The OP cell is positioned at the centre of the apparatus.

The transmit coils consist of two rectangular coils that form a quasi-Helmholtz pair. They are connected in series and placed on either side of the OP cell. Each coil was wound using 35 turns of #23 AWG wire wrapped around a rectangular piece of PMMA that was 20 cm by 15 cm. Collectively, the coils had a resistance of 24 Ω and an inductance of 1.13 mH. The coils were placed in series with a 55 nF capacitor creating an RLC circuit resonate at 20.4 kHz. The capacitor was added to counteract the inductive impedance of the circuit. The Q value of this circuit was 6. The coils were oriented parallel to the y-z plane so as to produce an oscillating magnetic field perpendicular to the static magnetic field.

The receive coils consisted of two pairs of coils placed symmetrically around the OP cell. Each coil was wound using 125 turns of #23 AWG wire around a rectangular piece of PMMA that was 6 cm by 2 cm. The coils were interconnected such that one pair of coils was wound in the opposite sense to the other pair. The coils had to be tuned to detect nuclear precession at 20.4 kHz. Collectively, the coils had a resistance of 46 Ω and an inductance of 4.88 mH. The coils were placed in parallel with a 12.6 nF capacitor creating an RLC circuit that resonated at 20.4 kHz. The Q value of this circuit was 18. The static magnetic field was set so that the Larmor frequency was close to this resonant frequency. The plane of the receive coils was parallel to the x-z plane and orthogonal to the transmit coils so that the coupling between the transmit and receive coils would be minimal.

The winding sense of the receive coil pairs was specifically chosen to diminish the effect of external oscillating magnetic fields. This is illustrated in Fig. 3.9. Since the four coils are identical, distant sources of oscillating magnetic fields will induce a voltage signal in one pair of coils that is exactly the opposite that is induced in the other pair. This results in a null output from the coils. However, the EMF induced across all four coils by precessing nuclei in the volume situated between the coils is additive.

3.2.3 Electronics

A number of instruments were used to generate B_1 pulses, drive gradient fields, and record the nuclear induction signal from the receive coils, as summarized in Fig. 3.10. The system was controlled by a Tecmag Apollo LF spectrometer running NTNMR Version 2.3.7.
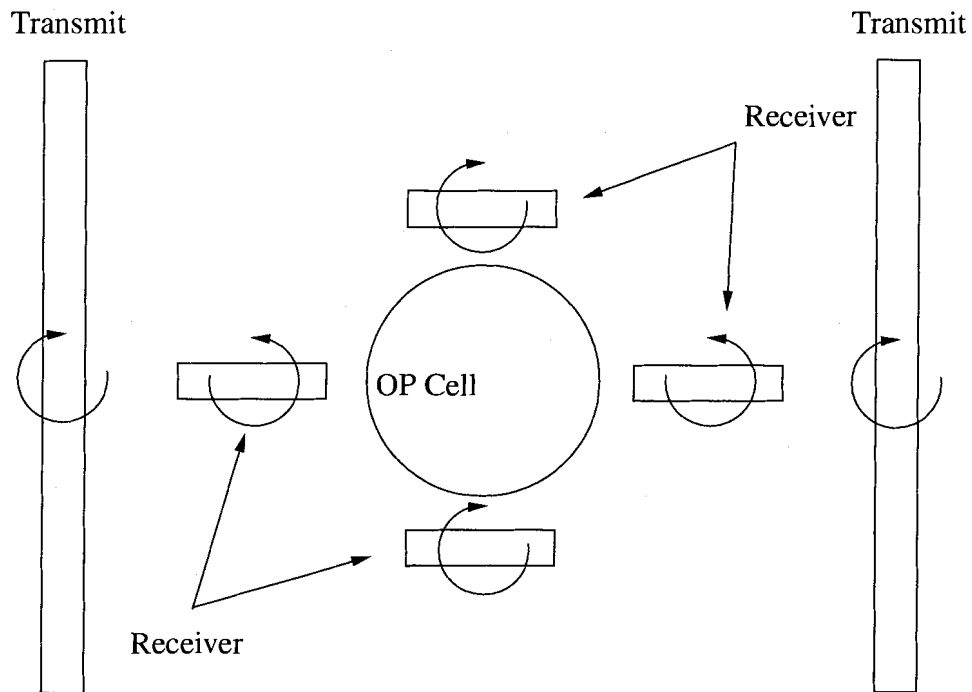
Figure 3.9: The winding sense of the two transmit coils and four receive coils. The curved arrows represent the relative winding sense of coils. The two transmit coils (the large coils to the sides) are wound in the same direction. The four receive coils (the four smaller coils surrounding the OP cell) are split into two pairs with one pair wound clockwise and the other wound counterclockwise.
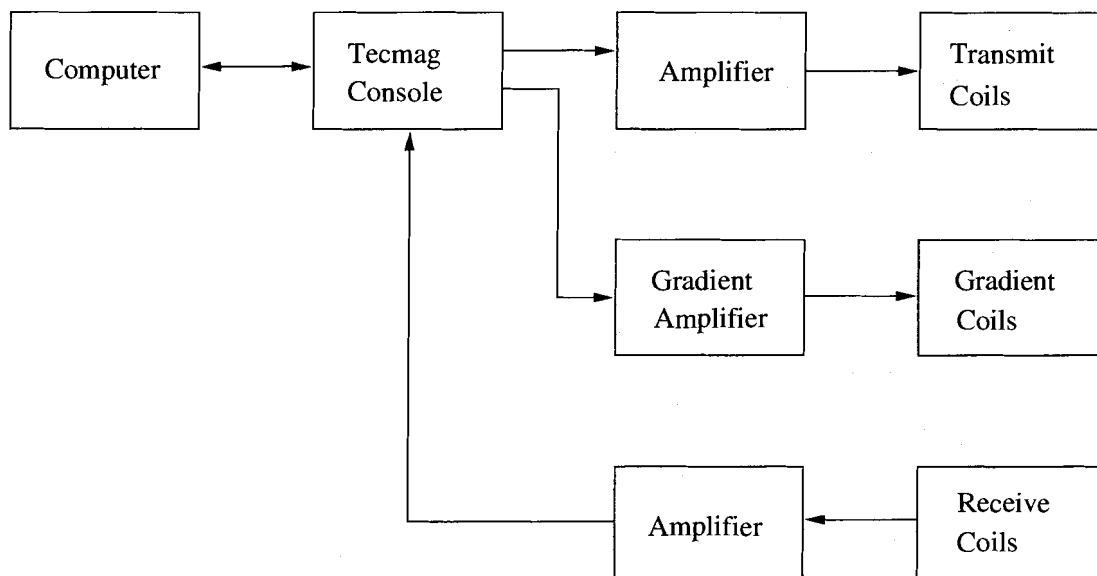
Figure 3.10: The electronics associated with the Tecmag Apollo LF spectrometer. The console was used for three separate purposes: driving the transmit coils, driving the gradient coils, and receiving the electronic signal generated by the receive coils.

When a $\mathbf{B}_1$ tipping pulse was required, an oscillating potential was created by the spectrometer. The spectrometer contains a frequency synthesizer and a transmitter modulator board that, in conjunction, create an oscillating potential. The frequency of the signal was always 20.4 kHz, matching the Larmor frequency of ^{3}He in the magnet. The peak-to-peak amplitude of the signal was approximately 0.6 V. This signal was then amplified by approximately 12 dB using an Amplifier Research Model 500A100AM3 amplifier. After the amplifier, the voltage signal was fed into the transmit coil through two noise gates. Fig. 3.11 shows a trace of the voltage signal for a sample $\mathbf{B}_1$ tipping pulse. The strength of the resultant $\boldsymbol{B}_1$ was typically of order 110 μT. Note that this signal is spectrally broad (a "soft" pulse). This minimizes variations in flip angles as the cell is moved from one location to another within the magnet.

Linear gradients were used in two ways: they were applied constantly at a low level to shim the magnetic field inside the magnet and they were momentarily ramped to higher levels to provide pulsed field gradients as part of a GRSE sequence. In both cases, they were controlled with the NTNMR software and the Tecmag spectrometer by varying the current
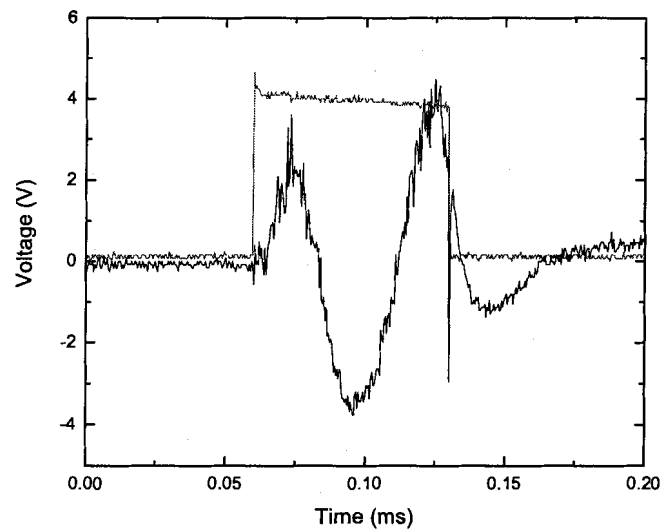
Figure 3.11: An example of a $\pi/2$ $\textbf{B}_1$ tipping pulse at 20.4 kHz as measured by the EMF applied across the transmit coil. The rectangular pulse represents the period of time over which the tipping pulse is applied. The ring down time of the tipping pulse comes about because of the finite Q of the tuned coils.
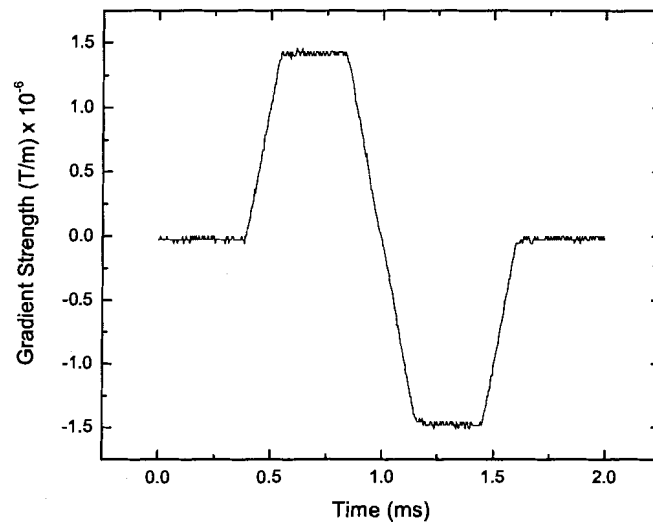
Figure 3.12: An example of a gradient pulse from a GRSE experiment. The field strength is inferred from a measurement of the voltage drop across a shunt resistance. The shape of the gradient pulse is discussed in Chapter 4.
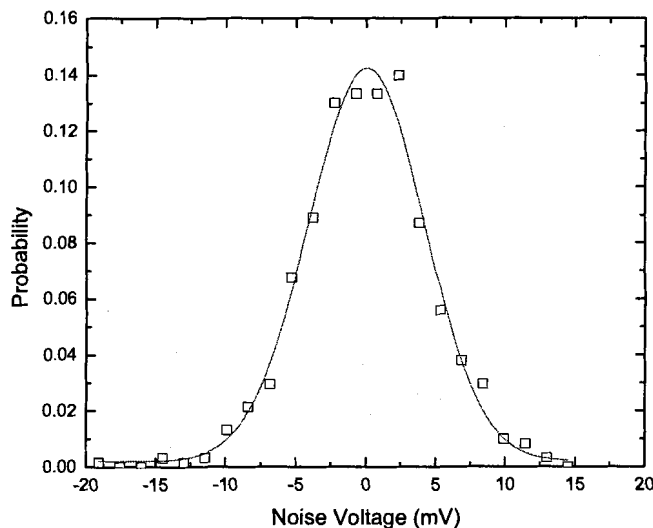
Figure 3.13: The distribution of amplitude noise on the nuclear precession signal induced in the receiver coils. The data has been fit with a Gaussian function.

fed to the gradient coils. The voltage signal used to control the gradients originated from the spectrometer and was converted to a current by a Techron 8607 Gradient Amplifier. The amplifier then drove the gradient coils. The shape of the gradient pulse was defined using the NTNMR software. An example of a typical gradient pulse used for a GRSE is shown in Fig. 3.12.

The amplitude of the nuclear precession signal induced in the receiver coils had a peak-to-peak amplitude of the voltage signal is of order 1 μV. A Stanford Research Systems SR560 Low-Noise Amplifier operating with a 20 kHz bandpass filter was used to amplify this signal by a factor of 10^4. The signal was passed into a digital receiver that amplified the signal by a factor of 2 and then was recorded with a fast 16-bit ADC converter. The recorded signal had a peak-to-peak amplitude of order 0.1 V. The amplitude noise present in the recorded signals was Gaussian distributed with a standard deviation of order 10 mV (see Fig. 3.13).

Chapter 4

Procedure

The effective diffusion coefficient of ^{3}He in a restricted geometry can be determined by measuring the amplitude of the free induction decay (FID) before and after the application of a bipolar gradient pulse [5]. The same type of experiment is apparently sensitive to the influence of concomitant gradients as demonstrated later in this thesis. This chapter outlines the procedure used to perform the attenuation measurements. First, there will be a discussion of the pulse sequence used to manipulate the nuclear spins. Then, the methods used to probe the influence of concomitant gradients on the outcome of this type of experiment will be discussed.

4.1 Attenuation Measurements

A series of experiments were performed where the amplitude of a FID was measured immediately before and after the application of a bipolar gradient pulse (see Fig. 4.1). The method used to extract amplitude information from signals is described in Chapter 5. From these measurements it is possible to calculate the attenuation incurred while the gradient field is applied. By performing a series of experiments where the gradient strength is incrementally changed, it is possible to determine the effective diffusion coefficient of the gas (see Subsection 2.3.7). The influence of concomitant gradients on the outcome of this type of measurement was investigated by repeating the experiment with the optical pumping (OP) cell placed at various positions within the magnet. The following subsections describe the pulse sequence and the procedures used for OP cell placement.
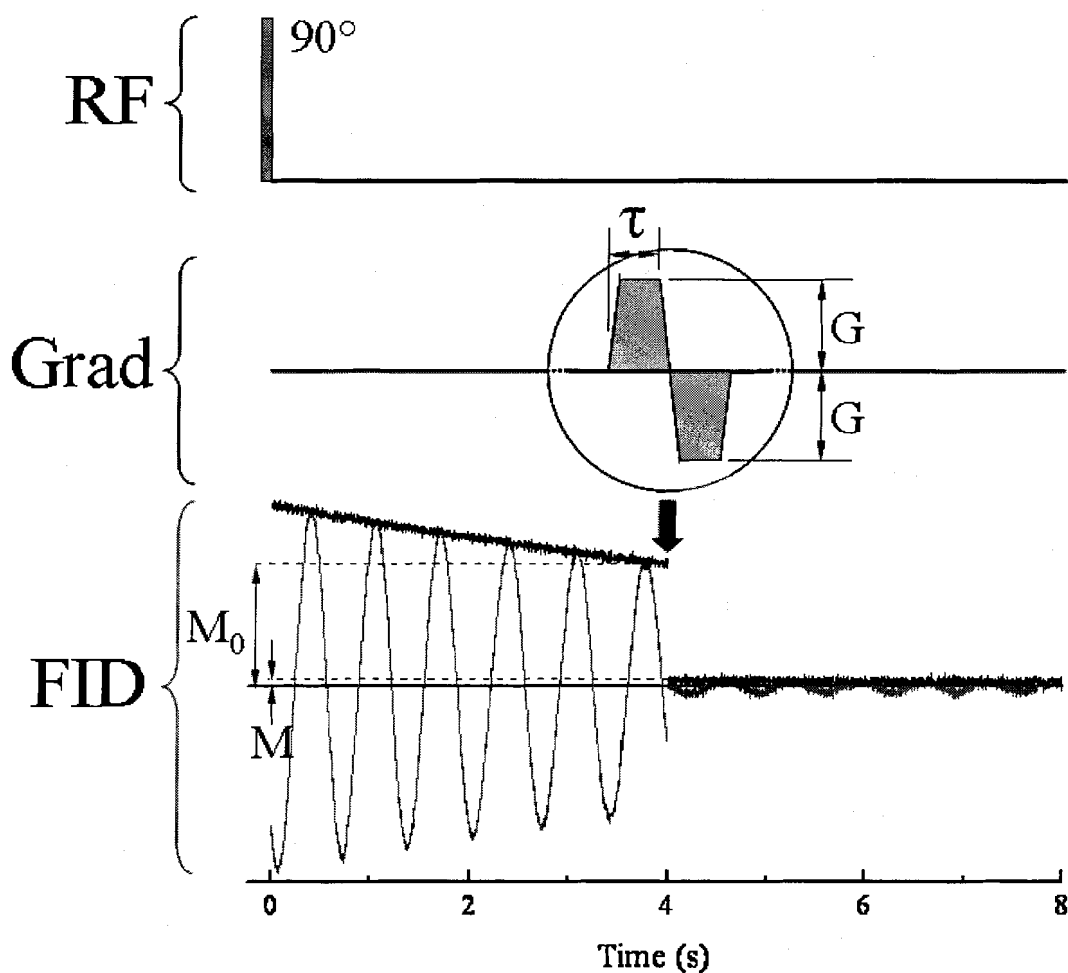
Figure 4.1: The shape of a FID during a typical attenuation measurement. The top part of this figure displays the application of a radio-frequency tipping pulse. The middle part of this figure displays the timing of the application of a bipolar gradient pulse. The bottom of the figure displays one phase of the complex detected signal and its magnitude. The other phase is not shown.

4.1.1 Pulse Sequence

Hyperpolarized ^{3}He nuclei were manipulated using a gradient-recalled echo sequence. A timing diagram for the pulse sequence used is shown in Fig. 4.2. First, a $\pi/2$ tipping pulse was applied at 20.4 kHz using the transmit coils. The duration of the tipping pulse was 70 μs. The $\pi/2$-pulse rotated the magnetization vector into the x-y plane (see Fig. 3.5 for the alignment of coordinates with respect to the orientation of the magnet). At some time, δ, after the $\pi/2$ pulse, a symmetric, bipolar field gradient directed along the x-axis of the magnet was applied. Typically, δ was of order 1 - 4 seconds. The time was chosen such that it was much shorter than the T_2^* decay time of the gas. This period of time was intended to eradicate spatial variations in the initial magnitude of the transverse magnetization.
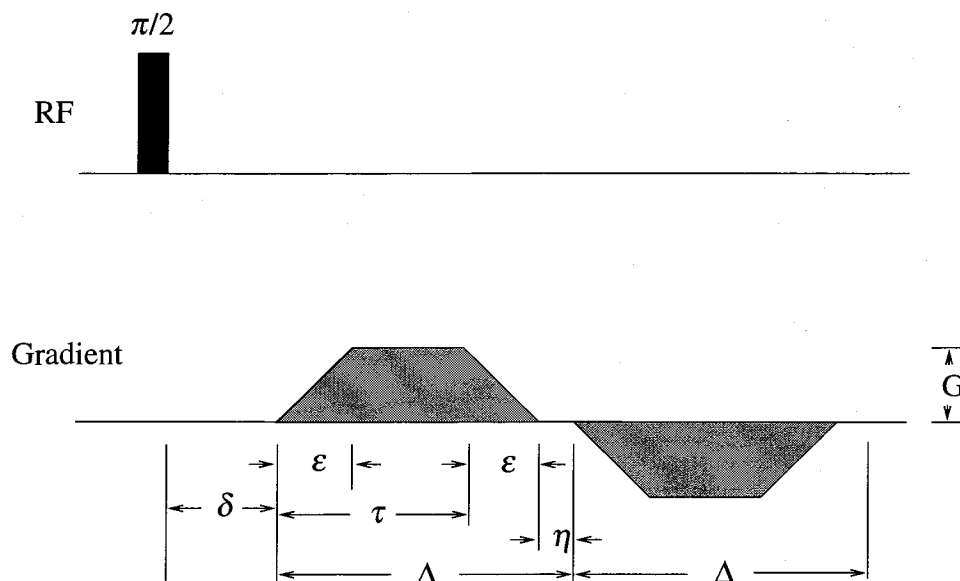
Figure 4.2: A schematic diagram (not to scale) of the pulse sequence used to probe the attenuation of a FID during the application of a field gradient.

The applied gradient pulses had a trapezoidal profile. The gradient strength was increased linearly over a period of time ε that was typically of order 150 μs. The plateau time $(\tau - \varepsilon)$ and interpulse delay time η were typically of order 300 μs, and 10 μs, respectively. The diffusion time is the time nuclei are free to diffuse during the application of the gradient. For rectangular gradients, the diffusion time is the simply the total duration of the gradient pulse. A correction is necessary for gradient pulses that are not rectangular. For

trapezoidal gradients the effective diffusion time is [41]

$$\tau_{eff} = \tau \left[1 + \frac{3(\varepsilon - \eta)}{2\tau} - \frac{\varepsilon^2}{4\tau^2} + \frac{\varepsilon^3}{20\tau^3} \right]^{\frac{1}{3}}, \qquad (4.1)$$

where the various symbols are defined in Fig. 4.2. Based on the timing values outlined above, the value for τ_{eff} for the gradient pulse described above is 515 μs.

4.1.2 The Role of Concomitant Gradients

As discussed in Chapter 2, the application of a bipolar gradient field attenuates a FID because of inexact rephasing. This attenuation is caused by both diffusion and by the influence of concomitant gradients. The main goal of this thesis is to investigate the conditions whereby concomitant gradient effects become important.

A recent experiment effectively using the same pulse sequence and apparatus has probed attenuation effects to achieve an accurate measure of the diffusion coefficient of ^{3}He [5]. Hayden et al. studied an OP cell filled with 1 Torr of ^{3}He placed at the isocentre of the magnet. The experiment involved measuring the attenuation of a FID when bipolar gradient pulses with various amplitudes and durations were applied. By fitting the measured data to Eq. 2.56, Hayden et al. determined the effective diffusion coefficient of 1 Torr confined to a cylindrical cell. Then, using Eq. 2.59, the diffusion coefficient of ^{3}He was calculated to be 0.140(6) m^2/s at 1 Torr and 293 K.

To explore the influence of concomitant gradients, three different experimental parameters were varied: gradient strength, OP cell position, and gas pressure. The first of these, gradient strength, influences the outcome of the experiment in two different ways. First, the diffusion induced attenuation of a FID is directly dependent on gradient strength. Second, the loss of coherence due to the influence of concomitant gradients is also directly dependent on gradient strength. Typically, at each OP cell position, fifty different attenuation measurements with different gradient strengths were made. For the 1 Torr cell, the gradient strength was incremented in equal steps between 0 and 2.2×10^{-3} T/m. For the 6 Torr cell, the gradient strength was incremented in equal steps between 0 and 5.0×10^{-3} T/m. The reason the maximum gradient strength was different for the two OP cells is discussed below.

The second experimental parameter that was varied was the OP cell placement. The same fifty experiments were repeated as the position of the OP cell along the z-axis of the magnet was changed. For the 1 Torr OP cell the cell was displaced within the range -10 cm to 10 cm from the magnet isocentre. For the 6 Torr OP cell this range was between -5 cm and 5 cm from the magnet isocentre. The axis of the cell was aligned to within 2.6° of that of the MRI magnet. The displacement of the geometric centre of the OP cell relative to the magnet isocentre was accurate to within 3.0 mm. As the displacement of the cell from the isocentre increases, the strength of the concomitant gradients grow (see Eq. 2.70) as does their influence on rephasing of spin coherences.

The final experimental parameter that was varied was the pressure of the ^{3}He gas in the cell. These experiments were carried out for OP cells with two different pressures: 1 Torr and 6 Torr at 293 K. As the pressure is increased (or as the diffusion coefficient is decreased) it takes a larger gradient strength to achieve the same level of attenuation because atoms do not diffuse as far during the gradient pulses. Thus, it is possible to investigate larger gradient strengths in the case of the 6 Torr cell simply because the rate at which attenuation from diffusion is incurred is decreased.

Based on the discussed experimental parameters, it is possible to calculate the characteristic length scales (see subsection 2.3.7) and determine the diffusion regime in which these experiments are performed. The characteristic diffusion length scale ℓ_D is 0.8 cm and 0.3 cm for the 1 Torr and 6 Torr OP cells, respectively. The structural length scale ℓ_s is approximately 2.4 cm, the radius of the 1 Torr and 6 Torr OP cells. The value of the dephasing length scale ℓ_G varied from 2.5 cm to 0.7 cm for the 1 Torr OP cell and from 1.0 cm to 0.3 cm for the 6 Torr OP cell. Figure 4.3 displays the parameter space explored by the 1 Torr and 6 Torr experiments in terms of the three characteristic length scales (see Fig. 2.8). This demonstrates that both experiments probed the free diffusion regime (at small gradient strengths) and the poorly understood region between the localization regime and the free diffusion regime (at high gradient strengths).
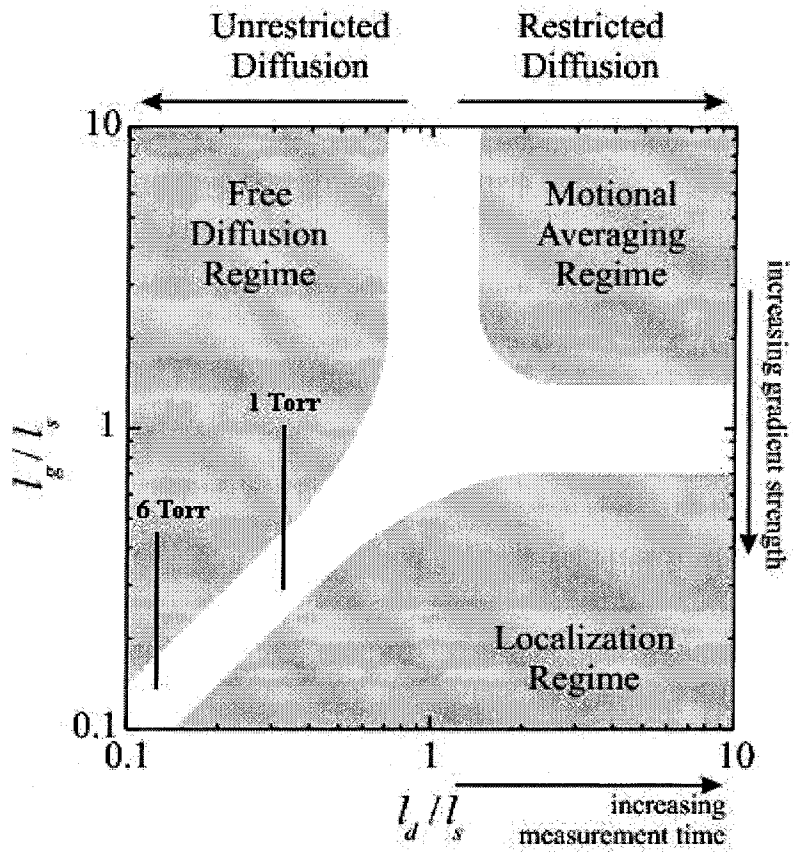
Figure 4.3: The diffusion regimes probed by the 1 Torr and 6 Torr experiments. The two solid lines represent the parameter space that is explored.

Chapter 5

Data Analysis

Analysis of the data acquired using the procedures outlined in the previous chapter requires accurate determination of the FID amplitude immediately before and after the application of the gradient pulse. As the gradient strength increases so does the attenuation. In order to maximize the dynamic range of the experiment, several different parameter estimation methods were characterized for reliability in regimes of low signal-to-noise ratio (SNR). Section 2.5 discusses how estimated parameters from the magnitude of a FID are influenced by a systematic bias at low SNR. This chapter presents the results of a study of the accuracy with which parameters such as FID amplitude and the FID decay time can be extracted from the recorded FID. In the first section, an analysis of simulated data is presented. Following this, an analysis of experimental data is presented.

5.1   Simulated Signal Analysis

An investigation of simulated FID data was performed to determine the conditions under which simultaneous analysis of both phases of a complex sinusoid yields accurate values for the amplitude and the decay time. Simulated FID signals were generated by adding random flucuations to both the amplitude and frequency of a complex damped sinusoid. These fluctuations were intended to model the amplitude noise and random walk frequency noise present in the real data. The first subsection below describes the method used to generate simulated data and the second subsection outlines the procedure used to test the accuracy of extracted parameters as a function of SNR. Simulated data were generated and

tested using a program written in the IGOR programming language. This program is listed in Appendix A.

5.1.1 Generation of Simulated Data

The ideal FID of the nuclear magnetization $M(t)$ can be represented as a complex damped sinusoid, as discussed in Section 2.3.3. That is

$$M(t) = M_0 e^{-t/T_2^*} e^{i\omega t} , \qquad (5.1)$$

where M_0 is the amplitude at $t = 0$, ω is the difference between the Larmor frequency and the local oscillator, and T_2^* is the decay time. In order to accurately simulate a FID as it would be recorded, the various noise sources discussed in Section 2.5.1 have to be included in the simulation. The amplitude noise, caused by Johnson noise, amplification noise and noise induced in the receiver coils by background magnetic fluctuations, has a Gaussian distribution (see Fig. 3.13). This can be simulated by adding a random amplitude noise term, $\Delta M(t)$, to M_0. Random walk frequency noise, caused by random fluctuations in the magnetic field, also has a Gaussian distribution and can be simulated by adding a random frequency noise term, $\Delta \omega(t)$, to ω. The third type of noise present in the datasets, frequency drift noise, was not included in the simulation. Thus, the simulated data represents a FID signal over a period of time during which the frequency drift is negligible. The simulated data has the form

$$M(t) = \left[M_0 e^{-t/T_2^*} + \Delta M(t) \right] e^{i[(\omega + \Delta \omega(t))t + \phi]} . \qquad (5.2)$$

The following discussion will refer to the amplitude SNR and the standard deviation of fractional frequency fluctuations. The amplitude SNR is defined as the ratio of the seed value of M_0 to the standard deviation of the applied random variable $\Delta M(t)$. The frequency stability is characterized in terms of a standard deviation σ for the distribution of instantaneous fractional frequency fluctuations $\Delta \omega(t)/\omega_0$, where ω_0 is the Larmor frequency. This quantity does not always converge to a meaningful limit for all noise types, as is the case for the frequency drift problem discussed in the next section. In general, the Allan variance [61] provides a much more robust measure of frequency stability. In experimental data, the amplitude SNR ranged from 50 to 1 and σ ranged from 0.075 to 10 ppm. Figure 5.1 shows

(a) Amplitude Noise   (b) Random-walk Frequency Noise
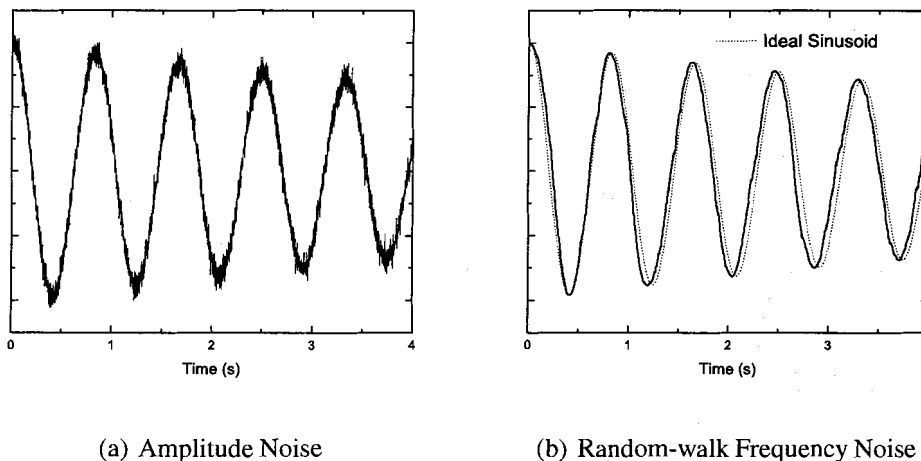
Figure 5.1: Two examples of simulated FID. Figure 5.1(a) displays a simulated FID with an amplitude SNR of 20. Figure 5.1(b) shows a simulated FID with a distribution of fractional frequency fluctuations characterized by $\sigma = 10$ ppm.

two simulated signals: one with random amplitude noise and one with random frequency noise.

5.1.2 Analysis of Simulated Data

Five different models were tested by fitting them to simulated FIDs using a least squares minimization routine. Models (i) and (iii) involve exponential curves that are fit to the absolute square of the FID and the magnitude of the FID, respectively. Both of these models are commonly used to analyze NMR data. Models (ii) and (iv) also involve exponential curves that are fit to the square of the FID and the magnitude of the FID, respectively but also attempt to correct for systematic bias by allowing for a constant offset at long times. Finally, model (v) involves a simultaneous fit to both phases of the simulated FID data. Note that the models (i)-(iv) are not as computationally intense as model (v). The purpose of these tests was to determine which model produced the most accurate measurements of M_0 and T_2^* of the simulated FID over a large range of SNR and fractional frequency fluctuations.

The five models that were tested have the form

$$(i) \qquad \left(M_1^{Fit}(t)\right)^2 \;=\; A^2 e^{-2t/T} \tag{5.3}$$

$$(ii) \qquad \left(M_2^{Fit}(t)\right)^2 \;=\; A^2 e^{-2t/T} - \eta^2 \tag{5.4}$$

$$(iii) \qquad M_3^{Fit}(t) \;=\; A e^{-t/T} \tag{5.5}$$

$$(iv) \qquad M_4^{Fit}(t) \;=\; A e^{-t/T} - \eta \tag{5.6}$$

$$(v) \qquad M_5^{Fit}(t) \;=\; A\left[\cos\left(\omega t + \theta\right) + i\sin\left(\omega t + \theta\right)\right] e^{-t/T} , \tag{5.7}$$

where A is an amplitude parameter, T is a decay constant parameter, ω is a frequency parameter, θ is a phase parameter and η is the mean value of the magnitude of the amplitude noise. Models (i)-(iii) and (v) all have a physical motivation. Model (iv) is not based on a proper physical argument. The models were used in the following way: a simulated FID was created, the model was applied to the simulated FID and the parameters were recorded. The parameters of most interest are A, the measure of the FID amplitude, and T, the measure of the FID decay time.

Figure 5.2 and Fig. 5.3 show the results of fitting each model to simulated FIDs with different values of amplitude SNR and σ. Each point in the figures results from the analysis of 1000 different simulated signals. Each of the 1000 simulated signals were generated with the same level of amplitude SNR and σ but with different (randomly generated) noise.

The amplitude SNR tests reveal that the physically motivated models return amplitude and decay time parameters that are within 5% of the seed values for SNRs of 5 and higher. Once the amplitude SNR drops below 5, models (i)-(iii) return parameters that are significantly different from the seed values. This is a direct result of the Rician bias that is discussed in Section 2.5. Of particular interest is the fact that even though the fit parameters for the amplitude and decay rate become less accurate, their precision remains high. This could easily lead to the misinterpretation of data. Model (v) is not affected by the Rician bias and returns values within 5% for both the amplitude and decay time over the range of SNR that was explored (0.5-100).

A study of the influence of random frequency noise was only performed on model (v), since it is the only one that depends on frequency. The results of this modeling experiment show that the amplitude and decay time parameters extracted from simulated FIDs are within 5% of the seed values for values of σ greater than 50 ppm. Above this value the fit parameters are always smaller than the seed value and return parameters as low as 20%

(a) Amplitude   (b) Decay Time
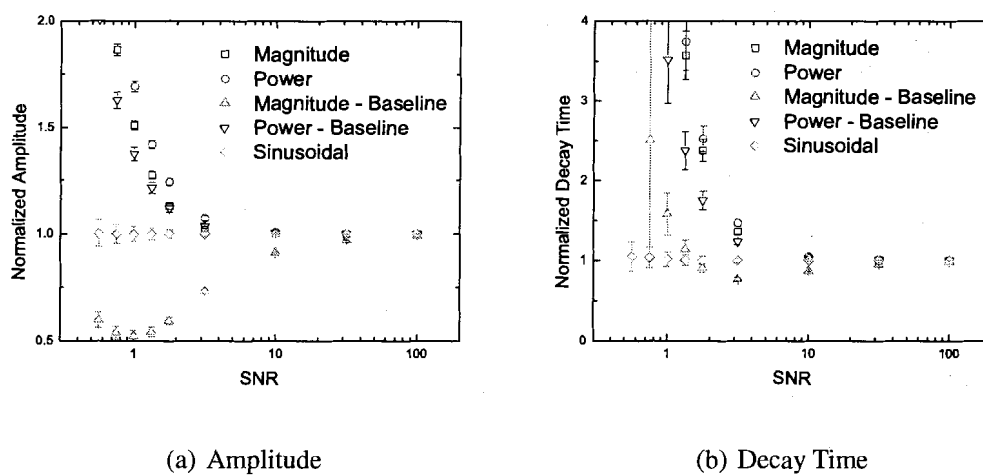
Figure 5.2: A comparison of five different analytic models for extracting the amplitude and decay time from simulated FIDs with amplitude SNR. Figure 5.2(a) shows results for amplitudes and Fig. 5.2(b) shows results for decay times. In both cases, the results have been normalized to the seed values that were used to generate the simulated FID. The error bars represent the standard deviation of the distribution of extracted parameters. The term power refers to model (i) and the term power minus baseline refers to model (ii)

(a) Amplitude   (b) Decay Rate
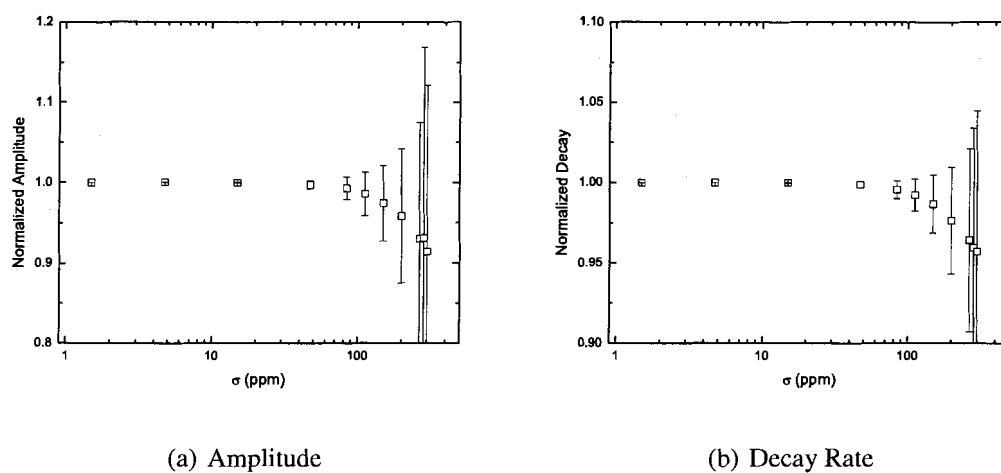
Figure 5.3: A study of the influence of frequency noise on the reliability of parameters extracted from a simultaneous fit to both phases of noisy simulated FID data. Figure 5.3(a) shows results for amplitude values and Fig. 5.3(b) shows results for decay times. In both cases, the results have been normalized to the seed values that were used to generate the simulated FID. The error bars represent the standard deviation of the distribution of extracted parameters. For all measurements, model (v) was fit to the full dataset.

below the seed values. This decrease in parameter value occurs because the simulated FID begins to look less like a sinusoid as σ increases. As the FID distorts, any model sinusoid with a rigidly fixed frequency applied to it will be both in and out of phase. When this is the case, it is impossible for model (v) to converge to reasonable parameter values.

These studies show that, in regimes of high amplitude SNR and fractional frequency fluctuation, all of the applied models return precise and accurate estimations for the amplitude and decay time of simulated FIDs. In regimes of amplitude SNR lower than 10 and σ lower than 50 ppm, model (v) returns the most accurate values of extracted amplitude and decay time. Above a σ of 50 ppm the parameters extracted from model (v) become less accurate and less precise. Above a σ of 300, the model is not able to converge to reasonable parameter values. The experimental data presented in Chapter 6 are characterized by a σ less than 15 ppm. It is important to remember that these constraints for model (v) are only valid in regimes where there is no frequency drift noise. This is not always the case under experimental conditions.

5.2 Experimental Data Analysis

The data from each experiment can be broken into two different regions: before the bipolar gradient pulse and after the bipolar gradient pulse. The amplitude of the FID immediately after the gradient pulse depends on the strength and duration of the gradient pulse. As the gradient strength is increased the amplitude of the FID after the gradient pulse decreases and eventually becomes comparable to the baseline noise level. Although the amplitude of the FID decreases, the level of amplitude noise remains the same. Therefore, it is important to be able to accurately measure the amplitude and decay constant of the FID in regimes of low SNR. The analysis given in the previous section shows that as long as there is no frequency drift the most accurate and precise amplitudes and decay times are obtained by simultaneously fitting to the phases of the complex signal. The influence of frequency drift in real experimental data is discussed below.
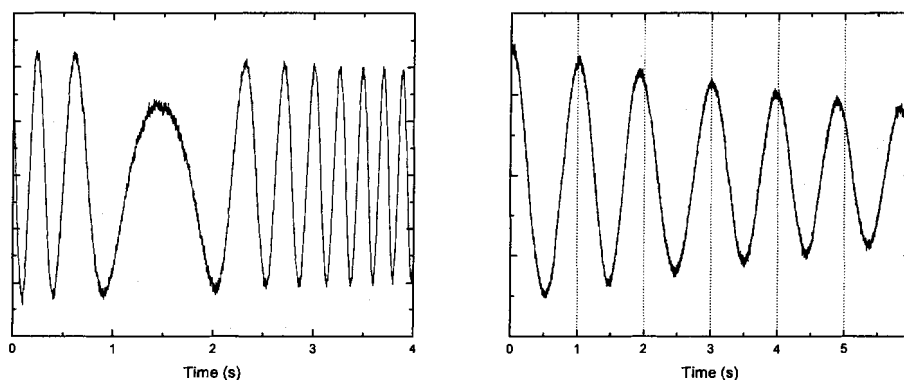
(a) The influence of a nearby elevator   (b) The influence of current source drift

Figure 5.4: The influence of elevator movement and current source drift on recorded FIDs. Figure 5.4(a) shows a FID recorded as an elevator adjacent to the experiment was in motion. Figure 5.4(b) shows a FID recorded when the elevator was stationary. Drift in the current source driving the solenoid causes a subtle frequency shift. Lines drawn at one second intervals reveal this effect. There is a net drift of 0.1 Hz over the 6 second window.

5.2.1 Frequency Drift Noise

Real FIDs, such as those acquired as part of the concomitant gradient study, exhibit frequency drift noise, which is related to changes in the magnetic field. Two systematic sources of magnetic field drift have been identified: the presence of a nearby elevator and the current source that drives the solenoid. Figure 5.4 illustrates the influence of these two noise sources on recorded FIDs.

The experiment was performed in a room adjacent to an elevator shaft. As the elevator changes floors, the local magnetic field at the OP cell location changes in a systematic way. Figure 5.4(a) shows a FID that was recorded at the same time as the elevator was in motion. The Larmor frequency of the ^{3}He systematically changes by 15 Hz over a 4 second period. This corresponds to a change in the local magnetic field of 0.5 μT. It is impossible to fit a complex sinusoid with a constant frequency to this type of data. Data exhibiting this type of behaviour were discarded and the experiment was repeated.

Figure 5.4(b) shows a FID in which the systematic change in Larmor frequency is more

subtle. The field drift is related to the stability of the current driving the solenoid (see Fig. 3.6). The frequency drift observed in data was typically of order 0.3 Hz over an 8 second period. This corresponds to a change in the local magnetic field of order 10 nT. Alternately, this corresponds to a change in current from the power supply or order 0.1 mA. This is consistent with the specifications for a Hewlett-Packard 6002A DC Power Supply. Although this drift is small compared to the drift caused by the elevator, a complex sinusoid with a constant frequency cannot be fit to the data. Again, this problem is caused by the FID distorting. As previously mentioned, any model sinusoid applied to these data will be both in phase and out of phase with the FID at different times during the decay, and thus model (v) is not able to converge.

5.2.2 Signal Windowing

The method that was used to overcome the problem of frequency drift in recorded FIDs was to separate the FID into "windows". The goal was to create shorter datasets over which the frequency drift was small enough that the complex sinusoid model could be used. For each window, the model was fit to data and an amplitude and decay time were extracted. The averages of these values were then assigned to the entire signal.

Figure 5.5 shows an example of a FID and the measured of M/M_0 that was extracted when using several different window lengths. For window lengths greater than 1 s, the ratio is clearly incorrect. This occurs because all of the fits return values for M_0 and M that are much smaller than the actual amount. This occurs when the FID is too distorted to apply model (v). For window lengths of 1 s or less, the complex sinusoid model extracted correct rates. Under these conditions the total accumulated phase due to frequency drift noise was negligible. The frequency drift noise was considered to be negligible when it was of the same order as random frequency noise with a σ of 10 ppm (the same level as the worst random frequency noise of the measured data). The typical value of window length used in the analysis of data presented later in this thesis was 1 s. This corresponds to a frequency drift of order 0.03 Hz (or a magnetic field drift of 1 nT) over the length of the window. This technique can only be used when the windows contain at least one period of the FIDs in order to accurately fit to the frequency and phase. Therefore, it is suggested that the local oscillator should be offset from the Larmor frequency enough to avoid zero beat conditions.
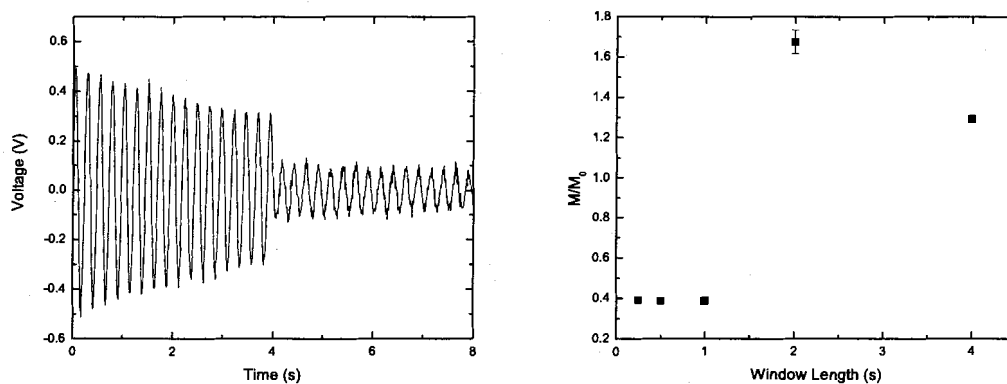
(a) A sample FID.

(b) Analysis of M/M_0 with various window lengths.

Figure 5.5: The effect of window length on the extracted value of M/M_0. Figure 5.5(a) shows a FID acquired from the 6 Torr ^{3}He sample placed at the gradient isocentre. Figure 5.5(b) shows the ratio of the FID amplitude before and after the gradient pulse (which occured at 4 s) as extracted using 5 different window lengths. The error bars assigned to each point represents the standard deviation of the ratio values extracted from each window.

Chapter 6

Results and Discussion

This chapter describes the results of several GRSE experiments performed using the 1 Torr and 6 Torr OP cells. The first section focuses on the 1 Torr cell and, specifically, compares data acquired at the isocentre of the magnet with previous work [5]. The next section focuses on the the 6 Torr cell. The third section is devoted to an interpretation of these data. In particular the equations introduced in subsection 2.4.2 for the influence of concomitant gradients are applied to the experimental geometry. Similarities (and differences) between this model and experimental data are discussed. This is followed by a description of an experiment in which an asymmetric bipolar gradient was employed to further probe the role of concomitant gradients. This chapter concludes with a critical analysis of these GRSE experiments.

As an aside, the isocentre of the gradient fields and the centre of the solenoid differ by 0.6 cm. The positions of the OP cell reported in the following discussions are reported with respect to the isocentre of the applied gradients.

6.1   1-Torr Cell Results

A series of GRSE experiments was performed using the 1 Torr OP cell. A similar series of experiments was used by Hayden et al. to determine the diffusion coefficient of ^{3}He at 1 Torr and 293 K [5]. In that experiment the cell was placed at the isocentre of the MRI magnet. The following subsections illustrate the result of repeating these measurements as the cell is displaced along the z-axis of the MRI magnet. As well, these experimental

results are compared with those of Hayden et al.

6.1.1 Isocentre

Figure 6.1 shows FID attenuation data for a series of GRSE sequences as a function of gradient amplitude when the 1 Torr OP cell is placed 1.3 cm from the isocentre of the magnet. The error bars increase in size as the signal attenuation increases because the amplitude SNR decreases.

The data is plotted using a semi-logarithmic scale because Eq. 2.56 predicts that the diffusion induced attenuation should fall along a straight line with a slope of $-\frac{2}{3}D_{eff}\gamma^2\tau^2$ when plotted in this format. In the experiments performed by Hayden et al., the self diffusion coefficient D_0 of ^3He was determined to be 0.140(6) m^2/s. This was accomplished by repeating measurements similar to those shown in Fig. 6.1 for different effective diffusion times τ and then fitting the data to Eq. 2.56. Using the previously determined value of D_0, Eq. 2.59 can be used to calculate the effective diffusion D_{eff} expected for the present experimental conditions. The effective diffusion time and the radius of the OP cell used to calculate D_{eff} were 515 μs and 2.2 cm, respectively. The result is 0.091(5) m^2/s. The solid line shown in Fig. 6.1 was calculated using this value of D_{eff} in Eq. 2.56 and represents the expected attenuation caused by diffusion. The solid line demonstrates agreement with previous work. A more important conclusion that will become obvious later is that diffusion is the only source of attenuation responsible for this behaviour. This experiment provides a baseline with which to compare the results presented below.

6.1.2 Axial Offset

Figure 6.2 shows the result of repeating the experiment described above as a function of position along the MRI magnet axis. Data for two displacements from the isocentre of the magnet are shown: 6.3 cm and 11.3 cm. In both cases there is a clear departure from the linear behaviour predicted by Eq. 2.56 when the applied field gradient increases beyond 1×10^{-3} T/m. There must be another mechanism causing the additional attenuation. This mechanism depends on gradient strength and cell position. One explanation is that the additional attenuation is caused by concomitant gradients. This hypothesis is explored further in Section 6.3.

Figure 6.1: FID attenuation for the 1 Torr cell displaced 1.3 cm from the isocentre of the magnet along the z-axis as measured using a GRSE sequence. The solid line represents the attenuation expected for a gas with an effective diffusion coefficient of 0.091 m^2/s.

Figure 6.2: FID attenuation for the 1 Torr cell placed at three different positions along the z-axis of the magnet as measured using a GRSE sequence. The solid line represents the attenuation expected for a gas with an effective diffusion coefficient of 0.091 m^2/s. Displacements are measured with respect to the magnet isocentre.
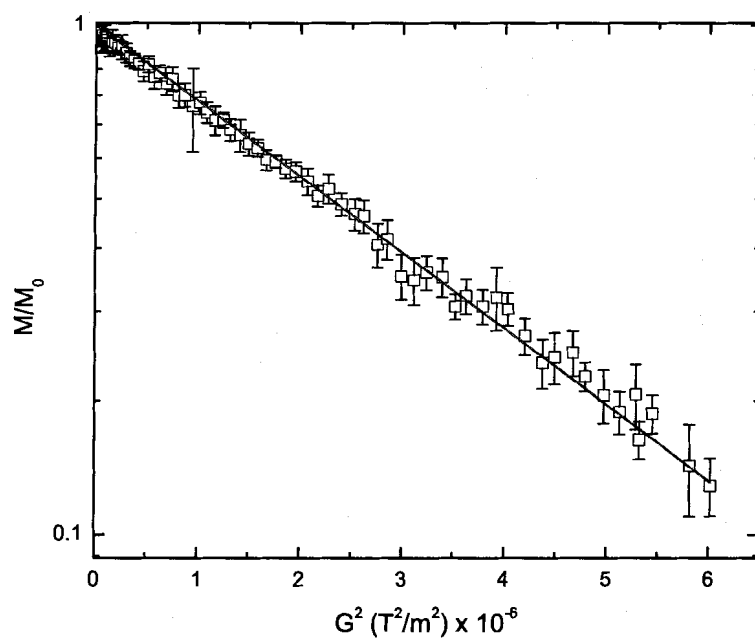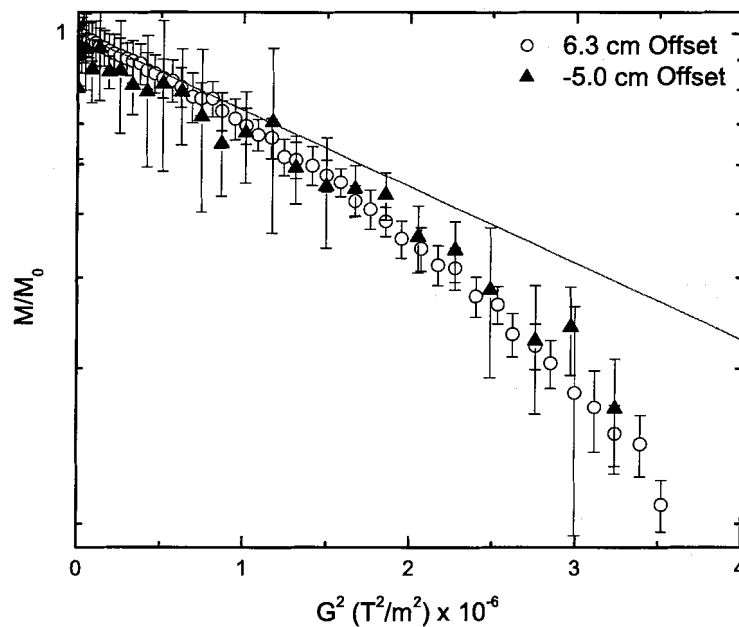
Figure 6.3: FID attenuation for the 1 Torr cell placed on opposite sides of the isocentre of the magnet along the z-axis as measured using a GRSE sequence. The solid line represents the attenuation expected for a gas with an effective diffusion coefficient of 0.091 m^2/s.

Figure 6.3 shows the results of an additional experiment on a cell displacement of -5.0 cm from the isocentre of the magnet. The measured attenuation demonstrates agreement with the measurements made at a cell displacement of 6.3 cm. This suggests that the mechanism causing the additional attenuation is symmetric with respect to $\pm z$ displacements.

6.2 6-Torr Results

The same experiments that were performed on the 1-Torr OP cell were also performed on the 6 Torr OP cell. Increasing the density of the gas decreases the effect of diffusion and enables larger gradient strengths to be applied. This in turn accentuates the relative impor-

tance of concomitant gradients. The following subsections describe these measurements.

6.2.1 Isocentre

Figure 6.4 shows FID attenuation data for a series of GRSE sequences as a function of gradient amplitude when the 6 Torr OP cell is placed at 0.6 cm from the isocentre of the magnet. For an ideal gas, the diffusion coefficient is inversely proportional to the pressure of the gas. Thus one expects D_0 for ^{3}He gas at a pressure of 6 Torr to be 0.023(1) m^2/s at room temperature. This in turn implies $D_{eff} = 0.020(1)$ m^2/s for the conditions of the experiments summarized in Fig. 6.4. The solid line shown in Fig. 6.4 represents the expected attenuation based on this effective diffusion coefficient. Over the range of gradient strengths probed by the 1 Torr cell placed at 1.3 cm from the isocentre of the magnet, the measured attenuation displays a linear behaviour. However, there is a clear departure from the linear behaviour predicted by Eq. 2.56 when the applied field gradient increases beyond 2.2×10^{-3} T/m. The effect of increasing the pressure is that the distance atoms move during the gradient pulse is decreased. It is thus possible to probe larger gradient strengths as there is less attenuation caused by diffusion. These results show that even near the isocentre of the magnet, the mechanism causing additional attenuation becomes non-negligible at larger gradient strengths. As an aside, the uncertainties for the 6-Torr data are much smaller than those for the 1 Torr data because the six-fold increase in the number of atoms in the 6 Torr cell that results in a larger NMR signal.

6.2.2 Axial Offset

Figure 6.5 summarizes data acquired as the 6 Torr cell was displaced 1.3 cm, 3.8 cm and 6.4 cm from the isocentre of the magnet along the z-axis. It is apparent that mechanisms other than diffusion influence the FID attenuation. These mechanisms depend on gradient strength and cell position. One of the most interesting characteristics of these data is that the attenuation is not a monotonic function of gradient strength. Specifically, the data the 3.0 cm and 5.7 cm offsets both display local extrema. The remainder of this chapter is devoted to an interpretation of these data.
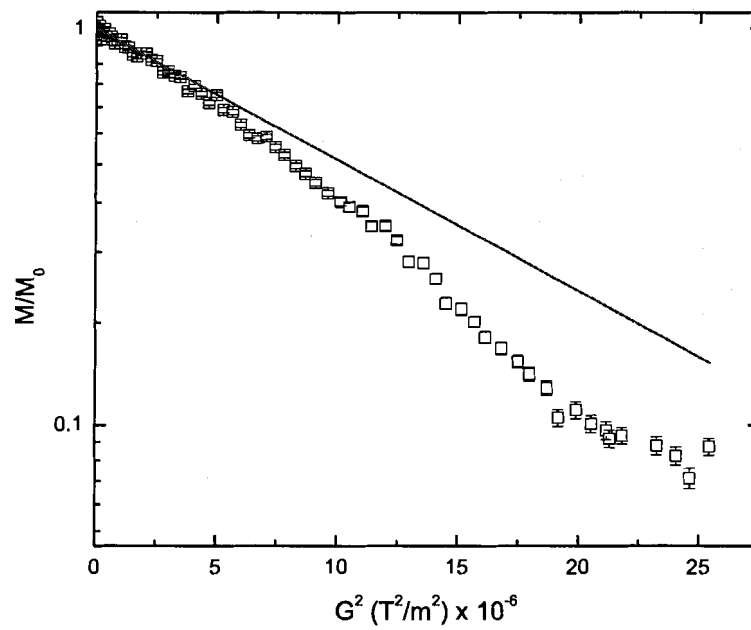
Figure 6.4: FID attenuation for the 6 Torr cell placed 0.6 cm from the isocentre of the magnet as measured using a GRSE sequence. The solid line represents the attenuation expected for a gas with an effective diffusion coefficient of 0.020 m^2/s.
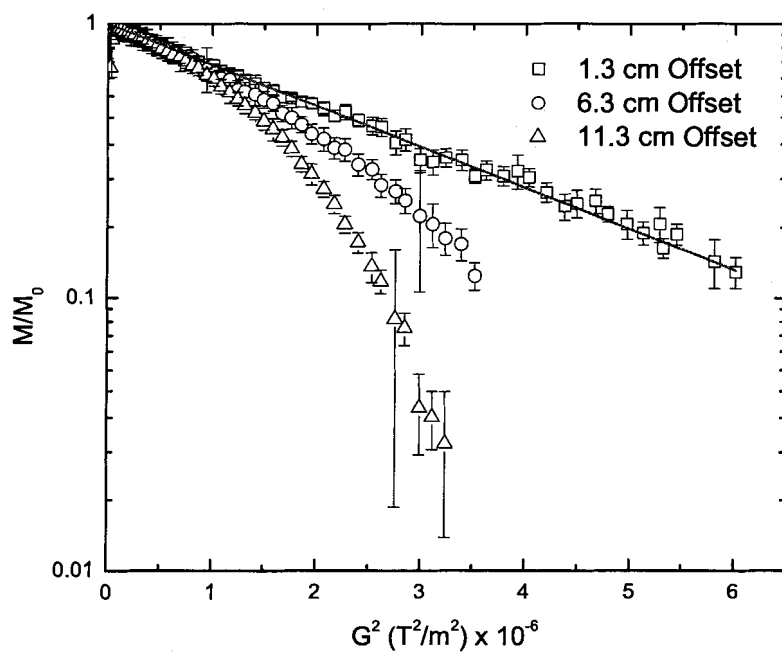
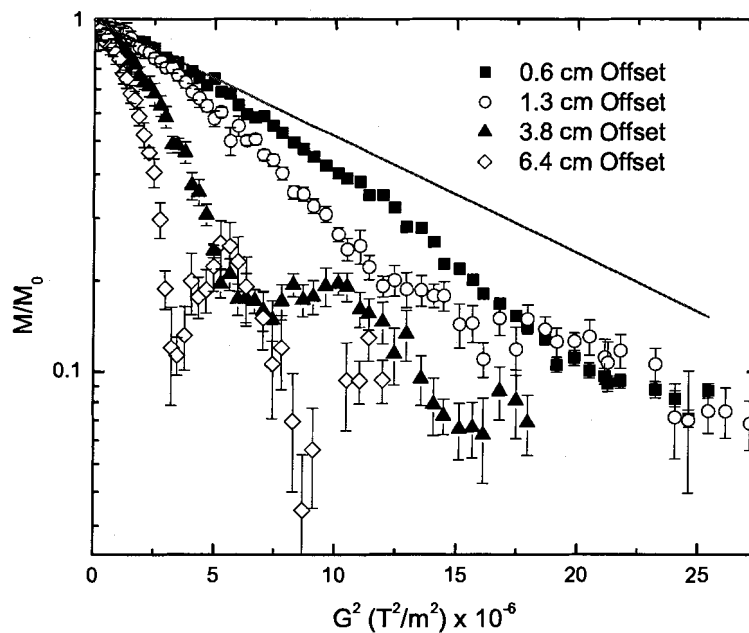Figure 6.5: FID attenuation for the 1 Torr cell placed at four different positions with respect to the magnet isocentre as measured using a GRSE sequence. The positions used were the 0.6 cm, 1.3 cm, 3.8 cm, and 6.4 cm displaced from the isocentre of the magnet in the positive z direction. The solid line represents the expected attenuation for a gas with an effective diffusion coefficient of 0.020 m^2/s.

6.3 Interpretation

Section 2.4.2 discussed the anticipated influence of concomitant gradients on the attenuation of FIDs. The equations presented in that section are used below to calculate the attenuation expected for the specific gradient pulses and geometry of the experiments described above.

6.3.1 Concomitant Gradient Model for a Cylindrical Cell

As discussed in Subsection 2.4.2, the phase accumulated by an atom during the application of a gradient pulse is given by

$$\phi\,(y,z) = \int_0^t dt\,\gamma|\boldsymbol{B}|\,, \tag{6.1}$$

where t is the total duration of the pulse and $\boldsymbol{B}$ is the magnetic field (i.e. the superposition of the static magnetic field $\boldsymbol{B}_0$ and the applied field gradient). The gradient pulse has a trapezoidal profile (as outlined in Section 4.1.1). The accumulated phase over the entire gradient pulse can be calculated by dividing the pulse into six different sections: a linear increase from 0 T/m to G, a plateau of amplitude G, a linear decrease from G to 0 T/m, a linear decrease from 0 T/m to $-G$, a plateau of amplitude $-G$ and a linear increase from $-G$ to 0 T/m. For the following discussion, the gradient pulse is assumed to begin at time $t = 0$. The other symbols representing specific times during the gradient pulse are all defined in Fig. 4.2.

During the periods of time when the gradient pulse is constant, the magnitude of the magnetic field is

$$B^+ = \sqrt{(B_0 + Gy)^2 + G^2 z^2} \tag{6.2}$$

$$B^- = \sqrt{(B_0 - Gy)^2 + G^2 z^2}\,, \tag{6.3}$$

where B^+ is the magnetic field during the positive plateau, B^- is the magnetic field during the negative plateau, B_0 is the static magnetic field strength and y and z are the coordinates of the point under consideration. The magnitude of the magnetic fields during the gradient ramp up and down periods are

$$B_1^{up}(t) = \sqrt{\left(B_0 + Gy\left(\frac{t}{\varepsilon}\right)\right)^2 + G^2 z^2 \left(\frac{t}{\varepsilon}\right)^2} \tag{6.4}$$

$$B_1^{down}(t) = \sqrt{\left(B_0 + Gy\left(1 - \frac{t - \tau}{\varepsilon}\right)\right)^2 + G^2 z^2 \left(1 - \frac{t - \tau}{\varepsilon}\right)^2} \tag{6.5}$$

$$B_2^{down}(t)) = \sqrt{\left(B_0 - Gy\left(\frac{t - \Delta}{\varepsilon}\right)\right)^2 + G^2 z^2 \left(\frac{t - \Delta}{\varepsilon}\right)^2} \tag{6.6}$$

$$B_2^{up}(t) = \sqrt{\left(B_0 - Gy\left(1 - \frac{t - (\Delta + \tau)}{\varepsilon}\right)\right)^2 + G^2 z^2 \left(1 - \frac{t - (\Delta + \tau)}{\varepsilon}\right)^2}, \tag{6.7}$$

Taking each section into consideration, Eq. 6.1 becomes

$$\begin{aligned}
\phi(y, z, G) &= \gamma\tau(B^+ + B^-) + \int_0^\varepsilon dt\, \gamma B_1^{up}(t) + \int_\tau^{\tau + \varepsilon} dt\, \gamma B_1^{down}(t) \\
&+ \int_\Delta^{\Delta + \varepsilon} dt\, \gamma B_2^{down}(t) + \int_{\Delta + \tau}^{\Delta + \tau + \varepsilon} dt\, \gamma B_2^{up}(t).
\end{aligned} \tag{6.8}$$

The first term in this equation takes into account the phase accumulated during the periods of time when the gradient strength remains constant. The four integrals give the phase accumulated over the four intervals during which the gradient is being ramped up or ramped down.

The net transverse magnetization in the cell after a gradient pulse is

$$M \propto \int_V e^{-i\phi(y,z,G)} dV, \tag{6.9}$$

where $\phi(y, z, G)$ is given by Eq. 6.8. For a cylinder with radius a and length ℓ centred on the position z_c, this becomes

$$M_{tot}^{cyl}(G) \propto \int_{-a}^{a} dy \sqrt{a^2 - y^2} \int_{z_c - \ell/2}^{z_c + \ell/2} dz\, e^{-i\phi(y,z,G)}. \tag{6.10}$$

The attenuation of the FID amplitude can then be determined by calculating the ratio

$$\frac{M_{tot}^{cyl}(G)}{M_{tot}^{cyl}(0)}. \tag{6.11}$$

Calculations of this ratio were performed using Mathematica. The relevant code is given in Appendix B. Each integral was evaluated numerically as a summation over a sufficiently fine mesh.

6.3.2 Comparison with Data

A model concomitant gradient attenuation curve was calculated for each experiment. Comparisons between these model calculations and the data from the two cells are shown in Figs 6.6 and 6.7. Also shown is the expected attenuation resulting from diffusion. Qualitatively, the model calculations suggest the correct behaviour, but quantitatively they do not fit any of the data sets well. This is to be expected since the model calculations assume that the ^{3}He atoms are static when in fact it is known that they move during the experiment. A proper accounting of the attenuation must take into account both effects. This observation is consistent with the fact that the agreement between the model calculations and the data is best for large offsets (where concomitant gradient effects are exaggerated) and at high gas densities (where diffusion is slow).

Figure 6.6(a) shows the data and model calculations for the the 1-Torr OP cell placed 1.3 cm from the isocentre of the magnet. The data agree with previous experiments [5] and can be fully explained by the diffusion of ^{3}He atoms during the gradient pulses. This is consistent with the model calculation for concomitant gradient effects which predicts very little additional attenuation.

Figures 6.6(b) and 6.6(c) show the data and model calculations for the 1-Torr OP cell displaced 6.3 cm and 11.3 cm from the isocentre of the magnet. Both data sets deviate from the behaviour expected for diffusion in a uniform gradient when the gradient strength is increased above 0.001 T/m. This value corresponds to a radius of curvature R_c of 60 cm. As the cell is moved away from the isocentre of the magnet, the influence of concomitant gradients increases because the value of G_z increases. The model calculations predict an effect that is comparable to that of diffusion. They also predict the existence of local minima and maxima. These comparisons suggest that concomitant gradients influence the attenuation of FIDs. At the same time it is difficult to rule out other effects since the maximum gradient strength that is probed is not large enough to reveal the characteristic extrema expected for concomitant gradients.
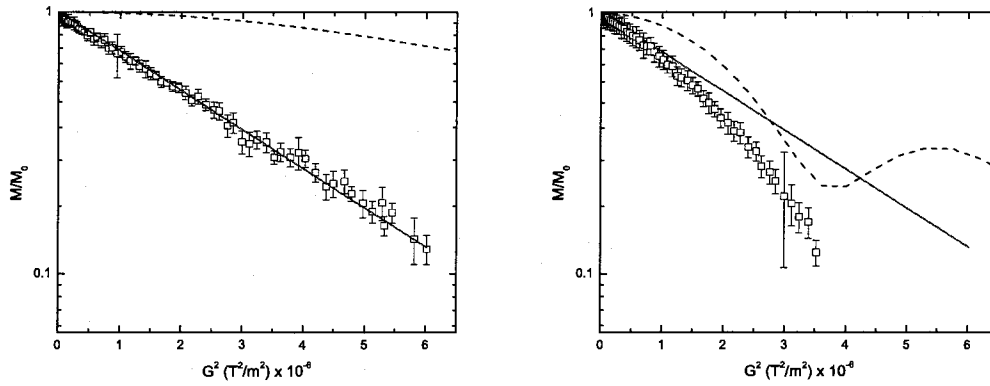
(a) 1.3 cm Offset

(b) 6.3 cm Offset
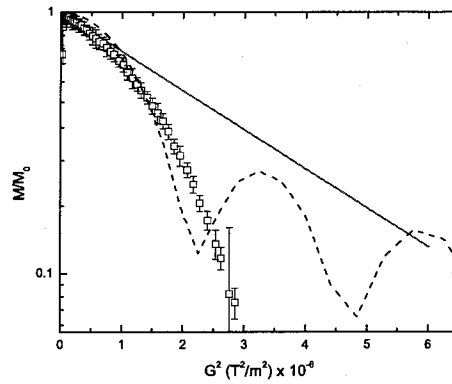
(c) 11.3 cm Offset

Figure 6.6: Comparison of data (points) with model calculations (dashed line) for each of the experiments performed with the 1 Torr cell. The solid line represents the expected attenuation for a gas with an effective diffusion coefficient of 0.091 m^2/s.

(a) 0.6 cm Offset

(b) 1.3 cm Offset

(c) 3.8 cm Offset

(d) 6.4 cm Offset

Figure 6.7: Comparison of data (points) with model calculations (dashed line) for each of the experiments performed with the 6 Torr cell. The solid line represents the expected attenuation for a gas with an effective diffusion coefficient of 0.020 m^2/s.

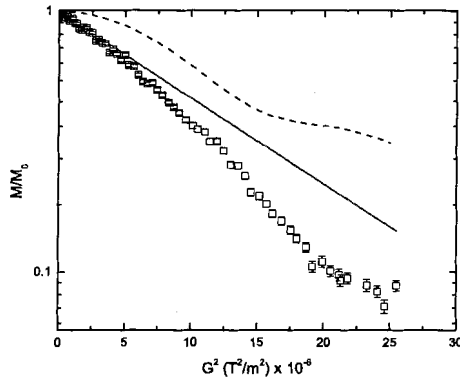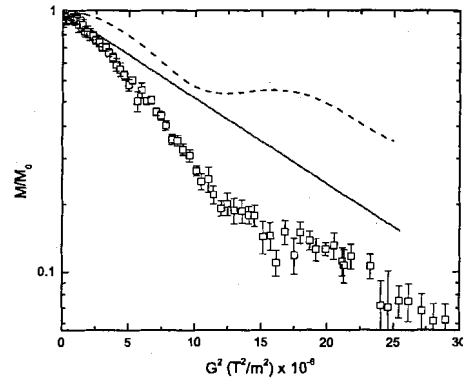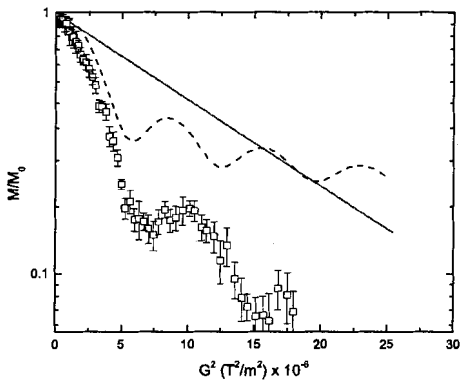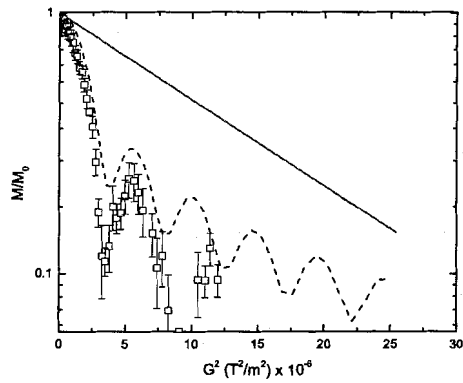The experiments performed with the 6-Torr OP cell provide much more convincing evidence that the extra attenuation observed in these experiments is due to concomitant gradients. Figure 6.7(a) compares the data from the experiment with the 6-Torr cell placed 0.6 cm from the isocentre of the magnet with model calculations for concomitant gradients. This dataset is striking because, even though it is slightly closer to the isocentre than the 1-Torr OP cell was (cf. Fig. 6.1) the attenuation curve clearly deviates from the expected attenuation for diffusion in a gradient. Note, however, that the deviation occurs at gradient amplitudes larger than those probed in the 1-Torr cell experiment. In effect the additional attenuation is revealed through the use of higher density gas in order to slow down diffusion. This in turn allows larger gradients to be applied. Again, the conclusion from this dataset is that there are additional mechanisms that attenuate the FID. However, it is not possible to conclude that these effects are caused by concomitant gradients.

Figures 6.7(b), 6.7(c), and 6.7(d) compare data from the 6-Torr OP cell placed 1.3 cm, 3.8 cm and 6.4 cm from the isocentre of the magnet, respectively. As the cell is displaced further from the isocentre of the magnet, nodes appear in the data. The same features are clearly evident in the model calculations. Although the attenuation levels do not agree, the similarity between the data and calculations is very suggestive.

Concomitant gradients cause incomplete rephasing during a bipolar gradient pulse as each spin is subjected to a different net magnetic field. The nodes that are predicted by the model calculations and that are present in the experimental data represent destructive interference in the time rate-of-change of magnetic flux arising from atoms located in different parts of the cell. However, it is possible for constructive interference to occur resulting in local maxima. The periodicity of the nodes scales with two factors: the length of the cell and its position with respect to the isocentre. As the length of the cell increases, so does the spread of Larmor frequencies. A smaller gradient is thus required to produce each node. The period of the nodes will also decrease as the sample moves away from the isocentre. This is because the magnitude of changes in the magnetic field during the gradient pulse increases away from the isocentre.

6.4 Asymmetric GRSE Experiment

Further evidence for the hypothesis that concomitant gradients are responsible for the features discussed in the previous section is revealed in a series of experiments in which GRSE sequences were applied with an asymmetric bipolar gradient pulse. The term asymmetric signifies that the two lobes of the gradient pulse are applied for unequal times. Figure 6.8 shows the data from two studies in which the plateau time of the positive gradient was either 450 μs or 2500 μs while the plateau time of the negative gradient was varied. Data are shown for three different cell positions with respect to the isocentre of the magnet. Ordinarily one would expect the minimum attenuation (the peak in the two curves) to occur when the two plateaus of the gradient pulse are identical. That is the ratio of the application times is 1. The reason for this is that the phase accumulation that occurs during one gradient pulse is expected to be completely unwound through application of a gradient of the opposite strength applied for the same length of time. More generally, this is expected to be true as long as the area of the two gradient pulses is equal. This is clearly not the situation with the data. The resulting peak is the result of two processes. The longer the second half of the bipolar pulse lasts, the more the magnetization is unwound leading to a larger FID amplitude. Opposing this, the longer the gradients are applied, the longer irreversible processes (i.e. diffusion) have to destroy the nuclear coherence leading to smaller and smaller FID amplitudes. Since these processes influence the FID amplitude in opposite senses, the peak must occur between the value of 0 and 1. The peak in the 2500 μs data occurs at a smaller lobe area ratio than that for the 450 μs data because diffusion has much more time to destroy the nuclear coherence.

Another interesting result from the experiment involving the shorter gradient pulse is that there is a systematic difference between the data acquired in the centre position and those acquired in the two offset positions. More of the magnetization is recovered in the centre position. This appears to be another demonstration of the influence of concomitant gradients. As previously explained, concomitant gradients increase in magnitude as the distance from the isocentre is increased. It thus becomes impossible to unwind a larger fraction of the magnetization as the cell is shifted further along the axis.

A third result from these experiments is that, in both studies, the FID attenuation that occurs at the 10 cm offset and at the -10 cm offset is the same. Along with the results

(a) 450 μs Positive Gradient   (b) 2500 μs Positive Gradient
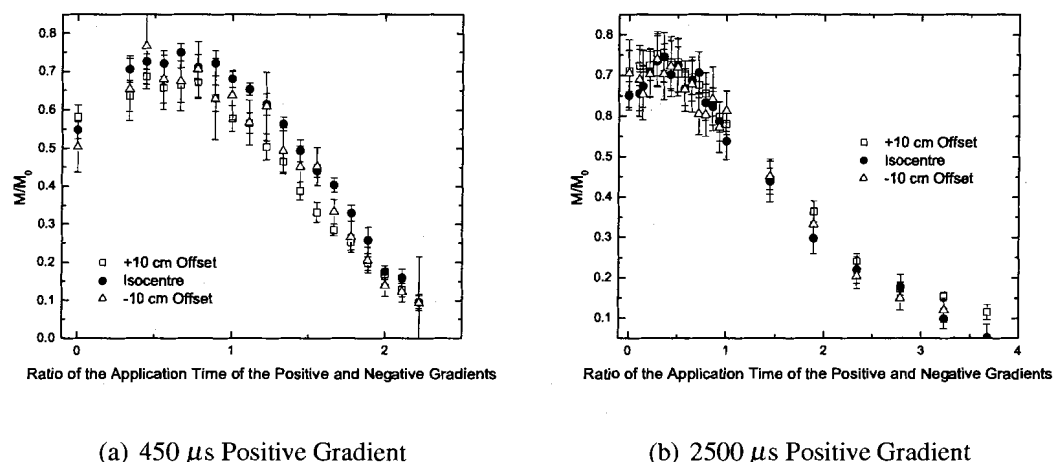
Figure 6.8: FID attenuation from a series of GRSE experiments using asymmetric gradients. The experimental results displayed in Fig. 6.8(a) used a positive gradient with a value of τ equal to 450 μs. The strength of the applied gradient was G = 1.01×10^{-3} T/m. The experimental results displayed in Fig. 6.8(b) used a positive gradient with a value of τ equal to 2650 μs. The strength of the applied gradient was G = 0.15×10^{-3} T/m.

shown in Fig. 6.3, this data provides evidence that the mechanism causing attenuation must be symmetric along the z-axis. This is an expected feature since the concomitant gradients of Golay coils are symmetric along the z-axis (i.e. B depends on z^2).

The experiments described above were repeated after switching the order of the positive and negative gradient pulse. The recorded data were the same as that reported above. This is expected and further strengthens the argument that only diffusion and concomitant gradients are affecting the attenuation of the FID amplitude.

6.5 Discussion

The comparisons between data and model calculations presented in this chapter are strongly suggestive of the key role played by concomitant gradients during GRSE experiments in low magnetic fields. Nevertheless, it is important to consider alternate mechanisms that might play a role.

One such mechanism is the breakdown of Eq. 2.55. This breakdown is thought to occur

when the application time of the bipolar gradient pulse is such that spins diffuse distances that are comparable to the size of restriction. Equation 2.55 can be expanded to find [66]

$$\ln\left(\frac{M(t)}{M(0)}\right) = -\frac{2G^2\tau^3 D_0}{3}\left[1 - \frac{\alpha S\sqrt{D_0\tau}}{V} + \vartheta\left(D_0\tau\right)\right] + \vartheta\left(D_0^{5/2}G^4\tau^{13/2}S/V\right), \tag{6.12}$$

where $\alpha = 32(2\sqrt{2}-1)/105\sqrt{\pi}$, and S/V is the surface area to volume ratio of the pore. This formula can be rewritten in terms the three length scales introduced in Chapter 3:

$$\ln\left(\frac{M(t)}{M(0)}\right) = -\frac{2}{3}\left(\frac{\ell_D}{\ell_G}\right)^6\left[1 - 3\alpha d\frac{\ell_D}{\ell_s} + \vartheta\left(\left(\frac{d\ell_D}{\ell_s}\right)^2\right)\right] + \vartheta\left(\frac{d\ell_D^{13}}{\ell_G^{12}\ell_s}\right), \tag{6.13}$$

where d is the dimensionality of the restriction. There are two distinct regimes for the breakdown of Eq. 6.13: either $(\ell_D/\ell_s)^2$ or $(\ell_D/\ell_G)^{12}(\ell_D/\ell_s)$ becomes significant. In the case of the 6 Torr cell, when gradient applications are of order 5×10^{-3} T/m the second term becomes large. In other words, a plot of $M(t)/M(0)$ versus G^2 should have both a linear and a quadratic term. The ratio of the two components should be of order 10^5 m^2/T^2. Figure 6.9 displays the result of applying a second-order polynomial fit to the attenuation measurements acquired when the 6 Torr cell was 6 mm from the gradient isocentre. The ratio of the two components from this fit is $2.1(5) \times 10^4$ m^2/T^2. This result suggests that the non-linear behavior of the attenuation from this particular experiment could be explained by the breakdown of the short-time approximation.

Another type of mechanism that needs to be discussed is the appearance of spin echo diffraction peaks that have been observed in recent years by a number of groups [42, 43, 67–69]. Callaghan et al. [69] showed that the spin echo amplitude for a PGSE showed evidence of diffraction peaks associated with the dimensions of the confining pore. However, they predict that these peaks will only occur when the GRSE interpulse delay time η is of order ℓ_G^2/D_0. For the experimental work in this thesis, the largest values of ℓ_G^2/D_0 are of order 0.2 s at 1 Torr and 1 s at 6 Torr. The value of η that was used for the GRSE experiments in this thesis was 10 μs and, thus, it seems unlikely that diffraction effects play a role.
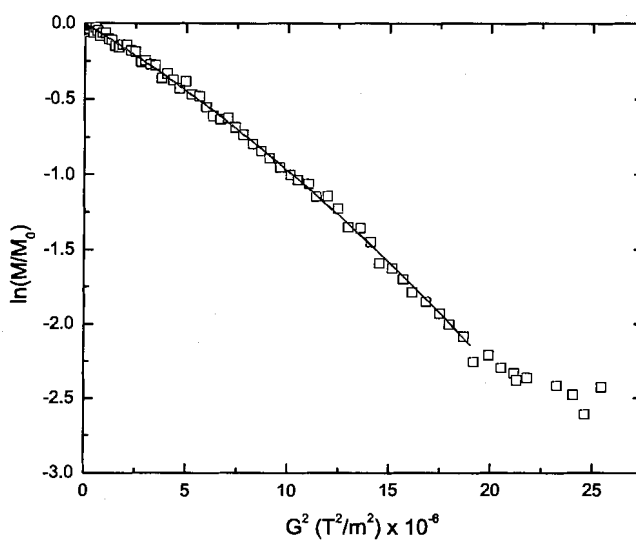
Figure 6.9: FID attenuation for the 6 Torr cell placed at 0.6 cm from the isocentre of the magnet along the z-axis as measured using a GRSE sequence. The data have been fit to a second-order polynomial. The curvature is consistent with a breakdown of the short time approximation.

Chapter 7

Conclusion

The goal of this thesis has been to probe the influence of concomitant gradients on NMR measurements of diffusion coefficients using a GRSE sequence. These gradients warp idealized planes of constant Larmor precession frequency into cylinders with a characteristic radius of $R_c = B_0/G$. The net result is a non-trivial distortion in the mapping between gradient amplitude and position which, in imaging applications, translates into artifacts (distortion and blurring). Experiments were performed in a regime where the maximum value of R_c was of order 10 cm, which is comparable to the dimensions of the sample. This in turn was expected to result in a situation where the influence of concomitant gradients would become important.

The experiments reported in this thesis made use of a GRSE sequence which involves a pulsed, bipolar field gradient. During this gradient pulse, the amplitude of the FID signal from a sample of hyperpolarized ^{3}He gas confined to a cylindrical cell is attenuated. This attenuation is caused by the diffusive movement of atoms in the field gradient which leads to an irreversible loss of nuclear magnetization. Measurements of this attenuation allow one to determine the diffusion coefficient of the gas, as long as the perturbing influence of concomitant gradients can be ignored. At large values of G/B_0 (i.e. small R_c) concomitant gradients result in additional signal attenuation that is related to an imperfect refocusing of the nuclear coherence. The observation and study of this previously unidentified effect amounts to the principal scientific result reported in this thesis.

One of the challenges associated with this project was to determine the FID amplitude after the gradient pulse. Another complicating factor was the presence of frequency drift

noise in the experimental data. As the gradient strength was increased, the amplitude of the FID and hence the SNR decreased. A numerical study was thus performed to compare the accuracy of fitting several different analytic models to simulated noisy FID data. This study showed that a bias caused by Rician noise was introduced for amplitude SNR < 10 unless a full complex damped sinusoid was used to fit the data. This bias reduces the apparent attenuation of a FID, an effect that would tend to mask the influence of concomitant gradients. However, even the full damped sinusoid model broke down when fractional frequency fluctuations σ > 50 ppm were introduced. The actual experimental data was characterized by amplitude SNR that ranged from 50 to 1 and σ that ranged from 0.075 to 10 ppm. In practice, the complex damped sinusoid model had to be fit to the data in "windows" because of systematic frequency drifts of order 0.3 Hz.

GRSE experiments were performed at various gradient strengths, OP cell positions, and gas pressures. The results of experiments using the two pressures were different and probed two different diffusion regimes. Measurements from an OP cell filled with 1 Torr of ^{3}He at the isocentre of the magnet agreed with the expected attenuation from diffusion. When the 1 Torr OP cell was displaced along the z-axis of the magnet, the measured attenuation displayed a systematic difference from the attenuation expected for diffusion. This difference depended on gradient strength and cell location. Experiments on both sides of the isocentre showed that the systematic difference was symmetric about the isocentre. Experiments with a 6 Torr OP cell showed that at all displacements from the gradient isocentre, the measured FID amplitude attenuation showed a systematic difference from the contribution expected for diffusion. The data from the 6 Torr cell displayed evidence of attenuation nodes that were predicted by a model that was used to calculated the expected attenuation from concomitant gradient effects.

Typically, the measured attenuation did not agree with the expected attenuation from diffusion or the calculated attenuation from the influence of concomitant gradients. Therefore, it is possible that there are other mechanisms causing attenuation in these experiments. Nonetheless, the fact remains that the influence of concomitant gradients is destructive to the coherence of nuclear precession signals under certain conditions. Based on the results of this thesis, it is possible to present several different suggestions for minimizing the effect of concomitant gradients when using GRSE pulse sequences. One obvious suggestion is to perform experiments only in regimes where $B_0 \gg \boldsymbol{G} \cdot \boldsymbol{r}$. This can be done either by raising

B_0 or by lowering the magnitude of the applied gradients. However, by lowering gradient strength, the application time of the gradient pulse must be increased. This is disadvantageous for rapid imaging sequences. A second suggestion is to place the imaging target at or near the isocentre of the magnet where concomitant gradients are small. This option is not particularly useful for large fields of view. A final recommendation is to consider using PGSE sequences instead of a GRSE sequence. The PGSE sequence is not as susceptible to concomitant gradient effects. This approach is not an option at high fields where the absorption of RF power from tipping pulses is significant. However, it may be feasible at low field where specific absorption rates are low.

There are several avenues for future research. It would be extremely useful to develop a model that takes into account the attenuating effects of both diffusion and concomitant gradients. This would enable one to compare the calculated attenuation with the experimental data presented in this thesis to determine if there are other attenuating mechanisms. Additional experiments could also be done to investigate the effect of increasing B_0. This would determine at what value of R_c concomitant gradients become non-negligible.

Recent studies of hyperpolarized noble gases have demonstrated the importance of accurate measurements of gas diffusion coefficients (in particular the diffusion coefficients for gas mixtures involving ^{3}He. The measurement performed by Hayden et. al [5] is regarded as a reliable measure of diffusion coefficients. This thesis has characterized one systematic bias (i.e. concomitant gradients) that may affect measurements of this kind. This work is important for studies of MR in very- and ultra-low fields, diffusion of polarized gases and potentially work involving MR probes of diffusion in inhomogeneous fields.

Appendix A

Program for Creating Simulated FIDs

The following code, written in Igor Pro 5.00, was used to create simulated FIDs and then fit to the FIDs with a complex sinusoid model. The parameters of the minimized model were then recorded.

```
// The following program creates simulated complex decaying sinusoids that
// contain amplitude and frequency noise.

#pragma rtGlobals=1

// The first three functions and macro are used to force IGOR to fit to two
// sinusoids at the same time.

Function/C csin(m,n)
// Returns a complex sinusoid.
Variable m,n
Return cmplx(cos(m+n), sin(m+n))
end

Function/C myCFunc(w,x)
// Returns a complex decaying sinusoid.
Wave w; Variable x
return w[0]*csin(w[1]*x,w[2])*exp(-x/w[3])
End

Function myFunc(w,p)
Wave w
Variable p
Wave/C wy= $"FullData"
Variable x=pnt2x(wy,p)
Variable/C ydata=wy[p]
Variable/C calc=myCFunc(w,x)
```

```
Variable sr,si
Variable dr,di
dr=real(ydata)-real(calc)
di=imag(ydata)-imag(calc)
sr=sign(dr)
si=sign(di)
dr *= dr
di *= di
if( dr>di)
return sr*sqrt(dr+di)
else
return si*sqrt(dr+di)
endif
end


Macro SetupForMethod(ywave)
String ywave
Prompt ywave,"complex data wave",popup WaveList("*",";","")
Duplicate/O $ywave,dummyData
Redimension/R dummyData
SetScale/P x,0,1,dummyData
dummyData=0
Duplicate/O dummyData, dummyFIt
End


Function f()

//  Suppresses the curve fit window: speeds things up.
variable V_FitOptions=4

variable i=0, imax=5000  //  The number of points in the simulated sinusoid.
Make/o coef={100,0.1,0,5000}  //  Initial guess for the complex fit.
Make/O/C /N=(imax) myCDataFit
myCDataFit=0
myCDataFit=myCFunc(coef,x)
variable amp=100, tau=5000, omega=1/10  //  Seed values for the simulated sinusoid.
Make /N=(imax) /O /D SignalReal SignalImag OmegaV PhaseV

Make /O /N=1 Interval jmax
variable j=7
Interval={2500,1000,500,250,100,50,25}  //  Different window sizes to test
jmax=2*(imax/Interval)-1

variable m=1, mmax=1000  //  Number of times to test each setting
Make /O /N=(mmax) MeanFreq MeanAmp MeanDecay

variable k=1, kmax=3 // Number of amplitude noise values to be tested
Make /O /N=(kmax) Noise
```

```
Noise={0.01, 0.1, 1} // Amplitude noise settings to use.

variable n=0, nmax=9 // Number of frequency noise values to be tested.
Make /O /N=(nmax) SignalNoise
SignalNoise={0,0.5,1,2,5,10,20,50,100} // Frequency noise values to test.

variable p=0, pmax=7
Make /O /N=(nmax, pmax, kmax) TotalFreq TotalSDFreq TotalAmp
Make /O /N=(nmax, pmax, kmax) TotalSDAmp TotalDecay TotalSDDecay
TotalFreq=0
TotalSDFreq=0
TotalAmp=0
TotalSDAmp=0
TotalDecay=0
TotalSDDecay=0

for(n=0;n<nmax;n+=1)
for(p=0;p<pmax;p+=1)
for(k=0;k<kmax;k+=1)
for(m=0;m<mmax;m+=1)

// The following code simulates the real and imaginary component of
// the complex sinusoid, creates complex dataset, and fits a complex
// sinusoid to the simulation.

OmegaV=0
PhaseV=0
SignalReal=0
SignalImag=0

for (i=0;i<imax;i+=1)
// For each point of the simulation there is a random frequency.
OmegaV[i]=omega*(1+gnoise(Noise[k]))
endfor

for(i=1;i<imax;i+=1)
// Based on the random frequency the phase is calculated.
PhaseV[i]=PhaseV[i-1]+((OmegaV[i-1]-OmegaV[i])*(i-1))
endfor

// The 0 value of the real and imaginary components.
SignalReal[0]=amp*cos(OmegaV[0]*0)+gnoise(SignalNoise[n])
SignalImag[0]=amp*sin(OmegaV[0]*0)+gnoise(SignalNoise[n])

for(i=1;i<imax;i+=1)
// The components are filled.
SignalReal[i]=amp*cos(OmegaV[i]*i+PhaseV[i])*exp(-i/tau)+gnoise(SignalNoise[n])
SignalImag[i]=amp*sin(OmegaV[i]*i+PhaseV[i])*exp(-i/tau)+gnoise(SignalNoise[n])
```

```
endfor

//  The next four lines create a complex dataset containing the two components.
Duplicate /O/C SignalReal FullData
Redimension/C FullData
FullData=0
FullData=cmplx(SignalReal, SignalImag)

// The following three arrays will contain the estimated parameters of the fit.
// Depending on the window size being used the arrays will have a different
// dimension.  They must be recreated before each window size is tested.

Make /N=(jmax[p]) /O /D Freq Amplitude Decay
Freq=0
Amplitude=0
Decay=0

for(j=0;j<jmax[p];j+=1)

coef={100,0.1,0,5000}

FuncFit /N/Q myFunc,coef,dummyData(j/2*(Interval[p]),j/2*
/(Interval[p])+(Interval[p]))/D=dummyFIt

//  The estimated parameters are stored after each fit.

Freq[j]=Coef[1]
Amplitude[j]=Coef[0]
Decay[j]=Coef[3]

//  If the decay values are too large or too the small, the fit failed.
// To not include them in mean calculations they are set to NaN.

if(Decay[j]>100000)
Amplitude[j]=NaN
Decay[j]=NaN
Freq[j]=NaN
elseif(Decay[j]<0)
Amplitude[j]=NaN
Decay[j]=NaN
Freq[j]=NaN
endif

endfor

//  This calculates the mean and standard deviation of the three parameters
// from all of the intervals tested.
```

```
WaveStats /Q Freq
MeanFreq[m]=V_avg
WaveStats /Q Amplitude
MeanAmp[m]=V_avg
WaveStats /Q Decay
MeanDecay[m]=V_avg

endfor

//  The final statistics for every run is contained in the following arrays.

WaveStats /Q MeanFreq
TotalFreq[n][p][k]=V_avg
TotalSDFreq[n][p][k]=V_sdev
WaveStats /Q MeanAmp
TotalAmp[n][p][k]=V_avg
TotalSDAmp[n][p][k]=V_sdev
WaveStats /Q MeanDecay
TotalDecay[n][p][k]=V_avg
TotalSDDecay[n][p][k]=V_sdev

endfor
endfor
endfor
End
```

Appendix B

Program for Calculating FID Attenuation

The following code, written in Mathematica, was used to calculate the expected FID attenuation due to the influence of concomitant gradients during a bipolar gradient pulse.

The following lines of code set up values for constants.

```
SetDirectory["Math"]
Directory[]
```

The following lines define the gyromagnetic ratio (gamma), the magnetic field (Bo), the radius (a), the plateau length (tau), and the ramp time (taur).

```
gamma=N[2*Pi*32.432*10^6];
Bo=N[6*10^(-4)];
a=N[.52/2];
tau=N[300*10^(-6)];
taur=N[150*10^(-6)];
philab=N[gamma*Bo*(2*tau*4*taur)];
l=0.093;
```

The following line calculates the phase accumulated during the gradient plateaus.

```
phic[y_,z_,G_]:=gamma*tau*(Sqrt[(Bo+Gy)^2+(Gz)^2]+Sqrt[(Bo-Gy)^2+(Gz)^2]);
```

The following line calculates the phase accumulated during the gradient ramps.

```
phir[y_,z_,G_]:=NIntegrate[gamma*(Sqrt[(Bo+G*(1-t/taur)y)^2+(G*(1-t/taur)z)^2]+
Sqrt[(Bo-G*(1-t/taur)y)^2+(G*(1-t/taur)z)^2], {t,0,2 taur}]
```

The following two lines calculate the magnetization after a gradient pulse.

```
Mr[zc_,G_]:=Delat^2*Abs[Sum[Sqrt[a^2-y^2]*Exp[I*phic[y,z,G]+phir[y,z,G]-philab)],
{y,-a+Delta,a,Delta},{z,zc-l/2+Delta,zc+l/2,Delta}]];
M[zc_,G_]:=Delat^2*Abs[Sum[Sqrt[a^2-y^2]*Exp[I*phic[y,z,G]-philab)],
{y,-a+Delta,a,Delta},{z,zc-l/2+Delta,zc+l/2,Delta}]];

t1=AbsoluteTime[];
Delta=.00025;
Mr[0.09,0.000]
M[0.9,0.000]
t2=AbsoluteTime[];
t2-t1

norm=Mr[0,0]
t1=AbsoluteTime[]
```

The following four blocks of code calculate the magnetization for various gradient strengths at four different positions of a cylindrical cell.

```
D1=Table[{x,Mr[0.0065,x]/norm},{x,0,0.005,0.0001}];
G1=ListPlot[D1,PlotStyle->RBGColor[0,0,0]]
output=OpenWrite["6mm.dat"];
tabdat=TableForm[D1,TableSpacing->{0,5}];
WriteString[output,tabdat];
Close["6mm.dat"];

D2=Table[{x,Mr[0.0135,x]/norm},{x,0,0.005,0.0001}];
G2=ListPlot[D2,PlotStyle->RBGColor[0,0,0]]
output=OpenWrite["13mm.dat"];
tabdat=TableForm[D2,TableSpacing->{0,5}];
WriteString[output,tabdat];
Close["13mm.dat"];

D3=Table[{x,Mr[0.0385,x]/norm},{x,0,0.005,0.0001}];
G3=ListPlot[D3,PlotStyle->RBGColor[0,0,0]]
output=OpenWrite["38mm.dat"];
tabdat=TableForm[D3,TableSpacing->{0,5}];
WriteString[output,tabdat];
Close["38mm.dat"];

D4=Table[{x,Mr[0.0635,x]/norm},{x,0,0.005,0.0001}];
G4=ListPlot[D4,PlotStyle->RBGColor[0,0,0]]
output=OpenWrite["63mm.dat"];
tabdat=TableForm[D4,TableSpacing->{0,5}];
WriteString[output,tabdat];
```

```
Close["63mm.dat"];
```

Bibliography

[1] P.C. Lauterbur. Image formation by induced local interactions: examples employing nuclear magnetic resonance. *Nature*, 242:190–191, 1973.

[2] PT Callaghan. *Principles of Nuclear Magnetic Resonance Microscopy*. Oxford University Press Inc., 1991.

[3] DA Yablonskiy, AL Sukstanskii, and JJH Ackerman. Image artifacts in very low magnetic field MRI: The role of concomitant gradients. *J. Magn. Reson.*, 174:279–286, 2005.

[4] CP Bidinosti, J Choukeife, PJ Nacher, and G Tastevin. In vivo NMR of hyperpolarized ^{3}He in the human lung at very low magnetic fields. *J. Magn. Reson.*, 162:122–132, 2003.

[5] ME Hayden, G Archibald, KM Gilbert, and C Lei. Restricted diffusion within a single pore. *J. Magn. Reson.*, 169:313–322, 2004.

[6] CP Bidinosti, J Choukeife, G Tastevin, PJ Nacher, and A Vignaud. MRI of the lung using hyperpolarized ^{3}He at very low magnetic field (3 mT). *MAGMA*, 16(6):255–258, 2004.

[7] AK Venkatesh, AX Zhang, J Mansour, L Kubatina, CH Oh, G Blasche, MS Ünlü, D Balamore, FA Jolesz, BB Goldber, and MS Albert. MRI of the lung gas-space at very low-field using hyperpolarized noble gases. *Magn. Reson. Imag.*, 21:773–776, 2003.

[8] RW Mair, MI Hrovat, S Patz, MS Rosen, IC Ruset, GP Topulos, LL Tsai, JP Butler, FW Hersman, and RL Walsworth. ^{3}He lung imaging in an open access, very-low-field human magnetic resonance imaging system. *Magn. Reson. Med.*, 53:745–749, 2005.

[9] SK Lee, M Mößle, W Myers, N Kelso, AH Trabesinger, A Pines, and J Clarke. SQUID-detected MRI at 132 μT with T_1-weighted contrast established at 10 μT - 300 mT. *Magn. Reson. Med.*, 53:9–14, 2005.

[10] AN Matlachov, PL Volegov, MA Espy, JS George, and RH Kraus Jr. SQUID detected NMR in microtesla magnetic fields. *J. Magn. Reson.*, 170:1–7, 2004.

[11] A Mohoric, J Stepisnik, M Kos, and G Planinsic. Self-diffusion imaging by spin echo in Earth's magnetic field. *J Magn. Reson.*, 136:22–26, 1999.

[12] PT Callaghan, CD Eccles, and JD Seymour. An Earth's field nuclear magnetic resonance apparatus suitable for pulsed gradient spin echo measurements of self-diffusion under Antartic conditions. *Rev. Sci. Instrum.*, 68:4263–4270, 1997.

[13] J Stepisnik, V Erzen, and M Kos. NMR imaging in the Earth's magnetic field. *Mag. Reson. Med.*, 15:386–391, 1990.

[14] E Chapple. Fundamental SNR and SAR limitation in low-field NMR (in preparation). Master's thesis, Simon Fraser University, 2006.

[15] WR Myers, M Mößle, and J Clarke. Correction of concomitant gradient artifacts in experimental microtesla MRI. *J. Magn. Reson.*, 177:274–284, 2005.

[16] PL Volegov, JC Mosher, MA Espy, and RH Kraus Jr. On concomitant gradients in low-field MRI. *J. Magn. Reson.*, 175:103–113, 2005.

[17] DG Norris and JMS Hutchison. Concomitant magnetic field gradients and their effects on imaging at low magnetic field strengths. *Magn. Reson. Imag.*, 8:33–37, 1990.

[18] J Parra-Robles, AR Cross, and GE Santyr. Theoretical signal-to-noise ratio and spatial resolution dependence on the magnetic field strength for hyperpolarized noble gas magnetic resonance imaging of human lungs. *Med. Phys.*, 32:221–229, 2005.

[19] FD Colegrove, LD Schearer, and GK Walters. Polarization of ^{3}He gas by optical pumping. *Phys. Rev.*, 132:2561–2572, 1963.

[20] MA Bouchiat, TR Carver, and C.M. Varnum. Nuclear polarization in He^3 gas induced by optical pumping and dipolar exchange. *Phys. Rev. Lett.*, 5:373–375, 1960.

[21] GP Wong, CH Tseng, VR Pomeroy, RW Mair, DP Hinton, D Hoffmann, RE Stoner, FW Hersman, DG Cory, and RL Walsworth. A system for low field imaging of laser-polarized noble gas. *J. Magn. Reson.*, 141:217–227, 1999.

[22] JC Leawoods, DA Yablonskiy, B Saam, DS Gierada, and MS Conradi. Hyperpolarized ^{3}He gas production and MR imaging of the lung. *Concepts Magn. Reson.*, 13:277–293, 2001.

[23] HE Moller, XJ Chen, B Saam, KD Hagspiel, GA Johnson, TA Altes, EE de Lange, and HU Kauczor. MRI of the lungs using hyperpolarized noble gases. *Magn. Reson. Med.*, 47:1029–1051, 2002.

[24] JR Owers-Bradley, S Fichele, A Bennattayalah, CJS McGloin, RW Bowtell, PS Morgan, and AR Moody. MR tagging of human lungs using hyperpolarized he-3 gas. *J. Magn. Reson. Imag.*, 17:142–146, 2003.

[25] EL Hahn. Spin echoes. *Phys. Rev.*, 80:580, 1950.

[26] M Salerno, EE de Lange, TA Altes, JD Truwit, JR Brookeman, and JP Mugler III. Emphysema: Hyperpolarized helium 3 diffusion MR Imaging of the lungs compared with spirometric indexes - Initial experience. *Radiology*, 222:252–260, 2002.

[27] BT Saam, DA Yablonskiy, VD Kodibagkar, JC Leawoods, DS Gierada, JD Cooper, SS Lefrak, and MS Conradi. MR Imaging of diffusion of ^{3}He gas in healthy and diseased lungs. *Magn. Reson. Med.*, 44:174–179, 2000.

[28] JR Mayo and ME Hayden. Hyperpolarized Helium 3 diffusion imaging of the lung. *Radiology*, 222:8–11, 2002.

[29] S Fichele, MNJ Paley, N Woodhouse, PD Griffiths, EJR van Beek, and JM Wild. Investigating ^{3}H diffusion NMR in the lungs using finite difference simulations and in vivo PGSE experiments. *J Magn. Reson.*, 167:1–11, 2004.

[30] MD Hürlimann, KG Helmer, LL Latour, and CH Sotak. Restricted diffusion in sedimentary rocks. Determination of surface-area-to-volume ratio and surface relaxivity. *J. Magn. Resons. A*, 111:169–178, 1994.

[31] RW Mair, GP Wong, D Hoffmann, MD Hürlimann, S Patz, LM Schwartz, and RL Walsworth. Probing porous media with gas diffusion NMR. *Phys. Rev. Lett.*, 83:3324–3327, 1999.

[32] E Durand, G Guillot, L Darrasse, G Tastevin, PJ Nacher, A Vignaud, D Vattolo, and J Bittoun. CPMG measurements and ultrafast imaging in human lungs with hyperpolarized helium-3 at low field (0.1 T). *Magn. Reson. Med.*, 47:75–81, 2002.

[33] S Ley, J Zaporozhan, A Morbach, B Eberle, KK Gast, CP Heussel, A Biedermann, E Mayer, J Schmiedeskamp, and A Stepniak. Functional evaluation of emphysema using diffurion-weighted ^{3}Helium-magnetic resonance imaging, high-resolution computed tomography, and lung function tests. *Invest. Radiol.*, 39:427–434, 2004.

[34] PN Sen, A André, and S Axelrod. Spin echoes of nuclear magnetization diffusing in a constant magnetic field gradient and in a restricted geometry. *J. Chem. Phys.*, 111: 6548–6555, 1999.

[35] PT Callaghan. A simple matrix formalism for spin echo analysis of restricted diffusion under generalized gradient waveforms. *J Magn. Reson.*, 129:74–84, 1997.

[36] WS Price, P Stilbs, and O Söderman. Determination of pore space shape and size in porous systems using NMR diffusometry. Beyond the short gradient pulse approximation. *J Magn. Reson.*, 160:139–143, 2003.

[37] LJ Zielinski and PN Sen. Effects of finite-width pulses in the pulsed-field gradient measurement of the diffusion coefficient in connected porous media. *J Magn. Reson.*, 165:153–161, 2003.

[38] EO Stejskal and JE Tanner. Spin diffusion measurements: Spin echoes in the presence of a time-dependent field gradient. *J. Chem. Phys.*, 42(1):288–292, 1965.

[39] RC Wayne and RM Cotts. Nuclear-magnetic-resonance study of self-diffusion in a bounded medium. *Phys. Rev.*, 151:264–272, 1966.

[40] RC Wayne and RM Cotts. Nuclear-magnetic-resonance study of self-diffusion in a bounded medium. *Phys. Rev.*, 159:486, 1967.

[41] KG Helmer, MD Hürlimann, TM de Swiet, P Sen, and CH Sotak. Determination of ratio of surface area to pore volume from restricted diffusion in a constant field gradient. *J. Magn. Reson. A*, 115:257–259, 1995.

[42] A Coy and PT Callaghan. Pulsed gradient spin echo nuclear magnetic resonance for molecules diffusing between partially reflecting rectangular barriers. *J. Chem. Phys.*, 101:4599–4609, 1994.

[43] SJ Gibbs. Observations of diffusive diffraction in a cylindrical pore by PFG NMR. *J. Magn. Reson.*, 124:223–226, 1996.

[44] S Gasiorowicz. *Quantum Physics*. John Wiley & Sons, Inc., second edition, 1996.

[45] E Courtade, F Marion, PJ Nacher, G Tastevin, K Kiersnowski, and T Dohnalik. Magnetic field effects on the 1083 nm atomic line of helium. *Eur. Phys. J. D*, 21:25–55, 2002.

[46] M Batz, S Baeßler, W Heil, EW Otten, D Rudersdorf, J Schmiedeskamp, Y Sobolev, and M Wolf. ^{3}He spin filter for neutrons. *J. Res. Natl. Inst. Stand. Technol.*, 110: 293–298, 2005.

[47] WA Fitzsimmons, NF Lane, and GK Walters. Diffusion of He (2^3S_1) in Helium gas; 2^3S_1-1^1S_0 interaction potentials at long range. *Phys. Rev.*, 174:193–200, 1968.

[48] EM Purcell and GB Field. Influence of collisions upon population of hyperfine states in hydrogen. *J. Astrophys*, 124:542, 1956.

[49] A Abragam. *The Principles of Nuclear Magnetism*. Oxford University Press Inc., 1961.

[50] PJ Mohr and BN Taylor. *CODATA recommended values of the fundamental physical constants: 2002*. National Institute of Standards and Technology, 2005.

[51] F Bloch, WW Hansen, and M Packard. Nuclear induction. *Phys. Rev.*, 21:127, 1946.

[52] HY Carr and EM Purcell. Effects of diffusion on free precession in nuclear magnetic resonance experiments. *Phys. Rev. 94*, 94:630–638, 1954.

[53] S Meiboom and D Gill. Modified spin-echo method for measuring nuclear relaxation times. *Rev. Sci. Instrum.*, 29:688–691, 1958.

[54] HC Torrey. Bloch equations with diffusion terms. *Phys. Rev.*, 104:563, 1956.

[55] A Haase. Snapshot FLASH MRI. Applications to T1, T2, and chemical-shift imaging. *Magn. Reson. Med.*, 13:77–89, 1990.

[56] B Robertson. Spin-echo decay of spins diffusing in a bounded region. *Phys. Rev.*, 151:273–277, 1966.

[57] CH Neuman. Spin echo of spins diffusing in a bounded medium. *J. Chem. Phys.*, 60: 4508–4511, 1974.

[58] SO Rice. Mathematical analysis of random noise. *Bell Syst. Tech. J.*, 23:282–332, 1944.

[59] SO Rice. Mathematical analysis of random noise - conclusion. *Bell Syst. Tech. J.*, 24: 46–156, 1945.

[60] A Papoulis. *Probability, Random Variables, and Stochastic Processes*. McGraw-Hill, third edition, 1991.

[61] DW Allan. Statistics of atomic frequency standards. *Proc. IEEE*, 54:221–230, 1966.

[62] C Lei. Preparation and characterisation of ^{3}He metastability-exchange optical pumping cells. Master's thesis, Simon Fraser University, 2002.

[63] F Laloe. Obituary: Jean Brossel (1918-2003). *Nature*, 422:274, 2003.

[64] JF Ganière. Relaxation nucléaire de He^3 gazeux par des surfaces. *Helv. Phys. Acta*, 46:147, 1973.

[65] TR Gentile and RD McKeown. Spin-polarizing ^{3}He nuclei with an arc-lamp-pumped neodymium-doped lanthanum magnesium hexaluminate laser. *Phys. Rev. A*, 47:456, 1993.

[66] TM de Swiet and PN Sen. Decay of nuclear magnetization by bounded diffusion in a constant field gradient. *J. Chem. Phys.*, 100:5597–5604, 1994.

[67] P Mansfield and PK Grannell. "Diffraction" and microscopy in solids and liquids by NMR. *Phys. Rev. B*, 12:3618–3634, 1975.

[68] PT Callaghan, A Coy, D MacGowan, KJ Packer, and FO Zelaya. Diffraction-like effects in NMR diffusion studies of fluids in porous solids. *Nature*, 351:467–469, 1991.

[69] SL Codd and PT Callaghan. Spin echo analysis of restricted diffusion under generalized gradient waveforms: planar, cylindrical, and spherical pores with wall relaxivity. *J. Magn. Reson.*, 137:358–372, 1999.